Universiteit Utrecht

Institute for Theoretical Physics

Master thesis

Numerical study of the trapped and extended Bose-Hubbard models

Supervisor:
Prof. dr. Cristiane Morais Smith
(ITP, Utrecht University)

Author:
Tommaso Comparin

Co-supervisors:
Marco Di Liberto MSc
(ITP, Utrecht University)

Dr. Federico Becca
(CNR-IOM and ISAS-SISSA)

August 2013

Abstract

The Bose-Hubbard model describes the physics of a system of bosonic ultracold atoms in an optical lattice, in which a phase transition is present between a superfluid phase and a Mott insulator one. The exact solution of this Hamiltonian is only feasible to find the ground-state of small systems, while other techniques (as mean-field schemes or quantum Monte Carlo) are necessary to study systems of larger size.

As a first application, we study the trapped model – relevant for the comparison with current experiments – through an inhomogeneous mean-field scheme. We describe some signatures of the phase crossover between superfluid and Mott insulator. In particular, the visibility of the quasimomentum distribution shows some kinks as a function of the lattice depth; we describe these features and we link them with the ones observed in other works in the literature.

As a second application, we use quantum Monte Carlo techniques to study the one-dimensional Bose-Hubbard model with long-range interactions and we focus on the appearance of the Haldane insulating phase, distinguishable from the Mott one through the presence of non-local hidden order. Non-local correlation functions are also used to describe the difference between the superfluid phase and the Mott insulator one.

Contents

Introduction

The research in the field of cold atoms in optical lattices has attracted much attention in the last decade, due to major experimental and theoretical advances. This is the study of particles moving in a "crystal of light" (the optical lattice), created by interfering laser beams. There is a direct correspondence with the case of electrons in the ionic lattice (as in a typical solid state system), and in fact some identical approaches are often used, as for instance the tight-binding model. However, the optical lattice set-up has some advantages with respect to solid state systems. First, light-crystal structures are very clean and host few defects; second, in a cold-atomic system the parameters of the model are usually highly tunable, whereas in solid state they are set by chemical properties of the components. The large degree of control experimentally achievable on the parameters of the lattice has opened the idea of using cold atoms in optical lattices to realize quantum simulators, i.e. experiments designed to simulate specific models from condensed matter and reproduce their physical behaviour, following ideas by Feynman [1].

A successful description for a system of bosonic atoms in an optical lattice is the Bose-Hubbard model, theoretically introduced in 1989 by Matthew Fisher and collaborators [2]. The phase diagram of this system at zero temperature includes a superfluid phase and a Mott-insulator one, separated by a quantum phase transition. In 1998 it was proposed that this model can be simulated in cold-atomic experiments [3], and in 2002 Markus Greiner and collaborators have observed the first signature of the Mott phase transition in such a set-up [4]. Together with the choice of new systems to study, recently there have also been advances in the precision of measurements, leading for instance to a resolution and control of the system at the level of a single-site [5, 6, 7].

In this thesis we have studied two realizations of the Bose-Hubbard model. In the first case we have added an external inhomogeneous potential to the original (homogeneous) model; this allows a closer comparison with experiments, in which a confining potential is required to keep the atoms inside a limited region of space. Because of the inhomogeneity, the system is not in a single global phase but it includes different domains. In particu-

lar, for an isotropic harmonic potential one can observe the formation of a structure of concentric shells of different phases. The structure and size of these shells – depending on a competition between the trapping potential and the interactions between particles – are relevant to explain some experimental results, as the coherence measurements that are obtained through *time-of-flight* imaging.

As a second case, we have studied the presence of non-local order in some phases of the Bose-Hubbard model. Inspired by research about spin systems started around 30 years ago, in 2006 it has been proposed [8] that in a one-dimensional Bose-Hubbard model a long-range repulsion can stabilize a topological phase (the Haldane insulator). The phase characterization of the system takes place by measuring some non-local correlation functions and it has been later used in the numerical or analytic studies of similar models [9, 10, 11]. Parts of this description have been recently confirmed in experiments with bosonic atoms [12], while the case of fermions is only described theoretically [13], by now.

As for other strongly-correlated systems, there is no exact analytic solution for the ground state of the Bose-Hubbard model; for this reason, this has been frequently used as a playground to introduce and test new solution techniques (exact or approximated). In this thesis we make use of two techniques. The first one is a site-decoupled mean-field technique (corresponding to the Gutzwiller ansatz). This is computationally inexpensive and allows the study of large and inhomogeneous systems, i.e. the experimentally relevant ones. However, it gives only an approximate solution, and in particular the description of the Mott insulator phase does not account correctly for fluctuations. The quantum Monte Carlo (QMC) approach includes a wide class of techniques, some of which are statistically exact (in the sense that they give unbiased estimates of physical quantities). In particular, QMC schemes for bosonic problems without frustration are generally not affected by the so called *sign problem*, that makes the study of fermionic systems more complex. Two common QMC schemes for the study of the Bose-Hubbard model are the Green's Function QMC (used in this thesis) and the Worm algorithm [14] (in the framework of the Path Integral QMC [15]). We also mention the Density Matrix Renormalization Group (DMRG) technique [16] (not used here), that provides precise results in the study of 1D systems. Recently, this approach has been reinterpreted as part of the class of Matrix Product State schemes [17], and connected to the broader class of Tensor Network techniques [18].

We also mention here some of the extensions of the Bose-Hubbard model that have been proposed and studied, both theoretically and experimentally. When the optical lattice includes a site-dependent disorder term, this can lead to a localization of the bosons and to the appearance of another phase

(the Bose glass); this was theoretically predicted in 1989 [2] and its first experimental signature was observed in 2007 [19]. In the context of time-dependent models, the use of Floquet theory [20] has introduced a way to obtain effective Hamiltonians with peculiar features, as a rescaling of the tunneling parameter or the inclusion of *correlated hopping* processes; note that the original Hamiltonians can be realized in experiments by "shaking" the lattice, i.e. through a perturbation that is periodic in time. Another example in the context of time-dependent models is reported in Ref. [21], where the resulting effective Hamiltonian includes an artificial magnetic field. This is linked to a class of systems that have been actively studied in the last years, namely the ones including an artificial gauge field for cold atoms in optical lattices [22]. A suitable design of the experimental set-up allows to simulate these models, in which the neutral atoms feel the effect of a gauge field in a way analogous to the Aharonov-Bohm effect for charged particles in electromagnetic fields. The directions of research in this subject include the characterization of quantum Hall states, the simulation of (possibly non-Abelian) lattice gauge theories, and even the study of topological field theory or Quark confinement in Quantum Chromodynamics.

General reviews about ultracold atoms in optical lattices can be found in Refs [23, 24, 25, 26], while the reviews in Refs [27] and [22] are about systems of dipolar bosonic atoms and artificial gauge fields, respectively.

The outline of this thesis is the following: we begin in chapter 1 with a general description of the Bose-Hubbard model, in which the lattice Hamiltonian is derived and its parameters are linked to the microscopic ones; we also describe the phase diagram of the homogeneous system and how it changes when an external trapping potential is included. In chapter 2, we introduce the motivation for our mean-field study of the trapped system. This comes from to the observation of certain features in the visibility of the quasi-momentum distribution (a measure of the coherence of the system); these features are observed both in experimental and numerical results. Some numerical methods that can be used to study the Bose-Hubbard model are described in chapter 3. We explain the reason why the exact diagonalization of the Hamiltonian is not feasible for large systems, and we describe a mean-field approach (valid for the homogeneous and trapped system) and some QMC techniques. In chapter 4 we present the results of our mean-field study of trapped systems in 1D and 2D; in particular, we show the density profiles for different choices of the parameters and the corresponding results for the visibility. In chapter 5 we show the results of our QMC study of the one-dimensional model with nearest-neighbour interactions and we present the characterization of some of the phases of the system, based on the measurement of non-local correlation functions. In the end we summarize the conclusions of this work and give an outlook about possible future developments.

Chapter 1

Bose-Hubbard Model

In this chapter we describe some general features of the Bose-Hubbard model and introduce some quantities that are used to characterize its phases. In section 1.1 we show how the Hamiltonian can be derived as a low temperature effective model for a gas of ultracold atoms in an optical lattice; in sections 1.2 and 1.3 we give more details about how the parameters of the model depend on the microscopic ones; in sections 1.4 and 1.5 we describe the theoretical phase diagram of the system and how it explains the shell structure of the inhomogeneous model; in section 1.6 we describe the typical measurements performed in experiments; in section 1.7 we describe an extended version of the Bose-Hubbard model, relevant to describe dipolar particles.

1.1 Lattice Hamiltonian

In this section we consider a system of cold atoms in continuous space and we show how the addition of a potential generated through interfering laser beams leads to a lattice model.

We consider the following second-quantized Hamiltonian in terms of the bosonic atomic field $\hat{\psi}(\mathbf{x})$

$$\begin{aligned} H = &\int d\mathbf{x}\ \hat{\psi}^\dagger(\mathbf{x}) \left(-\frac{\hbar^2}{2m}\nabla^2 + V_{\mathrm{OL}}(\mathbf{x}) + V_T(\mathbf{x}) - \mu \right) \hat{\psi}(\mathbf{x}) + \\ &+ \frac{1}{2}\int d\mathbf{x}\ d\mathbf{x}'\ \hat{\psi}^\dagger(\mathbf{x})\hat{\psi}^\dagger(\mathbf{x}')V(\mathbf{x}-\mathbf{x}')\hat{\psi}(\mathbf{x}')\hat{\psi}(\mathbf{x}), \end{aligned} \tag{1.1}$$

in which m is the atomic mass. This Hamiltonian includes a single-particle part (kinetic term, optical lattice potential V_{OL}, trapping potential V_T and chemical potential μ) and an interaction potential $V(\mathbf{x}-\mathbf{x}')$. We consider the s-wave scattering approximation (valid for low energy scattering) and

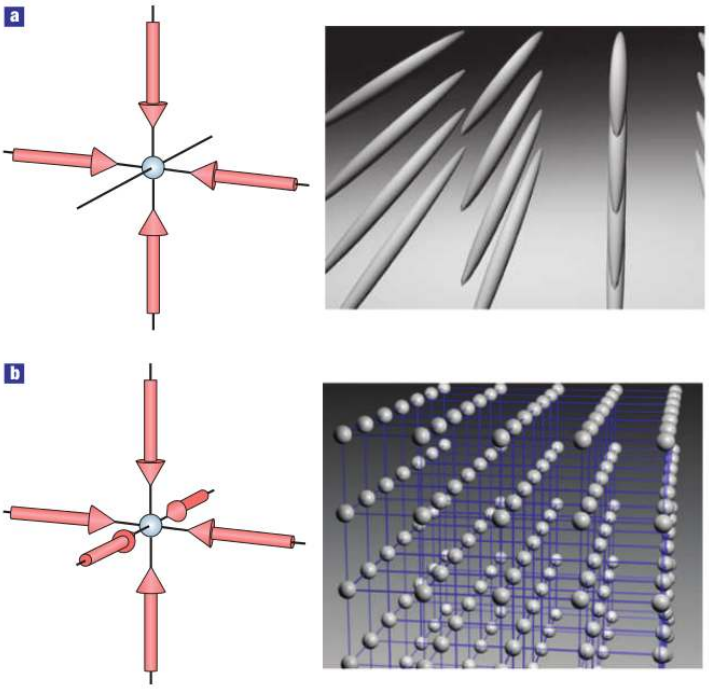

Figure 1.1: Examples of laser beams interfering to create the optical lattice potential. The resulting potential is a 2D array of 1D tubes (a), or a 3D lattice of tightly confining harmonic oscillator potentials on each site (b). Figure extracted from Ref. [23].

we replace the general interaction potential with a contact interaction

$$V(\mathbf{x}-\mathbf{x}') = \frac{4\pi a_s \hbar^2}{m}\delta(\mathbf{x}-\mathbf{x}'), \tag{1.2}$$

in which a_s is the s-wave scattering length. The trapping potential has generally the following form

$$V_T(\mathbf{r}) = \frac{m}{2}\sum_{j=1}^{3}\left(\omega_j^T x_j\right)^2, \tag{1.3}$$

in which the three trap frequencies ω_j^T are not necessarily the same.

The optical lattice potential $V_{\mathrm{OL}}(\mathbf{x})$ is produced through the interference of counter-propagating laser beams [23]. In the simple case of a cubic lattice[1], the resulting potential is

$$V_{\mathrm{OL}}(\mathbf{x}) = \sum_{j=1}^{3} V_{j,0}\sin^2(k_L x_j), \tag{1.4}$$

[1]More complicated lattice structures can be obtained by putting the laser beams at certain angles; see for instance Ref. [28].

where $k_L \equiv 2\pi/\lambda$ and λ is the wave length of the laser beams generating the lattice. Each one of the terms $V_{j,0}\sin^2(k_L x_j)$ is obtained by superimposing two polarized electromagnetic waves (see Fig. 1.1); the induced atomic dipole couples with the external electric field and this results in the confinement of the atoms around certain positions, forming a lattice with spacing $a = \lambda/2$.

Since this potential is periodic in space, the fields can be expanded in terms of Bloch's wave functions $\psi_{\mathrm{n},\mathbf{k}}(\mathbf{x})$, that have the same periodicity of the lattice and are labeled through the band index n and the quasi-momentum $\mathbf{k}$. Starting from the Bloch basis, we introduce the Wannier basis through

$$W_n(\mathbf{x}-\mathbf{x}_j) = \frac{1}{\sqrt{V}}\sum_{\mathbf{k}\in BZ}\psi_{\mathrm{n},\mathbf{k}}(\mathbf{x})e^{-i\mathbf{k}\cdot(\mathbf{x}-\mathbf{x}_j)}, \tag{1.5}$$

where $\mathbf{x}_j$ is a lattice site, BZ represents the first Brillouin zone and V is the volume. From now on, we only consider the Wannier state with lowest energy: $W(\mathbf{x}-\mathbf{x}_j) \equiv W_0(\mathbf{x}-\mathbf{x}_j)$. This assumption is justified when the gap to the first excited state W_1 is large if compared with the energy scale of interactions and of thermal fluctuations, and this is generally satisfied in practice [3]. Given the Wannier basis, the fields $\hat{\psi}$ and $\hat{\psi}^\dagger$ can be expanded as the following sums over all the lattice sites

$$\begin{aligned}\hat{\psi}^\dagger(\mathbf{x}) &= \sum_j W^*(\mathbf{x}-\mathbf{x}_j)\ \hat{b}_j^\dagger,\\ \hat{\psi}(\mathbf{x}) &= \sum_j W(\mathbf{x}-\mathbf{x}_j)\ \hat{b}_j,\end{aligned} \tag{1.6}$$

where $\hat{b}_i^\dagger$ ($\hat{b}_i$) is the operator that creates (annihilates) a particle in the state $W(\mathbf{x}-\mathbf{x}_i)$. While rewriting the Hamiltonian in terms of the operators $\hat{b}_i$ and $\hat{b}_i^\dagger$, we make use of the following assumptions:

1. the hopping processes between sites that are not nearest-neighbours are negligible w.r.t. the ones between nearest neighbours (this will be justified in section 1.3);

2. the interaction between particles on different sites is much smaller than the on-site one, and can be neglected. In section 1.7, the model with longer-ranged interactions will be described.

Given these assumptions, the original Hamiltonian (Eq. 1.1) reduces to the Bose-Hubbard Hamiltonian:

$$H = -J\sum_{\langle i,j\rangle}\hat{b}_i^\dagger\hat{b}_j + \frac{U}{2}\sum_i \hat{b}_i^\dagger\hat{b}_i^\dagger\hat{b}_i\hat{b}_i + \sum_i(\epsilon_i-\mu)\hat{b}_i^\dagger\hat{b}_i, \tag{1.7}$$

where $\langle i,j\rangle$ denotes nearest neighbouring sites and where we have defined

$$J = \int d\mathbf{x}\; W^*(\mathbf{x}-\mathbf{x}_i)\left(-\frac{\hbar^2}{2m}\nabla^2 + V_{\mathrm{OL}}(\mathbf{x})\right)W(\mathbf{x}-\mathbf{x}_j), \tag{1.8}$$

$$U = \frac{4\pi a_s \hbar^2}{m}\int d\mathbf{x}\; |W(\mathbf{x})|^4, \tag{1.9}$$

$$\epsilon_i = \int d\mathbf{x}\; V_T(\mathbf{x})|W(\mathbf{x}-\mathbf{x}_i)|^2 \approx V_T(\mathbf{x}_i). \tag{1.10}$$

Note that the expressions for the hopping coefficient J and for the on-site repulsion U are exact, but we will need some approximations (see sections 1.2 and 1.3) to evaluate them explicitly. The last step of Eq. (1.10) is based on the assumption that the characteristic length on which the trapping potential changes is much larger than the spatial extent of the Wannier function $W(\mathbf{x}-\mathbf{x}_i)$.

1.2 Wannier functions and harmonic approximation

In this section we derive an approximate expression for the Wannier functions of the lattice and we use it to estimate the value of U, the on-site repulsive interaction coefficient.

We consider the lattice potential in Eq. (1.4); this potential has the property of being *separable*, i.e. it can be written as the sum of terms depending only on one component of $\mathbf{x}$. Therefore the corresponding Wannier function $W(\mathbf{x})$ in each site can be factorized as

$$W(\mathbf{x}) = w_1(x)w_2(y)w_3(z). \tag{1.11}$$

The three one-dimensional Wannier functions w_1, w_2 and w_3 have the same expression and in the case of an isotropic lattice (with $V_{0,1} = V_{0,2} = V_{0,3}$) they are exactly the same.

By expanding the potential around the minimum of the well, we find

$$V_{\mathrm{OL}}(\mathbf{x}) = \sum_{j=1}^{3} V_{0,j}\sin^2(k_L x_j) \simeq \sum_{j=1}^{3} V_{0,j}k_L^2 x_j^2 = \frac{m}{2}\sum_{j=1}^{3}\nu_j^2 x_j^2, \tag{1.12}$$

where we have introduced the frequencies

$$\nu_j = \sqrt{\frac{2k_L^2}{m}V_{0,j}} = \frac{\hbar k_L^2}{m}\sqrt{\frac{V_{0,j}}{E_R}}, \tag{1.13}$$

and where the recoil energy is defined as $E_R = \hbar^2 k_L^2/(2m)$. For the potential in Eq. (1.12), the state with lowest energy is the product of normalized

Gaussian wave functions

$$w_\alpha(x_\alpha) = \frac{1}{(\pi d_\alpha^2)^{1/4}} \exp\left[-\frac{1}{2}\left(\frac{x_\alpha}{d_\alpha}\right)^2\right], \tag{1.14}$$

for $\alpha \in \{1,2,3\}$; the characteristic length d_α depends on the lattice depth

$$\frac{1}{d_\alpha} = \sqrt{\frac{m}{\hbar}}\left(\frac{2V_{0,\alpha}k_L^2}{m}\right)^{1/4} = \left(\frac{2V_{0,\alpha}k_L^2 m}{\hbar^2}\right)^{1/4}. \tag{1.15}$$

By making use of Eqs (1.9) and (1.14) and by introducing

$$U_0 = \frac{4\pi a_s \hbar^2}{m}, \tag{1.16}$$

we can compute the on-site interaction U

$$\begin{aligned}
U &\equiv U_0 \int_{\mathbb{R}^3} d\mathbf{x}|W(\mathbf{x})|^4 = U_0 \prod_{\alpha=1}^{3}\int_{\mathbb{R}} dx|w_\alpha(x)|^4 = \\
&= U_0 \prod_{\alpha=1}^{3}\frac{1}{\pi d_\alpha^2}\int_{\mathbb{R}} dx \exp\left[-2\left(\frac{x}{d_\alpha}\right)^2\right] = U_0 \prod_{\alpha=1}^{3}\frac{1}{\pi d_\alpha^2} d_\alpha\sqrt{\frac{\pi}{2}} = \\
&= U_0 \frac{1}{(2\pi)^{3/2}}\prod_{\alpha=1}^{3}\frac{1}{d_\alpha} = U_0 \frac{1}{(2\pi)^{3/2}}\prod_{\alpha=1}^{3}\left(\frac{2V_{0,\alpha}k_L^2 m}{\hbar^2}\right)^{1/4} = \\
&= \frac{4\pi a_s\hbar^2}{m\sqrt{8\pi^3}}\left(\frac{2k_L^2 m}{\hbar^2}\frac{\hbar^2 k_L^2}{2m}\right)^{3/4}\prod_{\alpha=1}^{3}\left(\frac{V_{0,\alpha}}{E_R}\right)^{1/4} = \\
&= \frac{4\pi a_s\hbar^2}{m\sqrt{8\pi}}k_L^3\prod_{\alpha=1}^{3}\left(\frac{V_{0,\alpha}}{E_R}\right)^{1/4} = \frac{8\pi}{\sqrt{8\pi^3}}\frac{\hbar^2 k_L^2}{2m}k_L a_s\prod_{\alpha=1}^{3}\left(\frac{V_{0,\alpha}}{E_R}\right)^{1/4} = \\
&= E_R\sqrt{\frac{8}{\pi}}k_L a_s\prod_{\alpha=1}^{3}\left(\frac{V_{0,\alpha}}{E_R}\right)^{1/4}.
\end{aligned} \tag{1.17}$$

Therefore, the final result for the on-site interaction coefficient in the harmonic approximation is

$$\frac{U}{E_R} = \sqrt{\frac{8}{\pi}}\,(k_L a_s)\prod_{\alpha=1}^{3}\left(\frac{V_{0,\alpha}}{E_R}\right)^{1/4}, \tag{1.18}$$

that becomes

$$\frac{U}{E_R} = \sqrt{\frac{8}{\pi}}\,(k_L a_s)\left(\frac{V_0}{E_R}\right)^{3/4}, \tag{1.19}$$

in the case of an isotropic lattice ($V_{0,j} = V_0$ for any $j \in \{1,2,3\}$).

For a later purpose, we note that the Wannier function in momentum space (i.e. the Fourier transform of Eq. 1.14) reads

$$w_\alpha(k_\alpha) = \frac{1}{(\pi\sigma_\alpha^2)^{1/4}} \exp\left[-\frac{1}{2}\left(\frac{k_\alpha}{\sigma_\alpha}\right)^2\right], \tag{1.20}$$

where the characteristic size is the inverse of d_α:

$$\sigma_\alpha = \frac{1}{d_\alpha} = \frac{2\pi}{\lambda}\left(\frac{V_{0,\alpha}}{E_R}\right)^{1/4}. \tag{1.21}$$

1.3 Band structure calculation of J

In this section we describe a scheme to derive the hopping coefficient J, based on the calculation of the band structure of the lattice. We start from the following one-particle Hamiltonian in one-dimension

$$\begin{aligned} H_1 &= \frac{-\hbar^2}{2m}\nabla^2 + V_0 \sin^2\left(\frac{\pi x}{a}\right) = \\ &= \left(\frac{-\hbar^2}{2m}\nabla^2 + \frac{V_0}{2}\right) - \frac{V_0}{4}\left(e^{+i\frac{2\pi x}{a}} + e^{-i\frac{2\pi x}{a}}\right), \end{aligned} \tag{1.22}$$

the eigenfunctions of which can be written through Bloch's theorem as

$$\psi_q(x) = e^{iqx}u(x), \tag{1.23}$$

where q is the quasi-momentum and we are dropping the band index n since we are considering a single-band model (as explained in section 1.1). The function $u(x)$ has the same periodicity of the potential, i.e. $u(x+a) = u(x)$, thus its Fourier decomposition reads

$$u(x) = \sum_p d_p e^{\frac{2\pi}{a}px}, \tag{1.24}$$

where p is an integer index.

The Schrodinger equation $H_1\psi_q(x) = E(q)\psi_q(x)$ can be rewritten as

$$\left\{\left[-\frac{\hbar^2}{2m}\left(\frac{2\pi}{a}p + q\right)^2 + \frac{V_0}{2}\right]\delta_{p,p'} - \frac{V_0}{4}\left(\delta_{p-1,p'} + \delta_{p+1,p'}\right)\right\} d_{p'} = E(q)d_p, \tag{1.25}$$

by making use of Eqs (1.23) and (1.24) and of the orthogonality property of plane waves. Eq. (1.25) is an eigenvalue problem, from which we can find the lowest eigenvalue $E_0(q)$ and the corresponding eigenstate $\vec{d}$ (both as functions of the quasi-momentum q). Note that a certain interval $\{-p_{\max}, .., 0, .., +p_{\max}\}$ has to be chosen for p and p', so that computing the bands for one choice of q corresponds to the diagonalization of a

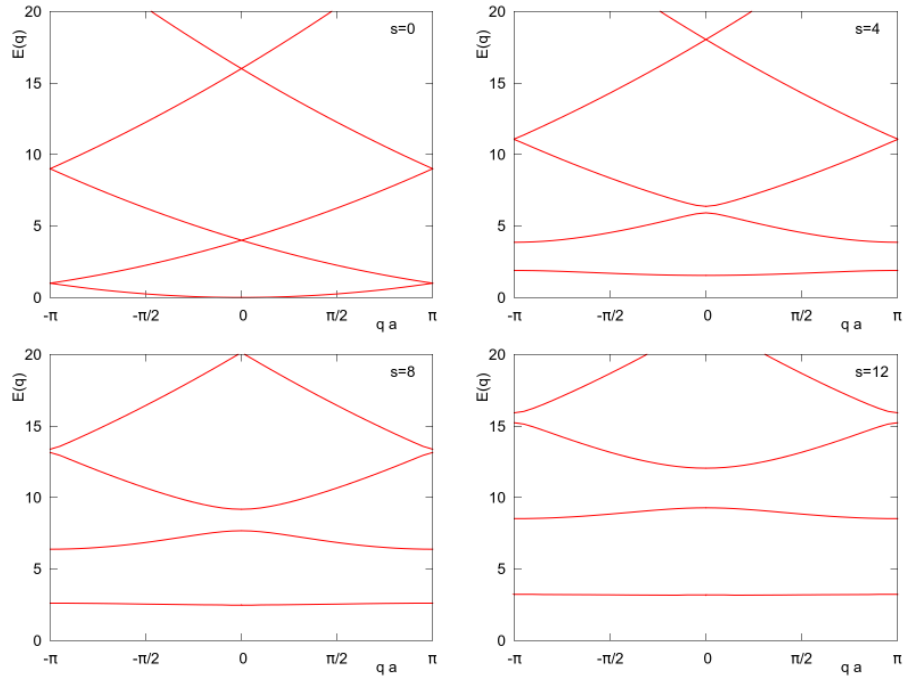

Figure 1.2: Band dispersion for different lattice depths $s \equiv V_0/E_R$, computed solving Eq. (1.25) for different values of qa and $p_{\max} = 5$ (see text).

$(2p_{\max} + 1) \times (2p_{\max} + 1)$ matrix. Some examples of the band energy dispersion $E_n(q)$ are shown in Fig. 1.2; it can be noted that the single-band approximation is not a good assumption for very shallow lattice, in which the gap to the first band is smaller.

The energy spectrum is related to the hopping parameter J_R between two sites at distance Ra by the following relation [25]

$$\sum_R e^{iqaR} = E_0(q), \tag{1.26}$$

where we are only considering the lowest energy level E_0 on each site. If Eq. (1.26) is evaluated for a certain number D of values of q, this leads to a linear system of D equations in D variables that can be solved to find $\{J_1, .., J_D\}$. In our calculation we have chosen $D = 6$, after verifying that a larger value of D does not change the results for J_R (with $R \leq 3$). In Table 1.1 we show the results for the nearest-neighbour and next-nearest-neighbour coefficients J_1 and J_2, that are in agreement with the ones in Ref. [29]. We notice that J_1 is always negative, meaning that there is a gain in energy in nearest-neighbour hopping, whereas the next-nearest-neighbour hopping is not energetically favourable. Moreover, $|J_2|$ is always smaller than $|J_1|$ and for realistic lattice depths the ratio $|J_2/J_1|$ is lower than $1/10$;

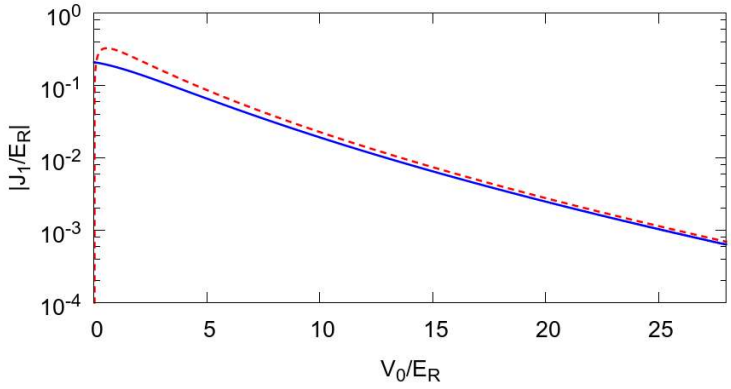

Figure 1.3: Nearest neighbour hopping parameter (in semilog scale) as a function of the lattice depth. Results are obtained through Eq. (1.27) (dashed line) and band structure calculations (solid line).

in the same way, the values of J_R are strongly suppressed for larger R. This is a justification for neglecting all the hopping processes with $R \geq 2$.

V_0/E_R	J_1/E_R	J_2/E_R
2	-0.14276	0.02039
4	-0.08549	0.00615
8	-0.03080	0.00064
12	-0.01225	0.00009
16	-0.00533	0.00001

Table 1.1: Nearest-neighbour and next-nearest-neighbour hopping coefficients J_1 and J_2 for different lattice depths.

So far, we have only considered the energy dispersion and hopping parameters for a one dimensional system. In the case of a separable lattice, the dimensionality does not affect the value of the hopping parameter; this is because we restrict our model to nearest-neighbour hopping processes, that happen only along one of the possible directions. Thus one only needs to know the value of J_1 for the 1D model. On the contrary, for a non-separable lattice the hopping coefficients would have to be computed explicitly for the system with the correct dimensionality.

Considering the case of a separable isotropic lattice, an approximate expression for the nearest-neighbour hopping coefficient J based on the solution of the Mathieu equation is given in Ref. [30]:

$$\frac{J}{E_R} = \frac{4}{\sqrt{\pi}} \left(\frac{V_0}{E_R}\right)^{3/4} \exp\left(-2\sqrt{\frac{V_0}{E_R}}\right). \tag{1.27}$$

In Figure 1.3 we compare the formula in Eq. (1.27) with the results of our band-structure calculation.

1.4 Homogeneous phase diagram

It was first predicted by Matthew Fisher and collaborators in 1989 (Ref. [2]) that the zero temperature phase diagram of the homogeneous Bose-Hubbard model

$$H = -J \sum_{\langle i,j \rangle} \hat{b}_i^\dagger \hat{b}_j + \frac{U}{2} \sum_i \hat{b}_i^\dagger \hat{b}_i^\dagger \hat{b}_i \hat{b}_i - \mu \sum_i \hat{b}_i^\dagger \hat{b}_i, \tag{1.28}$$

includes two different phases: a Mott-insulator phase in which a fixed (integer) number of particles are localized on every site and a superfluid phase in which particles are delocalized over a large region of the lattice. Here we describe the characteristic of the two phases and give some results for the phase diagram.

Large U/J: Mott insulating phase

If the repulsive on-site interaction is dominating ($U/J \geq 1$) and the number of particles N is commensurate with the number of sites N_s, the ground state of Eq. (1.28) is a Mott insulator. The extreme case is the one of vanishing hopping coefficient ($J \equiv 0$), that has the ideal Mott insulator state as an exact solution. This is the product of local Fock states with the same number n_0 ($n_0 \equiv N/N_s$) of particles on every site

$$|\psi_{\mathrm{MI}}\rangle \equiv |\psi_{\mathrm{MI}}\rangle_{J=0} \propto \prod_{i=1}^{N_s} \left(\hat{b}_i^\dagger\right)^{n_0} |0\rangle. \tag{1.29}$$

This state has no occupation number fluctuations, all the sites host exactly n_0 particles. For a small but finite value of J/U, perturbation theory [31] leads to a state that is a dilute gas of particle/hole pairs immersed in a "sea" of sites with local density $n_i = n_0$

$$|\psi_{\mathrm{MI}}\rangle_{J/U} \approx |\psi_{\mathrm{MI}}\rangle + \frac{J}{U} \sum_{\langle i,j \rangle} \hat{b}_i^\dagger \hat{b}_j |\psi_{\mathrm{MI}}\rangle, \tag{1.30}$$

where particle/hole excitations (also called doublon/holon) are only localized on neighbouring sites (up to first order in J/U).

Some features of the Mott state are: (a) the order parameter $\psi \equiv \langle b_i \rangle$ vanishes; (b) there is a gap in the excitation spectrum because the lowest excitation is the creation of a particle-hole pair (corresponding to an energy of $n_0 U$); (c) the compressibility $\kappa = \frac{\partial n}{\partial \mu}$ vanishes, i.e. the density remains constant as the chemical potential increases (in a certain range) and (d) the fluctuations of the number of particles per site are suppressed.

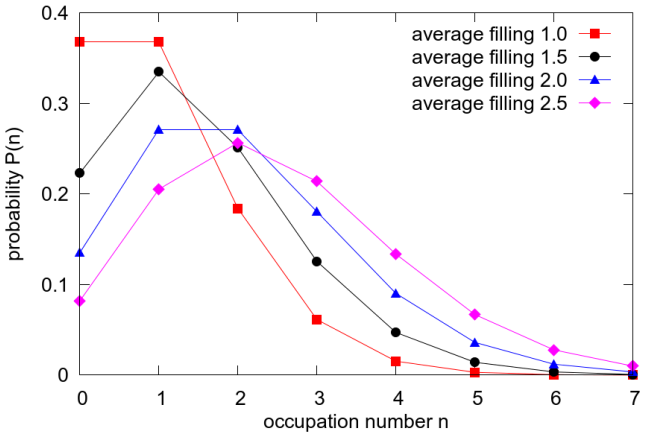

Figure 1.4: Local occupation number distribution in the ideal superfluid state (Eq. 1.31), for $U/J = 0$.

Small U/J: superfluid phase

If the kinetic term is dominating, the system reaches a superfluid phase, in which each single-particle state is delocalized over the lattice. For the ideal case of vanishing interaction ($U/J = 0$), the exact many-particle ground-state is

$$|\psi_{\mathrm{SF}}\rangle \propto \left(\hat{b}_{k=0}^{\dagger}\right)^{N} |0\rangle \propto \left(\sum_{i=1}^{N_s} \hat{b}_i^{\dagger}\right)^{N} |0\rangle. \tag{1.31}$$

In this state, the local density distribution $P(n)$ is a binomial distribution (see Ref. [32])

$$P(n) = \frac{e^{-N/N_s}}{n!} \left(\frac{N}{N_s}\right)^{n}. \tag{1.32}$$

Some examples of this distribution are shown in Fig. 1.4, where it can be noticed that $P(n)$ is not sharply peaked on a single local density n_0. As a comparison, in the ideal Mott state (Eq. 1.29) we have $P(n) = \delta_{n,n_0}$.

The presence of local density fluctuations is one of the features of the superfluid phase, not only in the ideal case of vanishing interactions. Other features include (a) the absence of an energy gap, (b) the finiteness of the compressibility (this is seen in the monotonic increase of the density for increasing chemical potential) and (c) the finiteness of the order parameter: $|\psi| > 0$.

Phase diagram

As we have described, the limit of weak interaction (strong interaction and commensurate filling) corresponds to a superfluid (Mott insulator) phase.

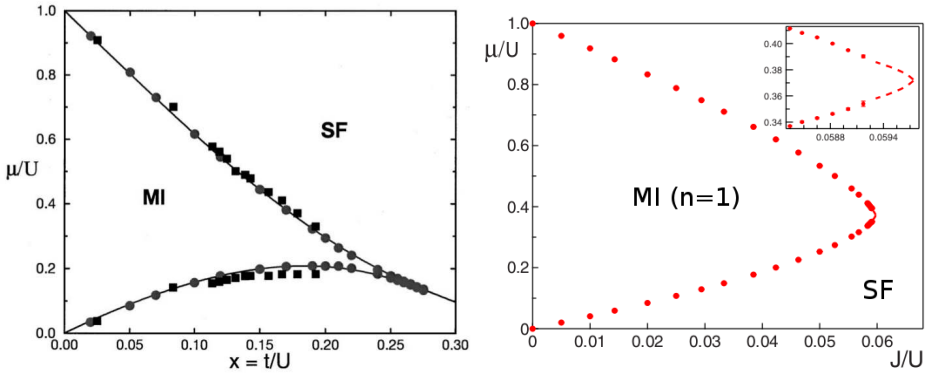

Figure 1.5: Left: phase diagram of the homogeneous one-dimensional Bose-Hubbard model (t corresponds to the hopping coefficient J); squares are QMC results (Ref. [33]), circles are DMRG results (Ref. [34]), the solid line is a strong-coupling expansion. Figure extracted from Ref. [35]. Right: boundaries of the first Mott lobe in the phase diagram of the homogeneous two-dimensional Bose-Hubbard model, obtained through QMC calculations. The inset shows a detailed view of the region of the tip. Figure adapted from Ref. [36].

Varying the ratio U/J or changing the chemical potential μ can lead to a phase transition.

In particular, we consider the $(J/U)-(\mu/U)$ phase diagram, that is characterized by some lobes (for low values of J/U) inside which the system is in the Mott phase with an integer filling factor; outside these lobes, the system is in the superfluid phase. The lines of fixed density do not correspond to lines of fixed chemical potential. In Fig. 1.5 we show accurate calculations of the first Mott lobe (i.e. the one with local density pinned to $n_0 = 1$) in 1D and 2D. They are qualitatively different, while the one in 3D is qualitatively the same as in 2D. When the boundary of a lobe is crossed, a quantum phase transition takes place. Depending on whether the crossing happens at fixed density or at fixed U/J, the transition has different universality properties [2].

In a site-decoupled mean-field approach (see section 3.2.2), the dimensionality of the system only enters the mean-field Hamiltonian through a rescaling of J by the connectivity z, that is the number of nearest neighbours of each site ($z = 2d$ for a d-dimensional hypercubic lattice). For this reason, the mean-field $(zJ/U) - (\mu/U)$ phase diagram does not depend on the dimensionality. In Fig. 1.6 we show the first Mott lobes computed by this mean-field approach; by a comparison with Fig. 1.5 it can be noted that the 1D mean-field phase diagram is qualitatively different from the real one, while in higher dimensions there is only a quantitative difference in the position of the lobe tips.

The phase diagram changes when other effects are taken into account. The inclusion of longer-range interactions is described in section 1.7 and has been treated for instance in Refs [34, 8, 10]. The way in which the phase diagram changes for finite temperatures has been studied in Refs [37, 38, 39].

1.5 Inhomogeneous system: shell structure

As mentioned in section 1.1, in an experimental set-up the atoms are confined in space by a magnetic trap. In this section we describe the trapping potential and the resulting shell structure in the local observables. The main point here is that the trapping potential (i.e. the term $\sum_i \epsilon_i n_i$ in the full Hamiltonian Eq. 1.7) breaks the homogeneity of the system; therefore there is not a single global phase of the system, but coexistence of different phases is allowed. For the same reason, the superfluid-Mott insulator phase transition is replaced by a phase crossover.

The trapping potential includes two different contributions: an external magnetic trap and the confinement due to the waist of the laser beams that are used to create the optical lattice. For an optical lattice as in Eq. (1.4) and for a trapping potential as in Eq. (1.3), the frequency of the harmonic trap along the x direction is

$$\omega_x^T = \sqrt{\omega_m^2 + \frac{4}{m}\left(\frac{V_{0,y}}{w_y^2} + \frac{V_{0,z}}{w_z^2}\right)}, \tag{1.33}$$

where ω_m is the frequency of the (isotropic) external magnetic trap and w_y (w_z) is the waist of the laser beam along the y (z) direction. Analogous relations hold for ω_y^T and ω_z^T. In case of an isotropic lattice (with the same lattice depth V_0 and the same beam waist w in every direction), the trapping frequency reads [40]

$$\omega^T = \sqrt{\omega_m^2 + \frac{8V_0}{mw^2}}. \tag{1.34}$$

In Ref. [41], a correction to this expression has been proposed, to take into account "*the modification of the vibrational ground state energy in each well due to the spatial variations of the laser intensities on the scale w*". The corrected expression for the isotropic case reads

$$\omega^T = \sqrt{\omega_m^2 + \frac{4(2V_0 - \sqrt{V_0})}{mw^2}}. \tag{1.35}$$

Independently from the strength of the trapping potential, its presence makes it favourable an accumulation of the particles close to the center of the trap. When the local density in the center is larger than one, there is a competition between the trapping potential and the repulsive on-site

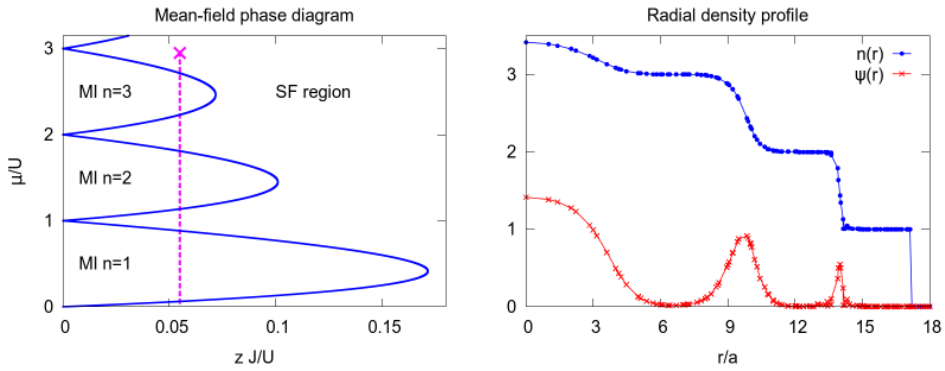

Figure 1.6: Left: mean-field phase diagram for the homogeneous system (solid lines), chemical potential in the center of the trap (cross mark), effective local chemical potential in the trapped system (dashed vertical line). Right: radial dependence of the density (filled circles) and order parameter (crosses), obtained through the inhomogeneous site-decoupled mean-field approach described in section 3.2.2.

interaction, since the latter favours a spread of the density over a larger region. This competition leads to a shell structure for the density profile, meaning that along the radial direction the system is in a sequence of Mott and superfluid shells.

A first way of understanding this structure is the use of the Local Density Approximation, based on the fact that the trapping potential changes slowly on the typical system size. In this approximation, the trapping potential is included in an effective local chemical potential $\tilde{\mu}_i$

$$\tilde{\mu}_i = \mu - \epsilon_i, \tag{1.36}$$

and for each site i the homogeneous system with chemical potential $\tilde{\mu}_i$ is studied. In this approximation, the effective chemical potential in the center of the trap corresponds to μ, while in all the other sites $\tilde{\mu}_i < \mu$ and $\tilde{\mu}_i$ decreases with the distance from the center. If we put this set of effective chemical potentials in the homogeneous phase diagram (see Fig. 1.6) we see that for certain values of J/U this vertical line crosses different regions (corresponding to different phases).

This approximate explanation for the shell structure of the inhomogeneous Bose-Hubbard model is confirmed by approaches that take into account the inhomogeneity by studying the full Hamiltonian. In Figure 1.6 an example is shown of the shell structure, computed through the inhomogeneous mean-field approach described in Chapter 3. The formation of a structure including shells of different phases has been studied both numerically (Refs [42, 43]) and in experiments (Ref. [44]).

1.6 Time-of-flight measurements

One of the experimental techniques most frequently used to study a system of cold atoms in an optical lattice is the measurement of the momentum distribution via time-of-flight images. This is part of the following experimental sequence

1. a Bose-Einstein condensate is prepared at low temperature (order of $10^0 - 10^2$ nK), and a trapping potential is used to confine it in a finite region;

2. the laser beams needed to produce the optical lattice are slowly turned on and their intensity is increased up to the required value of V_0;

3. the system is kept on hold for a certain time interval;

4. all the potentials (the trapping potential and the lattice created by laser beams) are suddenly turned off; the particles are now free and move as plane-waves with a certain momentum $\mathbf{k}$;

5. after a certain time interval τ, the particles are detected on a camera through absorption imaging of the atom cloud, leading to a map of the optical density distribution.

What is observed through this images is a density distribution in real space $N_{\text{tof}}(\mathbf{r})$. Assuming that when all the potentials are turned off the motion of the particle is free, this interference pattern in real space is interpreted as a distribution of momentum

$$N_{\text{tof}}(\mathbf{r})|_{\mathbf{k}=\frac{m\mathbf{r}}{\hbar\tau}} = \left(\frac{m}{\hbar\tau}\right) |W(\mathbf{k})|^2 \, S(\mathbf{k}), \tag{1.37}$$

where $S(\mathbf{k})$ is defined as

$$S(\mathbf{k}) \equiv \sum_{i,j} e^{i\mathbf{k}\cdot(\mathbf{r}_i - \mathbf{r}_j)} \langle \hat{b}_i^\dagger \hat{b}_j \rangle, \tag{1.38}$$

and $n(\mathbf{k})$ is the product of $S(\mathbf{k})$ and the Wannier envelope

$$n(\mathbf{k}) = |W(\mathbf{k})|^2 S(\mathbf{k}). \tag{1.39}$$

Some approximations are implied, when mapping the optical density observed in real space to the interference pattern $n(\mathbf{k})$, as done in Eq. (1.37). This approach neglects the role of interaction during the expansion (after the trap and lattice are turned off, the motion of particles is assumed to be free) and corrections due to the finiteness of the time interval τ. According to Ref. [45], these measurements are analogous to the observation of an interference pattern in classical optics, in which a far-field condition is usually assumed.

The corresponding far-field condition in case of time-of-flight measurements is that τ should be much larger than a time-scale τ_{ff} proportional to the characteristic coherence length. For a shallow lattice (i.e. for a small U/J) the coherence length is large and τ_{ff} would be larger than the one typically used (see Ref. [45]).

We note that the difference between $n(\mathbf{k})$ and $S(\mathbf{k})$ is the Wannier envelope $|W(\mathbf{k})|^2$. Given the results derived in section 1.2, we are able to evaluate this envelope explicitely (in the harmonic approximation for the lattice wells) for any value of $\mathbf{k}$.

Another feature of time-of-flight measurements is that only a 2D image is detected in the experiments, rather than a map of the full 3D $n(\mathbf{k})$. What is measured is $n_\perp(k_x, k_y)$, defined as the integral of $n(\mathbf{k})$ along the probe line k_z:

$$n_\perp(k_x, k_y) = \int_{-\infty}^{+\infty} n(\mathbf{k}) dk_z = \int_{-\infty}^{+\infty} |W(\mathbf{k})|^2 S(\mathbf{k}) dk_z. \tag{1.40}$$

In the same way, $S_\perp(k_x, k_y)$ is defined as

$$S_\perp(k_x, k_y) = \frac{n_\perp(k_x, k_y)}{|w_1(k_x) w_2(k_y)|^2}. \tag{1.41}$$

The time-of-flight measurements that we have described have represented the first experimental signature of the phase transition introduced in section 1.4. In fact in the ideal superfluid phase there is a large phase coherence and $n(\mathbf{k})$ shows some sharp interference peaks, while in the Mott state the number of particles is fixed on every site and the phase fluctuates, leading to a flat interference pattern (up to some small fluctuations).

In 2002, Markus Greiner and collaborators (Ref. [4]) performed this kind of measurements for different lattice depths. The results (Fig. 1.7) show that for increasing values of V_0 (corresponding to increasing values of U/J) the interference peaks smear out and only a uniform background remains. From Fig. 1.7 it can be also noted that what is observed is $n(\mathbf{k})$ and not $S(\mathbf{k})$, since the Wannier envelope suppresses the secondary peaks w.r.t. the central one.

1.7 Extended Bose-Hubbard model

For a system of atoms or molecules with a large dipole momentum, dipole-dipole long-range interactions are present in addition to the on-site repulsion (see Ref. [27] for an extended review). Here we consider the one-dimensional extended Bose-Hubbard model for N bosons on a L-sites chain with periodic boundary conditions (PBC), described by the Hamiltonian

$$H = -t \sum_{i=1}^{L} \left(b_i^\dagger b_{i+1} + b_{i+1}^\dagger b_i \right) + \frac{U}{2} \sum_{i=1}^{L} n_i(n_i - 1) + V \sum_{i=1}^{L} n_i n_{i+1}, \tag{1.42}$$

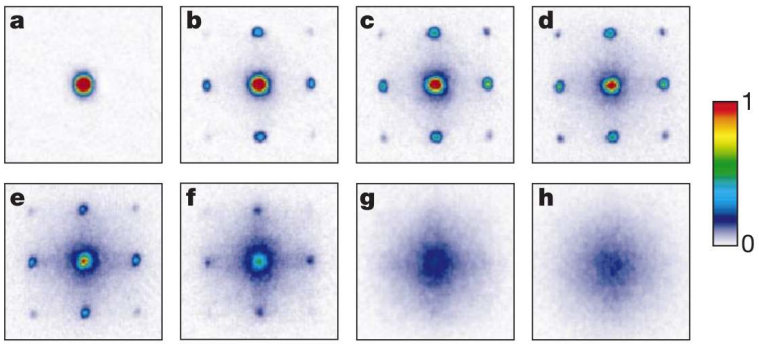

Figure 1.7: Time-of-flight measurements of $n_\perp(k_x, k_y)$ for different lattice depths, from (a) to (h) $V_0/E_R = 0, 3, 7, 10, 13, 14, 16, 20$. Figure extracted from Ref. [4].

in which the term proportional to V corresponds to a repulsive interaction between bosons on neighbouring sites, due to dipole-dipole interactions.

Because of the presence of the long-range repulsion, the phase diagram includes also a charge density wave (CDW) phase, in addition to the superfluid and Mott insulator ones; this phase is characterized by periodic density fluctuations around the average filling. In Ref. [34], this system was studied in the gran-canonical ensemble (i.e. with a chemical potential μ to regulate the number of particles) and it was shown how the phase diagram described in section 1.4 changes to include lobes of CDW phase (Fig. 1.8).

More recently, in a series of work (Refs [8, 9, 10]) the extended Bose-Hubbard model in one dimension has been studied at unit filling and it has been proposed that the long-range repulsion (either truncated to a distance of one or three) can stabilize a fourth phase (the Haldane insulator), that is insulating but distinct from the Mott phase. In Fig. 1.9 the $T = 0$ phase diagram is shown (for the case of repulsion truncated to the nearest neighbours).

In order to characterize the different phases of this system, we introduce the following set of correlation functions

$$C_{\mathrm{SF}}(r) = \langle \hat{b}_j^\dagger \hat{b}_{j+r} \rangle, \tag{1.43}$$

$$C_{\mathrm{DW}}(r) = (-1)^r \langle \delta\hat{n}_j \delta\hat{n}_{j+r} \rangle, \tag{1.44}$$

$$C_{\mathrm{par}}(r) = \left\langle \exp\left[i\pi \sum_{p=j}^{j+r-1} \delta\hat{n}_p \right] \right\rangle, \tag{1.45}$$

$$C_{\mathrm{str}}(r) = \left\langle \delta\hat{n}_j \exp\left[i\pi \sum_{p=j}^{j+r-1} \delta\hat{n}_p \right] \delta\hat{n}_{j+r} \right\rangle, \tag{1.46}$$

where we have defined $\delta\hat{n}_j \equiv (\hat{n}_j - 1)$ and $\hat{n}_j \equiv \hat{b}_j^\dagger \hat{b}_j$. The first two correlators

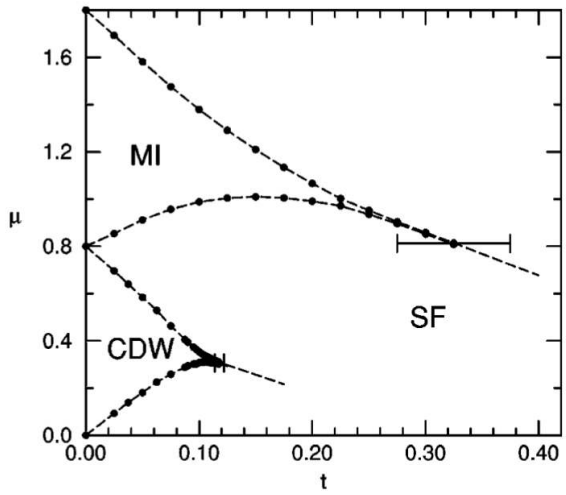

Figure 1.8: Phase diagram of the homogeneous one-dimensional Bose-Hubbard model with nearest-neighbour repulsive interaction($t \equiv J$, $U = 1$, $V = 0.4$). The phases are: Mott insulator with filling one (MI), charge density wave with filling one half (CDW) and superfluid (SF). Circles represent DMRG results. Figure extracted from Ref. [34].

are local, i.e. they are of the form

$$C(r) = C(j, j+r) = \langle \hat{A}(j)\hat{B}(j+r)\rangle, \tag{1.47}$$

whereas the *parity* and *string* correlation functions (Eqs 1.45 and 1.46) are non-local, i.e. $C(j, j+r)$ depends on all the sites between the sites j and $(j+r)$.

The classification of the phases of the system is based on the infinite-distance limit of the correlation functions introduced in Eqs (1.43) - (1.46); in practice most numerical methods deal with finite systems, thus the infinite-r limit is replaced by the maximum distance $r_{\max}$ allowed on the lattice and a finite size scaling of the results is performed afterwards. The classification of the phases based on the order parameters is the following [11]

phase	$C_{\mathrm{SF}}(\infty)$	$C_{\mathrm{DW}}(\infty)$	$C_{\mathrm{par}}(\infty)$	$C_{\mathrm{str}}(\infty)$
superfluid	$\neq 0$	0	0	0
Mott insulator	0	0	$\neq 0$	0
Haldane insulator	0	0	0	$\neq 0$
density wave	0	$\neq 0$	$\neq 0$	$\neq 0$

In Fig. 1.9 we show the phase diagram of this model obtained through DMRG, from Ref. [10]. This is computed with a maximum occupation number of 3 bosons per site and using open boundary conditions (two op-

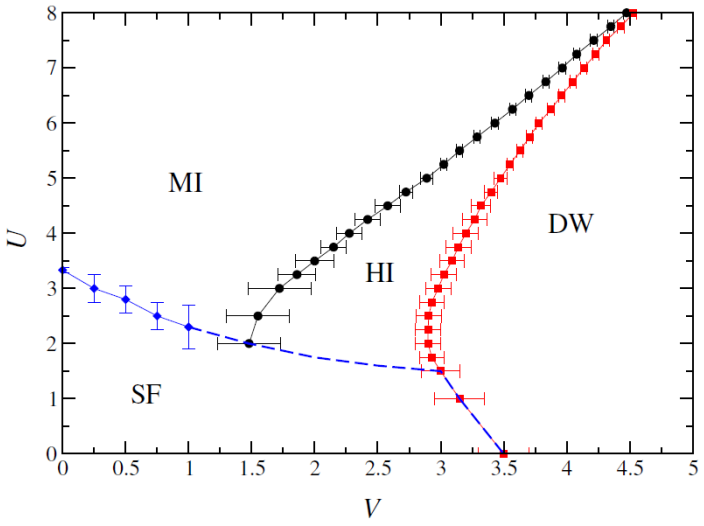

Figure 1.9: Phase diagram of the extended Bose-Hubbard model (Eq. 1.42), from Ref. [10]. Energies in units of J.

posite biases have been added at the left and right boundaries of the chain, in order to lift the ground state degeneracy).

Chapter 2

Visibility in the trapped system

As described in section 1.5, the presence of a trapping potential leads to a coexistence of different phases in the system. For very small values of U/J (corresponding to a shallow lattice), the system is a single superfluid domain; as U/J increases (corresponding to an increase of the lattice depth V_0/E_R), the Mott shells with integer filling appear.

In order to characterize the phase diagram of the system, there has been a large effort aimed at finding some experimentally measurable quantities that can be used to probe the appearance of Mott domains. In many of the experiments, time-of-flight images are taken, and the integrated interference pattern $n_\perp(k_x, k_y)$ is measured. Different quantities can be extracted from these data: in some studies (Refs [4, 46]) the width of the interference peak has been considered, while other authors have used the integral of the peak (Refs [47, 48]) or the peak weight (Ref. [49]).

Another way of characterizing the phase crossover is the visibility $\mathcal{V}$ of the interference pattern, that is a measure of the coherence of the system; this has been used for instance in Refs [31, 40, 50, 45, 51, 28].

In this chapter we first define and describe this quantity (section 2.1) and we review an experimental work (Ref. [31]) in which the visibility gives signatures of the appearance of Mott shells; this is linked to the presence of non-smooth features (kinks) in the plot of $\mathcal{V}$ as a function of V_0/E_R. The results from Ref. [31] have been later compared with different numerical simulations. QMC simulations of one-dimensional systems (reviewed in section 2.3) have been used to study the origin of the kinks. More recent QMC studies have achieved a quantitative description of the visibility by simulating 2D or 3D systems of experimentally relevant sizes, but no kinks have been observed; these studies are reviewed in section 2.4. In section 2.5 we mention the presence of kinks in the visibility for another experimental set-up, namely a triangular optical lattice (Ref. [28]).

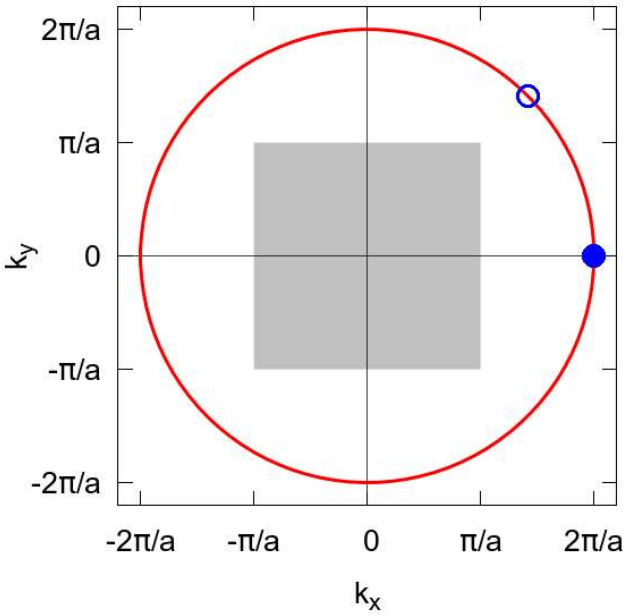

Figure 2.1: Position of $\mathbf{k}_{\max}$ (filled circle) and $\mathbf{k}_{\min}$ (empty circle); the shaded area corresponds to the first Brillouin zone.

2.1 Visibility

Given the definition of the integrated interference pattern $n_\perp(k_x, k_y)$ (Eq. 1.40), we define its visibility $\mathcal{V}$ as in Ref. [31]:

$$\mathcal{V} = \frac{n_\perp(\mathbf{k}_{\max}) - n_\perp(\mathbf{k}_{\min})}{n_\perp(\mathbf{k}_{\max}) + n_\perp(\mathbf{k}_{\min})}, \tag{2.1}$$

where

$$\mathbf{k}_{\max} = \left(\frac{2\pi}{a}, 0\right), \tag{2.2}$$

$$\mathbf{k}_{\min} = \left(\frac{2\pi}{a\sqrt{2}}, \frac{2\pi}{a\sqrt{2}}\right), \tag{2.3}$$

and where a is the lattice spacing. The definition of $\mathbf{k}_{\max}$ and $\mathbf{k}_{\min}$ is such that $\mathbf{k}_{\max}$ is the center of one of the interference peaks of $n_\perp$ (since this is the center of the second Brillouin zone), while $\mathbf{k}_{\min}$ is part of the incoherent background of $n_\perp$. Therefore, the visibility is a contrast measurement between the maximum and minimum values of $n_\perp$. The reason for the specific choice of $\mathbf{k}_{\min}$ and $\mathbf{k}_{\max}$ is that the Wannier functions in these two points are equal

$$|w_1(k_x)w_2(k_y)|^2_{\mathbf{k}_{\min}} = |w_1(k_x)w_2(k_y)|^2_{\mathbf{k}_{\max}}, \tag{2.4}$$

because they are at the same distance from the origin (as shown in Fig. 2.1). Therefore, the Wannier envelope factorizes and cancels in Eq. (2.1) and the visibility reads

$$\begin{aligned}\mathcal{V} &= \frac{\left(S_\perp(\mathbf{k}_{\max}) - S_\perp(\mathbf{k}_{\min})\right)\left|w_1(k_x)w_2(k_y)\right|^2_{\mathbf{k}_{\max}}}{\left(S_\perp(\mathbf{k}_{\max}) + S_\perp(\mathbf{k}_{\min})\right)\left|w_1(k_x)w_2(k_y)\right|^2_{\mathbf{k}_{\max}}} = \\ &= \frac{S_\perp(\mathbf{k}_{\max}) - S_\perp(\mathbf{k}_{\min})}{S_\perp(\mathbf{k}_{\max}) + S_\perp(\mathbf{k}_{\min})}.\end{aligned} \tag{2.5}$$

This quantity is a measure of the coherence of the system, useful to characterize its phase. In the superfluid phase there is coherence among particles on different sites and $n_\perp(k_x, k_y)$ shows sharp interference peaks; this leads to a visibility close to unity (or identically one, for the homogeneous system in the thermodynamic limit). On the contrary, for a homogeneous system in the ideal Mott phase ($J/U = 0$) the local number of particles is fixed while the local phase is not; this leads to a homogeneous $n_\perp(k_x, k_y)$ distribution and to a vanishing visibility. In the trapped system there is not a single global phase, thus the visibility can in principle take any intermediate value between $\mathcal{V} = 0$ and $\mathcal{V} = 1$.

Moreover, the experimental results for the visibility $\mathcal{V}$ typically include also other effects

- when extracting $n_\perp(\mathbf{k}_{\max})$ and $n_\perp(\mathbf{k}_{\min})$, these are averaged over a certain region around the specific points (e.g. in Ref. [31] this is a region of 3×3 pixels), to reduce the signal-to-noise ratio;
- $n_\perp(\mathbf{k}_{\max})$ and $n_\perp(\mathbf{k}_{\min})$ are averaged over the four copies of $\mathbf{k}_{\max}$ and $\mathbf{k}_{\min}$ obtained by rotations of $\pi/2$, π and $3\pi/2$;
- these quantities are also averaged over different time-of-flight images, extracted from successive measurements.

2.2 First observation of kinks in $\mathcal{V}$

Refs [31, 40] are the first works in which the visibility of the quasimomentum distribution is used to study the Mott-insulator transition of a bosonic gas in an optical lattice. The experimental set-up consists in a system of ^{87}Rb atoms (scattering length $a_s \simeq 5.45$ nm) in a 3D optical lattice (laser wavelength $\lambda = 850$ nm, lattice spacing $a = 425$ nm, recoil energy $E_R \approx h \times 3.2$ KHz). The number of particles is of the order of $10^5 - 10^6$, corresponding to approximately 3 particles per site in the center of the trap. The intensity of lattice potential is varied in the range $V_0/E_R \in [5, 30]$.

The results for the visibility (Fig. 2.2) show the expected behaviour, i.e. $\mathcal{V}$ is close to unity for shallow lattices and it decreases for large values of V_0.

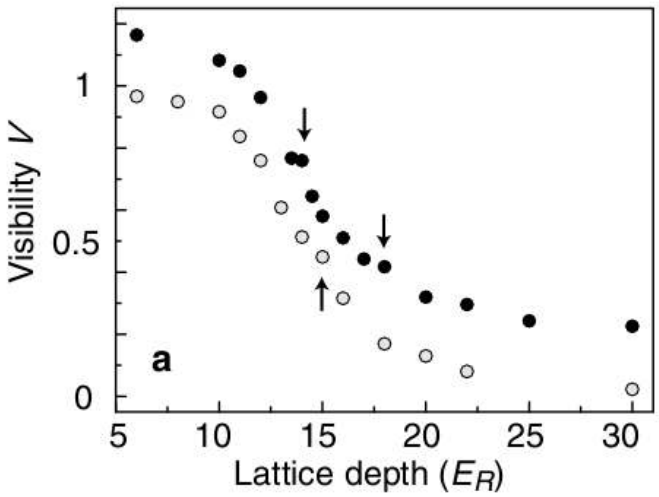

Figure 2.2: Visibility as a function of the lattice depth for a system of 3.6×10^5 atoms (gray circles) and 5.9×10^5 atoms (black circle). The second dataset is vertically shifted for clarity. Figure adapted from Ref. [31].

In particular the behaviour for large V_0 is in agreement with the estimate

$$\mathcal{V} \propto \frac{J}{U}, \tag{2.6}$$

obtained perturbatively for the homogeneous system via a first order expansion in terms of J/U (corresponding to the wave function in Eq. 1.30). Other details about the regime of deep lattice wells are given by the same authors in Ref. [40], in which a better estimate of the visibility is obtained by computing it through the Green's function within the Random-Phase Approximation.

Another feature that can be observed in Fig. 2.2 is the presence of kinks in the visibility, i.e. points in which the decay of $\mathcal{V}$ is not smooth; these can be easily recognized by looking at the numerical derivative of the data. These kinks are "systematically observed" in "reproducible positions", and they appear at values of V_0/E_R close to the ones at which the Mott shells with $n = 2$ or $n = 3$ particles per site are supposed to form. The explanation proposed by the authors is that "the observed kinks are linked to a redistribution in the density as the superfluid shells transform into MI regions with several atoms per site".

2.3 Interpretation by QMC in 1D

After the experimental results described in the previous section were published, P. Sengupta and collaborators (Ref. [50]) proposed an explanation

of the kinks in the visibility, based on a QMC study of the one dimensional Bose-Hubbard model in the trap [1].

The authors perform a study for fixed number of particles and describe two different cases: in the first one the local occupation number does not reach two, so that only the Mott domain with $n = 1$ can form, whereas in the second case also the Mott domain with $n = 2$ is present.

In the first case, for increasing U/J two kinks are observed in the (decreasing) visibility: a less evident one at $U/J = 6.3$ and a second one around $U/J = 7.1$ (see Fig. 2.3(a)). The first kink is related to the emergence of two Mott plateaux on the sides of the central superfluid region, while the second one is related to the formation of a full Mott domain in the middle of the trap.

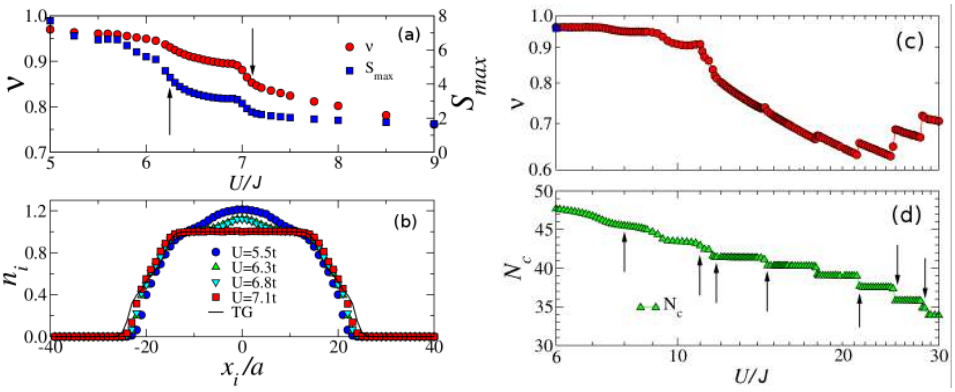

Figure 2.3: Left: 40 bosons on 80 sites, trapping potential $V_{\mathrm{T}}(i) = (0.01\ J)i^2$, less than two particles per site. (a) Visibility $\mathcal{V}$ and $(\max S(k))$, kinks at $U/J \simeq 6.3$ and 7.1. (b) Density profiles for different values of U/J (t corresponds to the hopping parameter J). Right: 60 bosons on 80 sites, trapping potential $V_{\mathrm{T}}(i) = (0.06\ J)i^2$. (c) Visibility $\mathcal{V}$ (d) Number of particles N_c in the center of the trap, i.e. the sites $i \in [-10, 10]$. Figures adapted from Ref. [50].

For intermediate values of U/J (i.e. between the two kinks), the density profile does not change (see Fig. 2.3(b)). This might seem in contrast with the finite compressibility of the superfluid domain in the center of the trap, but the reason is that this domain is trapped between the Mott regions. Thus, particles can move from the center to the boundaries (where the

[1] In the previous section we have explained how the choice of the points $\mathbf{k}_{\min}$ and $\mathbf{k}_{\max}$ matters in the definition of the visibility; in 1D the Brillouin zone is just the interval $[-\frac{\pi}{a}, \frac{\pi}{a}]$ and there are no such points with the property of being at the same distance from the origin. Moreover, in the theoretical works described in this section the system is truly one-dimensional, thus no integration over k_z is needed. Therefore, the visibility in 1D is defined directly as in Eq. (2.5), by replacing $S_\perp(k_{\max})$ and $S_\perp(k_{\min})$ with the maximum and minimum of $S(k)$.

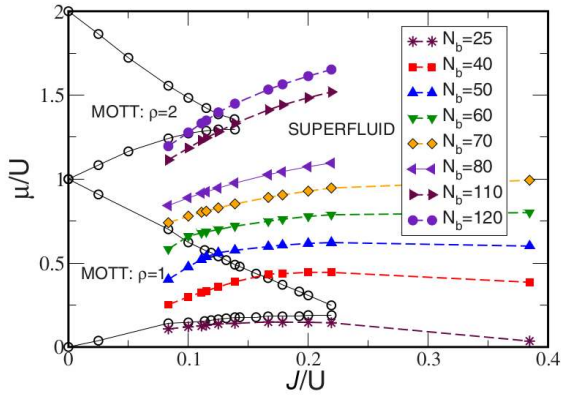

Figure 2.4: Canonical flows (i.e. lines with constant number of particles) in the homogeneous phase diagram for the 1D system with $V_T(i) = 0.008\ i^2$. Figure adapted from Ref. [52].

trapping energy is larger) only after U/J increases of a certain finite amount. In the range $U/J = 6.3 - 6.8$, also other quantities do not vary much (the total trapping energy, the interaction energy, the chemical potential).

In the simulation described in the second part of Ref. [50], also the Mott region with two particles per site can form. Up to a certain value of U/J ($U/J \sim 13$) the visibility has features similar to the previous case (see Fig. 2.3(c)), while for larger values of U/J there are more kinks; these correspond to features in N_c (number of particle in the 20 central sites). These kinks do not result from the formation of new Mott domains, but rather from a redistribution of bosons between the two existing Mott regions $n = 2$ and $n = 1$. Such a redistribution happens discontinuously, leading to the features in $\mathcal{V}$. Moreover, the competition between the trapping potential and the repulsive interaction is such that the size of the superfluid shoulders with $1 < n < 2$ is not always monotonously decreasing with U/J, and this can lead to an increase in $\mathcal{V}$ (e.g. the kink at $U/t = 14.6$).

Also a purely one-dimensional effect takes place, for larger values of U/J. When the Mott with $n = 2$ melts (i.e. there is a superfluid in the center of the trap), correlations develop between the two disconnected superfluid shoulders with $1 < n < 2$, and $\mathcal{V}$ increases. This would not happen in higher dimensionalities, since the superfluid region surrounding the center would be a shell (or a ring, in 2D), and it would be already connected.

In Ref. [52], some of the same authors of Ref. [50] give more details to explain the behaviour of the visibility. In particular, they map the canonical trajectories (i.e. the lines with fixed number of particles) on the homogeneous phase diagram (as shown in Fig. 2.4) and they use this to interpret the results for the visibility.

Following for instance the trajectory with $N = 50$ in Fig. 2.4 and com-

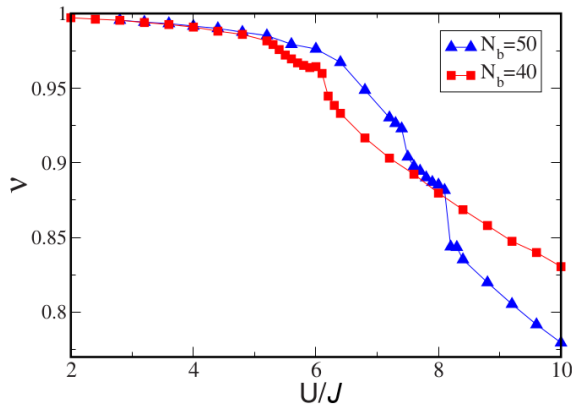

Figure 2.5: Visibility in the 1D trapped system with $V_T(i) = 0.008\ i^2$, for 40 (squares) and 50 (triangles) particles. Figure adapted from Ref. [52].

paring it with the corresponding visibility (Fig. 2.5), it is clear that the second kink in the visibility $\mathcal{V}$ happens when the chemical potential in the center of the trap (i.e. μ, and not the effective local chemical potential $\tilde{\mu}_i$) enters a Mott lobe. This corresponds to the closing of a Mott region in the center of the trap. On the other side, the position of the first kink in the visibility is not directly read from the phase diagram. One would expect its appearance for the first value of J/U lower than the tip of the Mott lobe ($J/U < (J/U)_c$); however this happens for a smaller J/U. This means that the first kink does not correspond to the first appearance of the Mott regions, but rather to the value of U/J for which these regions gain a relevant size.

2.4 Other QMC studies

The QMC studies described in the previous section are limited to one dimension, thus they cannot achieve a quantitative agreement with results of experiments in 3D (Ref. [31]). In this section we review other QMC studies, more relevant for the direct comparison with experiments.

QMC in 2D

Ref. [53] is a QMC study in 1D and 2D, in which isentropical lines are followed, rather than lines at constant temperatures. The reason for this is that what is constant during an experiment is the entropy, rather than the temperature. The aim of this work is the study of the change of temperature during an experiment, also with the goal of verifying the typical assumptions about the adiabaticity of the lattice loading procedure.

The authors show the results (reported in Fig. 2.6) of a calculation

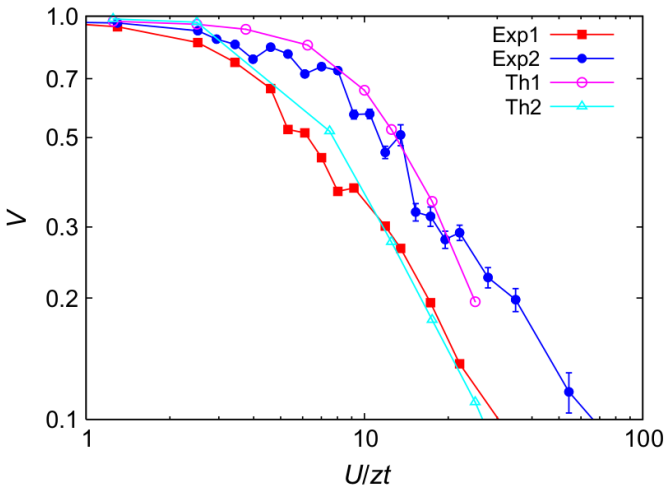

Figure 2.6: Visibility (in a semi-logarithmic scale) for a 2D system computed by QMC (lines "Th1" and "Th2", parameters in Ref. [53]) and experimental results from Ref. [31] with 79×10^3 (red squares) and 224×10^3 (blue circles) particles. Figure extracted from Ref. [53].

of the visibility for a 2D system. The choice of the parameters is such to reproduce the density profile of the 3D experiments in Ref. [31], but the simulation does not make use of a realistic number of particles and system size. However the trapping potential is chosen to be realistic, according to the relations given in section 1.5. Note that for the theoretical results shown in Fig. 2.6 also experimental effects have been taken into account, as the integration over a finite area in momentum space around $\mathbf{k}_{\max}$ and $\mathbf{k}_{\min}$.

There is a quantitative agreement (Fig. 2.6) between theoretical and experimental curves for the visibility, but the resolution in the one derived through QMC simulations is not enough to make any statement about the kinks in $\mathcal{V}$.

Moreover, the authors state that

- the visibility is in agreement with the gas being in the quantum regime, without any transition to the normal phase;
- the loading of the lattice is slow enough to make this process adiabatic, i.e. the real ground state of the system is reached.

QMC in 3D

In Ref. [45], another quantitative description of the experimental visibility of Ref. [31] is given. In particular, after taking into account all the different experimental effects (as the averaging over a certain area in momentum space and the regime of finite time-of-flight) the authors achieve a quantitative

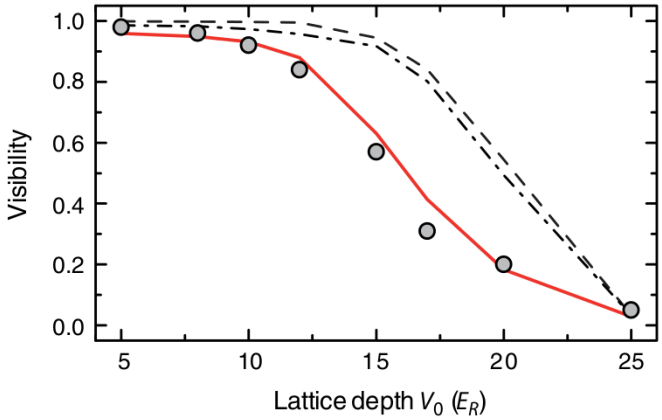

Figure 2.7: The two upper lines are calculations for finite (dashed line) and infinite (dotted-dashed line) time of flight, without considering experimental resolution. The visibility for a 3D system (including the corrections for finite experimental resolution) are shown, as computed by QMC (solid line) and in experiments (Ref. [31], circles). Figure extracted from Ref. [45].

agreement of the experimental visibility with the curve obtained by QMC simulations in 3D. This is shown in Fig. 2.7.

To conclude, in Ref. [53] and Ref. [45], a quantitative description of the experimental visibility results from Ref. [31] is achieved; however, no kinks are observed in $\mathcal{V}$. This could also be a by-product of the low resolution on the U/J axis, in Figures 2.6 and 2.7.

2.5 Kinks in the triangular lattice

In Ref. [28] a different experimental set-up is presented, in which the optical lattice is a triangular one in two dimensions. This geometry is achieved by a different positioning of the laser beams and it is an example of the possibility of describing different models with cold atoms in optical lattices.

In Fig. 2.8, the visibility is shown for this system. Some kinks in $\mathcal{V}$ are present, similar to the ones described in section 2.2. Unexpectedly, the positions of these kinks are in close agreement with the positions of the mean-field values of the critical coupling U/J (described in section 3.2).

Note that the number of nearest neighbours of a site in a triangular lattice is $z = 6$; this leads to a better agreement (as compared with the square lattice, where $z = 4$) of the mean-field results with the exact ones.

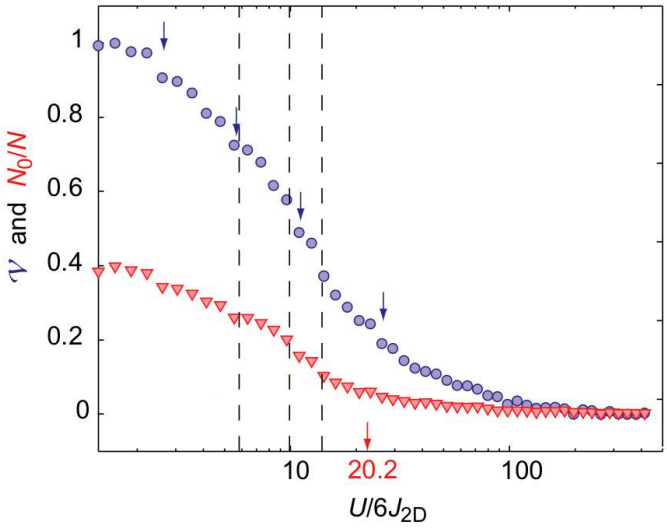

Figure 2.8: Visibility (blue circles) and condensate fraction (red triangles) as a function of $U/(6J)$, in a semi-logarithmic scale. The visibility is normalized through its maximum value $\mathcal{V}_{\max} = 0.48$. $z = 6$ is the number of nearest neighbours in a 2D triangular lattice. Figure adapted from Ref. [45].

Chapter 3

Numerical techniques

Since when fermionic Hubbard model and its bosonic equivalent were introduced, they have been often used as prototypical models to develop and test new analytical and numerical solution techniques in the physics of condensed-matter and many-body systems. For the bosonic model, this effort increased after its relation with cold-atomic systems was clarified, and it has been some times inspired from the study of the equivalent model for fermions.

In this chapter, we describe a few of the numerical schemes that can be used to find the ground-state of the bosonic model and characterize it by evaluating correlation functions. As we mention at the end of this introduction, the list of techniques that have been developed is very large. We concentrate on the ones that we have used in this thesis, namely the site-decoupled mean-field approach and the quantum Monte Carlo one.

In section 3.1 we describe the basic way of solving exactly any Hamiltonian, and we explain why this approach cannot be used for large systems, that is linked to the exponentially growing dimension of the Hilbert space. A first solution of this problem is the decoupling of some terms in the Hamiltonian, to reduce the complexity of the problem. The Bogoliubov approach described in section 3.2.1 is based on the decoupling of the interaction term, but it does not describe correctly the Mott phase transition. On the contrary, the site-decoupled mean-field scheme described in section 3.2.2 is based on the decoupling of the hopping term and succeeds in giving a description of the phase transition, although an approximate one. This method was first proposed in Ref. [54] to study the homogeneous model and only recently it has been applied to the inhomogeneous one (Ref. [55]). It can be shown that this approach is analogous to the use of the Gutzwiller variational wave function, that was first introduced to study the fermionic Hubbard model and then adapted to the bosonic case (Refs [56, 3]). In section 3.2.3 we describe this ansatz and show its relation with the mean-field approach. To conclude the description of the site-decoupled mean-field approach, in sec-

tion 3.2.4 we explain some details on how to implement the it numerically and in section 3.3 we compare its results with some known ones. In Section 3.4 we describe two QMC approaches: the variational Monte Carlo (VMC) scheme and the Green's Function Monte Carlo (GFMC) scheme. The results of the latter do not depend on initial assumptions about the ground-state and are in principle unbiased (for bosonic problems).

In general, the numerical techniques applied to study the Bose-Hubbard model (and the analogous models with a trapping potential, long-range interactions, disorder, or finite temperature) have included a large set of approaches. As a partial list, we mention some works based on the main techniques

- Gutzwiller wave function and corresponding mean-field theory (for homogeneous and trapped systems), Refs [56, 54, 57, 58, 59, 60, 61, 55];
- cluster mean-field theory, Refs [62, 63, 64];
- a large set of different QMC schemes (including VMC, GFMC, Path Integral Monte Carlo, Strong Series Expansion), Refs [65, 66, 50, 37, 67, 52, 36, 68, 53, 49, 69, 14, 11];
- DMRG (introduced in Ref. [16]), Refs [34, 70, 71, 8, 9, 72, 10];
- Matrix Product States, Ref. [12];
- Dynamical Mean Field Theory for bosons, Refs [73, 74, 75];
- exact diagonalization schemes, Refs [76, 3, 77].

3.1 Exact diagonalization

In this section we describe an exact diagonalization (ED) scheme to obtain the full spectrum and eigenstates of the Hamiltonian. We stress that another ED scheme exists (the one based on the Lanczos algorithm, not described here), that targets only the lowest eigenvalues and the corresponding eigenstates of the Hamiltonian. Since this method requires less CPU time and memory, it allows to study larger systems and it would be the most appropriate choice for a study only based on ED. We do not consider it here because we will use ED only as a benchmark for other methods.

The general procedure for diagonalizing the full Hamiltonian is the following

- choose a basis $\{|\phi_j\rangle\}_{j=1,..,D}$ of the Hilbert space of the system and list its D states;
- construct the $D \times D$ matrix representation of the Hamiltonian in the chosen basis, according to $H_{i,j} = \langle\phi_i|H|\phi_j\rangle$;

- diagonalize the matrix $H_{i,j}$, in order to get the full set of eigenvalues and eigenvectors $\{E_j, \vec{v}_j\}_{j=1,..,D}$.

At the end of this procedure, the lowest eigenvalue is identified with the ground state energy and the corresponding eigenvector is the ground state wave function in the basis $\{|\phi_j\rangle\}_{j=1,..,D}$

$$E_{gs} = \min_j(E_j), \tag{3.1}$$

$$H\vec{v}_{gs} = E_{gs}\vec{v}_{gs}. \tag{3.2}$$

and any observable expressed as an expectation value on the ground state $|\psi_0\rangle$ can be computed as

$$\langle\psi_0|\hat{A}|\psi_0\rangle = \sum_{j=1}^{D} |v_{gs}^j|^2 \langle\phi_j|\hat{A}|\phi_j\rangle. \tag{3.3}$$

In the case of a system of N bosons on a lattice of L sites, we choose the occupation numbers basis

$$|x\rangle = |n_1, n_2, ..., n_L\rangle \equiv |n_1\rangle_1 \otimes |n_2\rangle_2 \otimes .. \otimes |n_L\rangle_L. \tag{3.4}$$

The number D of terms in the basis (i.e. the dimension of the Hilbert space) grows as

$$D = \binom{N+L-1}{L-1} = \frac{(N+L-1)!}{N!(L-1)!}. \tag{3.5}$$

As an example, in Table 3.1 we show the number of states at unit filling ($N = L$) for some system sizes:

N	D	N	D
4	35	10	92378
6	462	20	68923264410
8	6435	30	59132290782430712

Table 3.1: Number of states for a system of N indistinguishable bosons in N sites.

This makes it clear that the full ED approach can only work for small systems.

Notice that in the matrix representation of H many entries are zero (all the ones corresponding to two different states not connected through a hopping process). Nevertheless, also the Lanczos algorithm will face the problem of the exponential growth of D, making the study of large system impossible. For this reason, we will not use ED to study the physical properties of the system in the thermodynamic limit ($N, L \to \infty$, $N/L = const$), but only as a benchmark for other methods. Notice that ED finds applications also as a part of more complex methods, like Numerical Renormalization Group and Dynamical Mean Field Theory.

3.2 Mean-field approaches

We present here some mean-field approaches for the homogeneous and inhomogeneous Bose-Hubbard models introduced in Eqs (1.7) and (1.28). The first approach that we describe is the Bogoliubov approximation (for the homogeneous system), that is based on the decoupling of the interaction term; this technique is not able to correctly describe the Mott phase transition. In section 3.2.2 we describe another mean-field scheme, based on the decoupling of the hopping term in the Hamiltonian. This approach succeeds in predicting the Mott phase transition, although in an approximate way. It has been shown later that using this mean-field approach corresponds to a variational calculation based Gutzwiller ansatz. This link is described in section 3.2.3 and it explains why this approach is more suitable (as compared to ED) to study large systems. More concretely, in sections 3.2.4 and 3.3 we describe the numerical scheme we used and we validate it by comparison with known results in the literature.

3.2.1 Bogoliubov approximation

The Bogoliubov transformation is a general method that allows to diagonalize some Hamiltonians, the most common example being in the context of the BCS theory of superconductivity. In this section (mainly based on Ref. [57]), we consider the homogeneous Bose-Hubbard model on a d-dimensional hypercubic lattice with spacing a. By introducing the operators $\hat{c}^\dagger_{\mathbf{k}}$ and $\hat{c}_{\mathbf{k}}$ through

$$\hat{b}_i = \frac{1}{\sqrt{N_s}} \sum_{\mathbf{k}} \hat{c}_{\mathbf{k}} e^{-i\mathbf{k}\cdot\mathbf{x}_i} \tag{3.6}$$

(where N_s is the total number of sites), the Hamiltonian can be written in momentum space as

$$H = \sum_{\mathbf{k}} (-\overline{\epsilon_{\mathbf{k}}} - \mu) \hat{c}^\dagger_{\mathbf{k}} \hat{c}_{\mathbf{k}} + \frac{1}{2} \frac{U}{N_s} \sum_{\mathbf{k},\mathbf{k}'} \sum_{\mathbf{k}'',\mathbf{k}'''} \hat{c}^\dagger_{\mathbf{k}} \hat{c}^\dagger_{\mathbf{k}'} \hat{c}_{\mathbf{k}''} \hat{c}_{\mathbf{k}'''} \delta_{\mathbf{k}+\mathbf{k}'} \delta_{\mathbf{k}''+\mathbf{k}'''}, \tag{3.7}$$

where $\overline{\epsilon_{\mathbf{k}}} = 2J \sum_{j=1}^{d} \cos(k_j a)$ is the dispersion related to the kinetic term. We note here that for $U = 0$ this Hamiltonian is diagonal and its ground-state is the one with N bosons in the $\mathbf{k} = 0$ minimum of $\overline{\epsilon_{\mathbf{k}}}$:

$$\left(\hat{c}^\dagger_{\mathbf{k}=0}\right)^N |0\rangle, \tag{3.8}$$

corresponding to the ideal superfluid state introduced in Eq. (1.31).

Assuming that the number of condensate atoms $N_0 = \langle \hat{c}^\dagger_0 \hat{c}_0 \rangle$ is much larger than unity (assumption valid in the weakly interacting limit) and choosing the expectation values of $\hat{c}^\dagger_0$ and $\hat{c}_0$ to be real, the Bogoliubov

approach consists in replacing these operators with their average plus a fluctuation (that we call with the same names)

$$\begin{aligned} \hat{c}_0 &\to \sqrt{N_0} + \hat{c}_0, \\ \hat{c}_0^\dagger &\to \sqrt{N_0} + \hat{c}_0^\dagger. \end{aligned} \tag{3.9}$$

Substituting Eq. (3.9) into Eq. (3.7) and setting to zero the part of the Hamiltonian that is linear in the fluctuation terms $\hat{c}_0^\dagger$ and $\hat{c}_0$, we find the condition

$$\mu = UN_0/N_s - zJ \tag{3.10}$$

(in which $z = 2d$ is the number of nearest neighbours of a site) and the following effective Hamiltonian

$$\begin{aligned} H^{\text{eff}} = &-\frac{1}{2}Un_0N_0 - \frac{1}{2}\sum_{\mathbf{k}}(\epsilon_{\mathbf{k}} + Un_0) + \\ &+ \frac{1}{2}\sum_{\mathbf{k}}(\hat{c}_{\mathbf{k}}^\dagger, \hat{c}_{-\mathbf{k}}) \begin{bmatrix} \epsilon_{\mathbf{k}} + Un_0 & Un_0 \\ Un_0 & \epsilon_{\mathbf{k}} + Un_0 \end{bmatrix} \begin{pmatrix} \hat{c}_{\mathbf{k}} \\ \hat{c}_{-\mathbf{k}}^\dagger \end{pmatrix}, \end{aligned} \tag{3.11}$$

in which we have introduced $\epsilon_{\mathbf{k}} = zJ - \overline{\epsilon_{\mathbf{k}}}$ and $n_0 = N_0/N_s$ and we have kept only terms up to second order in the fluctuations. This Hamiltonian is diagonalized by means of the substitution

$$\begin{pmatrix} \hat{d}_{\mathbf{k}} \\ \hat{d}_{-\mathbf{k}}^\dagger \end{pmatrix} = \begin{bmatrix} u_{\mathbf{k}} & v_{\mathbf{k}} \\ v_{\mathbf{k}}^* & u_{\mathbf{k}}^* \end{bmatrix} \begin{pmatrix} \hat{c}_{\mathbf{k}} \\ \hat{c}_{-\mathbf{k}}^\dagger \end{pmatrix}, \tag{3.12}$$

in which the condition $|u_{\mathbf{k}}|^2 - |v_{\mathbf{k}}|^2 = 1$ is required so that the new operators $\hat{d}_{\mathbf{k}}^\dagger$ and $\hat{d}_{\mathbf{k}}$ satisfy the bosonic commutation relations. This leads to the diagonal Hamiltonian

$$H^{\text{eff}} = -\frac{1}{2}Un_0N_0 + \frac{1}{2}\sum_{\mathbf{k}}[\hbar\omega_{\mathbf{k}} - (\epsilon_{\mathbf{k}} + Un_0)] + \sum_{\mathbf{k}} \hbar\omega_{\mathbf{k}} \hat{d}_{\mathbf{k}}^\dagger \hat{d}_{\mathbf{k}}, \tag{3.13}$$

with the dispersion relation

$$\hbar\omega_{\mathbf{k}} = \sqrt{\epsilon_{\mathbf{k}}^2 + 2Un_0\epsilon_{\mathbf{k}}}, \tag{3.14}$$

and the following values of the coefficients

$$|v_{\mathbf{k}}|^2 = |u_{\mathbf{k}}|^2 - 1 = \frac{1}{2}\left(\frac{\epsilon_{\mathbf{k}} + Un_0}{\hbar\omega_{\mathbf{k}}} - 1\right). \tag{3.15}$$

For this effective Hamiltonian, the total density is given by the sum of the condensate density n_0 and the density due to the excitations

$$\begin{aligned} n &= \frac{1}{N_s}\sum_{\mathbf{k}}\langle \hat{c}^\dagger_{\mathbf{k}}\hat{c}_{\mathbf{k}}\rangle_{\text{eff}} = \\ &= n_0 + \frac{1}{N_s}\sum_{\mathbf{k}\neq 0}\left[(|u_{\mathbf{k}}|^2+|v_{\mathbf{k}}|^2)\langle \hat{d}^\dagger_{\mathbf{k}}\hat{d}_{\mathbf{k}}\rangle_{\text{eff}} + |v_{\mathbf{k}}|^2\right] = \\ &= n_0 + \frac{1}{N_s}\sum_{\mathbf{k}\neq 0}\left[(|u_{\mathbf{k}}|^2+|v_{\mathbf{k}}|^2)\frac{1}{e^{\beta\hbar\omega_{\mathbf{k}}}-1} + |v_{\mathbf{k}}|^2\right], \end{aligned} \tag{3.16}$$

where $\langle..\rangle_{\text{eff}}$ denote the expectation value calculated with the effective Hamiltonian H^{eff}. In the limit of zero temperature the first term in the summand vanishes and the following relation can be obtained in the continuum limit

$$n = n_0 + \frac{1}{2}\int_{-1/2}^{+1/2} d\mathbf{q}\left(\frac{\epsilon_{\mathbf{q}}+Un_0}{\hbar\omega_{\mathbf{q}}}-1\right), \tag{3.17}$$

with $\epsilon_{\mathbf{q}} = \sum_{j=1}^{d}[1-\cos(2\pi q_j)]$ and $\hbar\omega_{\mathbf{q}} = (\epsilon^2_{\mathbf{q}} + 2Un_0\epsilon_{\mathbf{q}})^{1/2}$.

Eq. (3.17) has been used in Ref. [57] to compute the condensate fraction n_0/n for different filling factors n and for different values of U/J. Numerical results for integer and non-integer filling factor do not show relevant differences and in both cases there is no critical value of U/J above which the condensate fraction vanishes. This is a sign of the fact that Bogoliubov approximation does not predict the phase transition to the Mott insulator phase, the reason being that the approximated treatment of interactions cannot be used when describing a strongly depleted condensate. Nevertheless, this approach turns out useful in the regime of weak interactions, where it is mostly effective to compute observables that are defined in momentum space.

3.2.2 Site-decoupled mean-field approach

In this section we describe a mean-field approach based on the decoupling of the hopping part of the Hamiltonian, introduced by K. Sheshadri and collaborators in 1993 (Ref. [54]). Considering the inhomogeneous Bose-Hubbard Hamiltonian (Eq. 1.7), we use the following decoupling

$$\hat{b}^\dagger_i\hat{b}_j = \langle\hat{b}^\dagger_i\rangle\hat{b}_j + \hat{b}^\dagger_i\langle\hat{b}_j\rangle - \langle\hat{b}^\dagger_i\rangle\langle\hat{b}_j\rangle = \psi_i\hat{b}_j + \psi_j\hat{b}^\dagger_i - \psi_i\psi_j, \tag{3.18}$$

where we have introduced the real order parameter $\psi_i \equiv \langle\hat{b}_i\rangle$. Note that the choice of $\psi_i \in \mathbb{R}$ is arbitrary, but it is justified by the fact that the phase of ψ_i does not enter explicitly in the procedure for finding the ground-state.

By using Eq. (3.18), the Hamiltonian becomes a sum of local terms

$$\hat{H} = \sum_i \hat{H}_i^{\mathrm{MF}}(\psi_i, \{\psi_j\}_{\mathrm{nn}_i}), \tag{3.19}$$

where the local mean-field Hamiltonian $\hat{H}_i^{\mathrm{MF}}$ on the site i depends on the other sites only through the order parameters ψ_j on the sites j that are nearest neighbours of i (i.e. $j \in \mathrm{nn}_i$). The explicit expression is

$$\hat{H}_i^{\mathrm{MF}} = J\left(\sum_{j\in\mathrm{nn}_i}\psi_j\right)\left(\psi_i - \hat{b}_i^\dagger - \hat{b}_i\right) + \left(\frac{U}{2}\hat{n}_i(\hat{n}_i-1) + (\epsilon_i - \mu)\hat{n}_i\right). \tag{3.20}$$

We will now describe the difference between the homogeneous ($\epsilon_i = 0$) and inhomogeneous ($\epsilon_i \neq 0$) cases. In the homogeneous case, the observables are not site-dependent and in particular $\psi_i = \psi$. Therefore the local Hamiltonians are completely decoupled and equivalent, and each one of them reads

$$\hat{H}^{\mathrm{MF}}(\psi) = Jz\psi\left(\psi - \hat{b}^\dagger - \hat{b}\right) + \left[\frac{U}{2}\hat{n}(\hat{n}-1) - \mu\hat{n}\right]. \tag{3.21}$$

This can be expressed as a tridiagonal matrix in the occupation number basis $\{|n\rangle\}$:

$$\langle p|\hat{H}^{\mathrm{MF}}|q\rangle = \left[zJ|\psi|^2 - q\mu + \frac{U}{2}q(q-1)\right]\delta_{q,p} - zJ\psi\sqrt{p}\delta_{q,p-1} - zJ\psi\sqrt{q}\delta_{p,q-1}. \tag{3.22}$$

A maximum number $n_{\max}$ of bosons per site has to be chosen; as an example, the matrix representation with $n_{\max} = 4$ is:

$$\begin{bmatrix} zJ|\psi|^2 & -zJ\psi & 0 & 0 & 0 \\ -zJ\psi & zJ|\psi|^2 - \mu & -\sqrt{2}zJ\psi & 0 & 0 \\ 0 & -\sqrt{2}zJ\psi & zJ|\psi|^2 - 2\mu + U & -\sqrt{3}zJ\psi & 0 \\ 0 & 0 & -\sqrt{3}zJ\psi & zJ|\psi|^2 - 3\mu + 3U & -2zJ\psi \\ 0 & 0 & 0 & -2zJ\psi & zJ|\psi|^2 - 4\mu + 6U \end{bmatrix}. \tag{3.23}$$

In the inhomogeneous case (not treated in Ref. [54], but recently described in Ref. [55]) the order parameter depends on the site index, and therefore also the matrix in Eq. (3.23) does. Hence, the local Hamiltonians $H_i^{\mathrm{MF}}(\psi_i, \{\psi_j\}_{\mathrm{nn}_i})$ are no longer decoupled (because the hopping term depends on the values of the order parameter in the neighbouring sites) and all of them have to be diagonalized simultaneously. In section 3.2.4 we describe a self-consistent approach that allows us to do so.

3.2.3 Gutzwiller ansatz

The Gutzwiller wave function is a variational ansatz that was first introduced to study the fermionic Hubbard model. It has then been applied also in

the context of the bosonic model (Refs [78, 56]), in which it has also been modified to a different version, that is the one we are presenting here. The variational ansatz is the following product of independent states on every site

$$|\psi_g\rangle = \prod_{i=1}^{N_s} \left[\sum_{n_i=0}^{\infty} f_{n_i}^{(i)} |n_i\rangle \right], \tag{3.24}$$

where the coefficients $f_{n_i}^{(i)}$ are to be optimized in the variational procedure. This choice of the wave function restricts the dimensionality D of the Hilbert space to

$$D = N_s \times (n_{\max} + 1), \tag{3.25}$$

where $n_{\max}$ is the already mentioned maximum on-site occupation number. This quantity (D) increases only linearly with the system size (to be compared with the exponential growth in Eq. 3.5), thus making it possible to study larger system, as compared to the ones that can be studied by ED methods. The drawback is that the Gutzwiller wave function includes no correlations between different sites; this approximation is particularly poor in the description of the Mott state, since the state at finite J is replaced with the ideal state (correct only for $J/U \equiv 0$). This problem will be the reason for a lack of agreement with QMC results in some specific cases (see section 3.3).

Using this ansatz, the following expectation values can be computed in terms of the coefficients $\left\{ f_{n_i}^{(i)} \right\}$:

$$\rho_{ij} \equiv \langle \hat{b}_i^\dagger \hat{b}_j \rangle_g = \left(\sum_{n_i=0}^{\infty} f_{n_i+1}^{(i)*} f_{n_i}^{(i)} \sqrt{n_i + 1} \right) \left(\sum_{n_j=0}^{\infty} f_{n_j}^{(j)*} f_{n_j+1}^{(j)} \sqrt{n_j + 1} \right), \tag{3.26}$$

$$\langle \hat{b}_i^\dagger \hat{b}_i \rangle_g = \sum_{n_i=0}^{\infty} \left| f_{n_i}^{(i)} \right|^2 n_i, \tag{3.27}$$

$$\langle \hat{b}_i^\dagger \hat{b}_i^\dagger \hat{b}_i \hat{b}_i \rangle_g = \sum_{n_i=0}^{\infty} \left| f_{n_i}^{(i)} \right|^2 n_i (n_i - 1), \tag{3.28}$$

$$\langle \hat{b}_i \rangle_g = \sum_{n_i=0}^{\infty} f_{n_i}^{(i)*} f_{n_i+1}^{(i)} \sqrt{n_i + 1}. \tag{3.29}$$

From these results, we can compute the expectation value of the Bose-

Hubbard Hamiltonian (Eq. 1.7) on the state $|\psi_g\rangle$:

$$\langle H\rangle_g = -J\sum_{\langle i,j\rangle}\left(\sum_{n_i=0}^{\infty} f_{n_i+1}^{(i)*} f_{n_i}^{(i)}\sqrt{n_i+1}\right)\left(\sum_{n_j=0}^{\infty} f_{n_j}^{(j)*} f_{n_j+1}^{(j)}\sqrt{n_j+1}\right) + \\ + \frac{U}{2}\sum_{i=1}^{N_s}\sum_{n_i=0}^{\infty}\left|f_{n_i}^{(i)}\right|^2 n_i(n_i-1) + \sum_{i=1}^{N_s}(\epsilon_i-\mu)\sum_{n_i=0}^{\infty}\left|f_{n_i}^{(i)}\right|^2 n_i. \tag{3.30}$$

As we did for the site-decoupled mean-field approach, we stress the difference in the application of this scheme to the homogeneous or inhomogeneous Hamiltonian. In the homogeneous case ($\epsilon_i = 0$), the coefficients f_n are not function of the site index; thus Eq. (3.30) becomes

$$\frac{\langle H\rangle_g}{N_s} = \left[-zJ\sum_{n=1}^{\infty}\sum_{m=1}^{\infty} f_n^* f_{n-1} f_{m-1}^* f_m\sqrt{nm} + \sum_{n=0}^{\infty}|f_n|^2\left(\frac{U}{2}n(n-1)-\mu n\right)\right]. \tag{3.31}$$

In order to describe the ground state of the system, the coefficients in the Gutzwiller state have to be the ones that minimize this expectation value. This is a function of $(n_{\max}+1)$ variables; for typical values of $n_{\max}$, the minimization can easily be performed numerically. Once the f_n coefficients are known, observables can be computed through Eqs (3.26)-(3.29) and analogous expressions.

In principle the same approach can be used also in the inhomogeneous case, but it has to be applied to the full Hamiltonian (Eq. 3.30); thus the minimization involves $(n_{\max}+1)\times N_s$ variables, while in the homogeneous case these are only $(n_{\max}+1)$. As an example, the number of variables for a $5\times5\times5$ lattice with a cut-off $n_{\max}=4$ is 5 in the homogeneous case and 625 in the inhomogeneous one. Note that the symmetries of the trapping potential can be used to reduce this number in the inhomogeneous case. For instance, we have typically restricted our calculations to the sites (i,j,k) with $i,j,k\geq 0$, making use of the symmetry of $V_T(\mathbf{x})$ under rotations to describe the rest of the lattice.

Link with the mean-field approach

When the total Hamiltonian of the system is written as a sum of local terms as in Eq. (3.19), the Gutzwiller ansatz (Eq. 3.24) is the most general form of the eigenstates. Hence, the coefficients $\vec{f^i} = \{f_n^{(i)}\}$ correspond to the eigenvectors of the mean-field local Hamiltonian matrix (Eq. 3.22) and the site-decoupled mean-field approach is equivalent to the minimization based on the Gutzwiller ansatz. Therefore the two methods (the diagonalization of the mean-field Hamiltonian and the minimization of the Gutzwiller energy) are equivalent. We choose to use the diagonalization of the mean-field

Hamiltonian in order to avoid the task of minimizing functions of many variables, and we use the Gutzwiller coefficients to compute expectation values.

3.2.4 Numerical scheme

In this section we explain more in detail the possible schemes to use the mean-field/Gutzwiller approach that we have described.

Homogeneous case

The study of the homogeneous system does not involve large calculations, for the reasons explained before. In any case different schemes can be used:

1. one choice is that of considering the Hamiltonian in Eq. (3.22), finding its $(n_{\max}+1)$ eigenvalues $E_\alpha(\psi)$ analytically and minimizing the lowest one w.r.t. the order parameter ψ. This corresponds to finding

$$\min_{\psi} \min_{\alpha\in\{0,..,n_{\max}\}} E_\alpha(\psi). \tag{3.32}$$

2. a second possible choice is that of using a self-consistent loop. The Hamiltonian H^{MF} is diagonalized for a certain value of ψ, after which a new value ψ_{new} of the order parameter is computed by Eq. (3.29). If the two quantities are not equal (up to a certain numerical tolerance), ψ is conveniently changed and the procedure is repeated till convergence.

Inhomogeneous case

Also in the inhomogeneous case the same two schemes (conveniently generalized from a single site to the full lattice) can be used. Both methods can be applied when the chemical potential μ is fixed (i.e. only the Gutzwiller coefficients $\{\vec{f^i}\}$ are unknown) or when the number of particles is fixed (i.e. also the chemical potential is unknown).

We begin by considering the case of fixed chemical potential. The minimization procedure is performed in the following way

- diagonalize the local Hamiltonian in the truncated basis on each site (this is a $(n_{\max}+1)\times(n_{\max}+1)$ matrix that is real, symmetric and tridiagonal);
- identify the lowest eigenvalue $E_g(\{\psi_i\})$ of the total Hamiltonian (sum of all the local ones);
- minimize E_g with respect to $\{\psi_i\}$;
- compute local observables through the Gutzwiller coefficients $\{\vec{f^i}\}$.

The self-consistent loop approach is the following

- initialize the set of values of the order parameter on the entire lattice $\{\psi_i\}_{\text{old}}$;
- diagonalize the local Hamiltonian in the truncated basis on each site;
- compute the new order parameters $\{\psi_i\}_{\text{new}}$, through the Gutzwiller coefficients (Eq. 3.29);
- compare $\{\psi_i\}_{\text{old}}$ and $\{\psi_i\}_{\text{new}}$ by evaluating the norm of their difference in $\mathbb{R}^{N_s}$
  - if they differ more than a certain chosen tolerance, update the order parameters with the new values and repeat the diagonalization;
  - if they are close enough, keep the new values of the order parameters and Gutzwiller coefficients and use them to compute observables.

The scheme to work at a fixed number of particles (valid for both methods) is the following

- initialize the chemical potential μ;
- perform either the minimization or the self-consistent loop;
- compute the number of particles $\tilde{N}$ through the Gutzwiller coefficients (Eq. 3.27);
- compare N and $\tilde{N}$: if they differ less than a certain tolerance then the calculation stops, otherwise μ has to be modified and the previous two steps have to be repeated until convergence.

In particular, we use the secant method to decide how to modify μ in order to make $|\tilde{N} - N|$ decrease and vanish.

As we discussed before, in the inhomogeneous case the minimization involves a large number of variables. For this reason, we have used the minimization approach only in the homogeneous case, to validate the results of the self-consistent approach. In section 3.3.1 we report a comparison of the two methods for the homogeneous system, while for the inhomogeneous case we have only used the self-consistent approach.

3.3 Validation of the mean-field scheme

In this section we show the results of some calculations used to test and validate the mean-field approach. In particular, in section 3.3.1 we compare the two methods described in section 3.2.4; in section 3.3.1 we study the visibility of the homogeneous system and compare the results with the ones

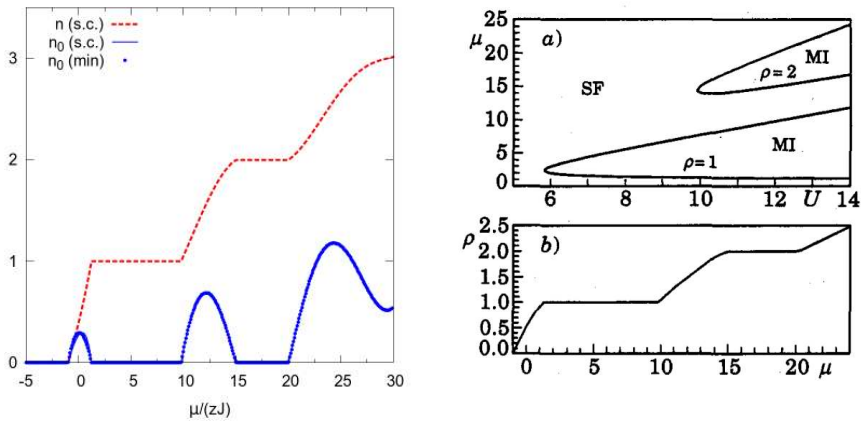

Figure 3.1: Left: Mean-field calculation of the density n and the condensate density $n_0 \equiv |\psi|^2$ as functions of the chemical potential μ, for a fixed value of $U = 12zJ$ and with $n_{\max} = 5$. The results for n_0 are obtained through the self-consistent loop scheme (solid line) and through the minimization scheme (points); the difference between the two is hardly visible. Right: (a) phase diagram and (b) density along the line with $U = 12$ (energies expressed in units of zJ). Figure extracted from Ref. [54].

from Ref. [79]; in section 3.3.2 we show that our results are in qualitative agreement with mean-field calculation from Refs [58, 59], which compare well with QMC results from Ref. [65].

3.3.1 Homogeneous system

Self-consistent loop vs minimization

In section 3.2.4 we described two methods to find the ground state of the mean-field Hamiltonian, namely a minimization w.r.t. the order parameter ψ and the scheme based on the self-consistent loop. In Fig. 3.1 we show the results for the density n and condensate density n_0 as functions of the chemical potential; we set $U = 12zJ$, in order to compare the results with those in Ref. [54]. As expected, we observe the presence of the Mott phase characterized by integer filling, incompressibility (vanishing derivative of $n = n(\mu)$) and vanishing condensate density. The condensate density is computed with the two methods described in 3.2.4 and the difference between the results is hardly visible in the plot. The density as a function of μ is in agreement with results in Ref. [54], also shown in Fig. 3.1.

Calculations of visibility

In this section we compare results obtained in different ways for the visibility of a 3D homogeneous Bose-Hubbard model, in a region of the phase diagram

close to the tip or the Mott lobe with filling one. This point is

$$\begin{aligned}\left(\frac{U}{zJ}\right)_c &\simeq 5.83,\\ \left(\frac{\mu}{zJ}\right)_c &\simeq 0.4\left(\frac{U}{zJ}\right)_c = 2.33,\end{aligned} \tag{3.33}$$

as given in Refs [80, 57].

Our goal is to compare the visibility of the interference pattern computed in two different ways:

- the standard definition introduced in section 2.1 (see Refs [65, 45]), that remains valid also in the inhomogeneous case;
- the expression (specific for the homogeneous case) derived in Ref. [79].

In both approaches, the finiteness of the system has an effect on $n(\mathbf{k})$ and then on the visibility; for this reason we have repeated the calculations for different lattice sizes and compared the results.

Here we repeat some of the steps used in Ref. [79] to derive an expression for the visibility. From the mean-field decoupling (Eq. 3.18), we have that

$$\langle \hat{b}_i^\dagger \hat{b}_j \rangle = \begin{cases} |\psi|^2 & {\scriptstyle (i\neq j)} \\ n & {\scriptstyle (i=j)} \end{cases}, \tag{3.34}$$

and this leads to the following rewriting of $S(\mathbf{k})$ (defined in Eq. 1.38):

$$\begin{aligned} S(\mathbf{k}) &= \sum_i n + \sum_i e^{i\mathbf{k}\cdot\mathbf{r}_i} \sum_{j\neq i} e^{-i\mathbf{k}\cdot\mathbf{r}_j} |\psi^2| = N + |\psi^2| \sum_i e^{i\mathbf{k}\cdot\mathbf{r}_i} \left(-e^{-i\mathbf{k}\cdot\mathbf{r}_i} + \sum_j e^{-i\mathbf{k}\cdot\mathbf{r}_j} \right) = \\ &= N + |\psi^2| \sum_i e^{i\mathbf{k}\cdot\mathbf{r}_i} \sum_j e^{-i\mathbf{k}\cdot\mathbf{r}_j} - |\psi|^2 \sum_i 1 = (N - N_0) + |\psi|^2 \left| \sum_i e^{i\mathbf{k}\cdot\mathbf{r}_i} \right|^2 \equiv \\ &\equiv (N - N_0) + |\psi|^2 f(\mathbf{k}), \end{aligned} \tag{3.35}$$

where N (N_0) is the number of particles (condensed particles). We have introduced

$$f(\mathbf{k}) = \left| \sum_i e^{i\mathbf{k}\cdot\mathbf{r}_i} \right|^2 = \prod_{j=1}^{3} \left| \sum_{j=1}^{L} e^{ik_j ja} \right|^2 = \prod_{j=1}^{3} F(k_j), \tag{3.36}$$

where a is the lattice spacing; for cubic $L \times L \times L$ lattice, $F(k)$ reads

$$F(k) = \left(\frac{\sin(kLa/2)}{\sin(ka/2)} \right)^2, \tag{3.37}$$

and it satisfies:

$$\begin{aligned} &F(0) = L^2, \\ &F(2\pi/a) = L^2, \\ &F(\sqrt{2}\pi/(2a)) \ll L^2. \end{aligned} \tag{3.38}$$

We now make use of the Gaussian form of the Wannier functions (approximation introduced in section 1.2), in which σ is the characteristic spread of the Gaussian in momentum space. Thus the visibility defined in Eq. (2.1) can be rewritten as

$$\begin{aligned} \mathcal{V} &= \frac{n_\perp(2\pi/a,0) - n_\perp(2\pi/(\sqrt{2}a), 2\pi/(\sqrt{2}a))}{n_\perp(2\pi/a,0) + n_\perp(2\pi/(\sqrt{2}a), 2\pi/(\sqrt{2}a))} = \\ &= \frac{|\psi|^2 \left[F(0)F\left(\frac{2\pi}{a}\right) - F\left(\frac{\sqrt{2}\pi}{2a}\right) F\left(\frac{\sqrt{2}\pi}{2a}\right)\right] \int dq_z F(q_z)|w(q_z)|^2}{2(N-N_0) + |\psi|^2 \left[F(0)F\left(\frac{2\pi}{a}\right) + F\left(\frac{\sqrt{2}\pi}{2a}\right) F\left(\frac{\sqrt{2}\pi}{2d}\right)\right] \int dq_z F(q_z)|w(q_z)|^2} \simeq \\ &\simeq \frac{|\psi|^2 L^4 \int dq_z F(q_z)|w(q_z)|^2}{2(N-N_0) + |\psi|^2 L^4 \int dq_z F(q_z)|w(q_z)|^2} = \frac{|\psi|^2}{|\psi|^2 + (N-N_0)y}, \end{aligned} \tag{3.39}$$

where y is introduced as

$$y = \frac{2}{L^4} \frac{1}{\int dq_z |w(q_z)|^2 F(q_z)} \tag{3.40}$$

and it is approximated as

$$y \approx \frac{\sigma a}{L^5 \sqrt{\pi}}. \tag{3.41}$$

In Fig. 3.2, we show the visibility computed by the standard definition and by Eq. (3.39), for different lattice sizes. There is a good agreement between the different results, that are both based on the same mean-field decoupling. Note that Eq. (3.39) includes an approximation for y (Eq. 3.41).

We stress that the size of the system does not play any role in determining the ground-state (i.e. the Gutzwiller coefficients), but it matters in the computation of the Fourier transforms required in the momentum distribution. In the thermodynamic limit, the peaks in the momentum distribution would be very sharp (δ-like) in the superfluid phase, while in the Mott phase $n(\mathbf{k})$ would be completely flat. Therefore the visibility would have a sharp transition between $\mathcal{V} = 1$ (superfluid phase) and $\mathcal{V} = 0$ (Mott phase). As shown in Fig. 3.2, results obtained with both approaches change in the correct way for increasing system size.

3.3.2 Inhomogeneous system

In Refs [58, 59, 60], the results of mean-field calculations in the 3D trapped case are shown and compared with the same results computed by QMC (Ref. [65]). The quantities that are computed include the density profiles

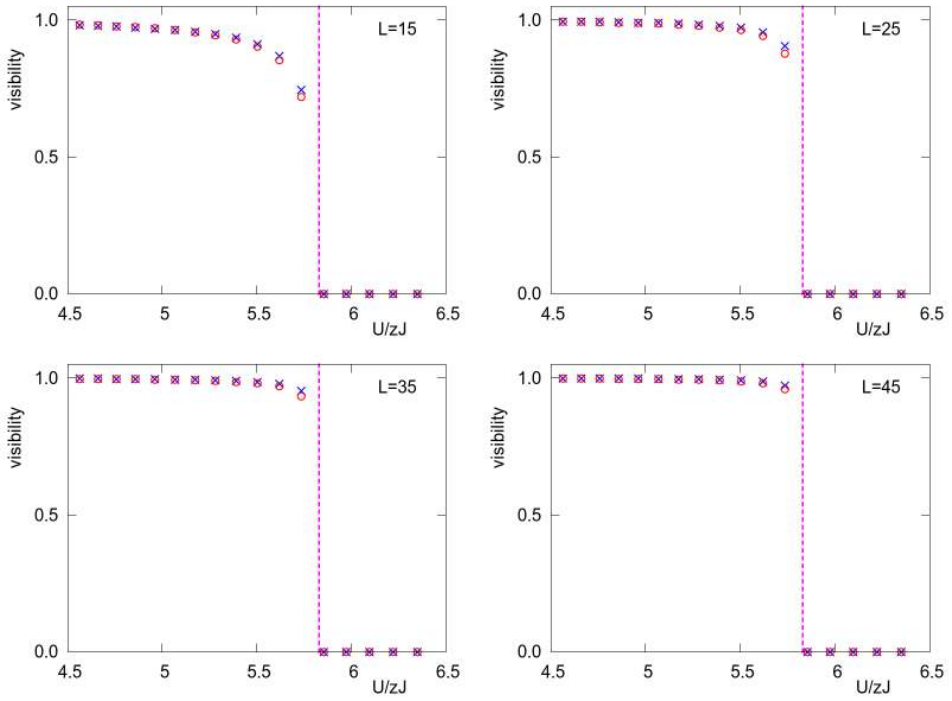

Figure 3.2: Visibility of a $L \times L \times L$ homogeneous system computed using the standard definition in Eq. (2.1) (crosses) and the expression in Eq. (3.39) from Ref. [79] (open circles). The expected mean-field critical value of U/zJ is also shown (dashed line).

and the momentum distribution $S(\mathbf{k})$ (Eq. 1.38) for six different sets of parameters. In this section we show the agreement of our calculation with the other mean-field ones and we comment about the comparison with the QMC results.

In Fig. 3.3, we show the agreement of density profiles computed by a mean-field approach and by QMC. This does not directly lead to an agreement in the results for $S(\mathbf{k})$, as shown in Fig. 3.4. In particular, for the choice (d) of the parameters, the QMC and mean-field $S(\mathbf{k})$ are qualitatively different. This is because in this situation there is almost no superfluid fraction in the accurate (i.e. QMC) results; therefore the order parameter ψ_i is zero on most of the lattice sites and this makes the mean-field decoupling a poor approximation in this case. Apart from this case, the mean-field results for $S(\mathbf{k})$ are quite accurate.

Moreover, we show the following comparisons of our results with mean-field ones from the literature:

- in Figures 3.5 and 3.6 we show the results of our scheme for the density profiles and momentum distributions, in good agreement with the

other mean-field results (Figures 3.3 and 3.4);
- in Fig. 3.7 we compare our results with those in Ref. [58];
- in Fig. 3.8 we compare our results for the integrated momentum distribution $S_\perp(k_x, k_y)$ (Eq. 1.41) with the ones from Ref. [60].

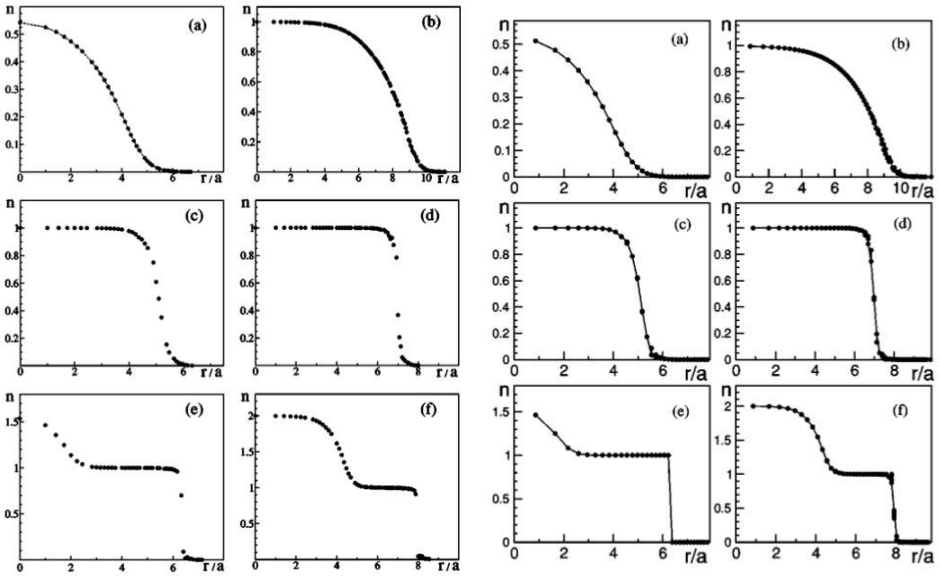

Figure 3.3: Left: density profiles computed by QMC, figure from Ref. [65]. Right: density profiles computed by the mean-field approach, figure from Ref. [59]. The sets of parameters are the same as in Fig. 3.5 .

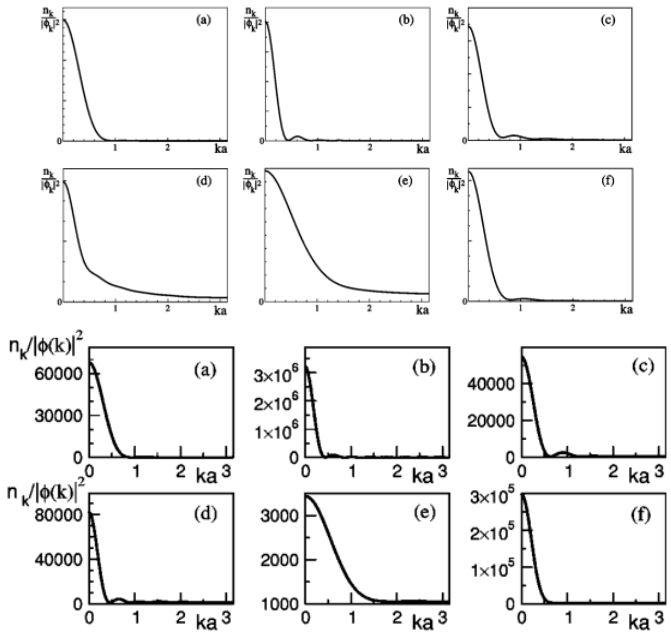

Figure 3.4: Top: momentum distribution $S(\mathbf{k})$ computed by QMC, figure from Ref. [65]. Bottom: momentum distribution $S(\mathbf{k})$ computed by the mean-field approach, figure from Ref. [59]. The sets of parameters are the same as in Fig. 3.5 .

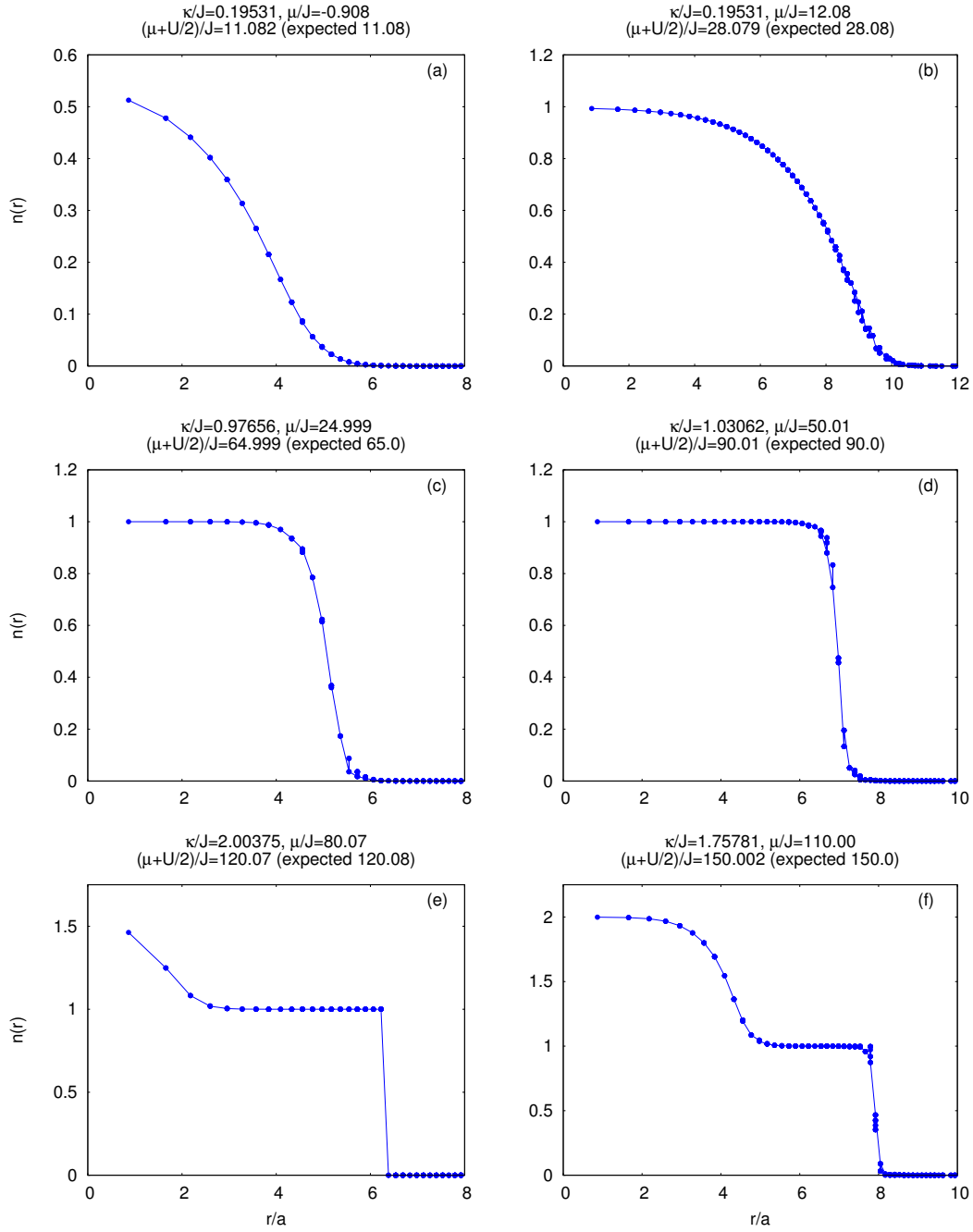

Figure 3.5: Density profiles for a 3D trapped system. The choice of the parameters corresponds to the one in the six plots in Fig. 1 in Ref. [65]; the values of $(\mu + U/2)$ are slightly different from the ones in that work, as shown in the titles of the plots; κ is the curvature of the harmonic trap.

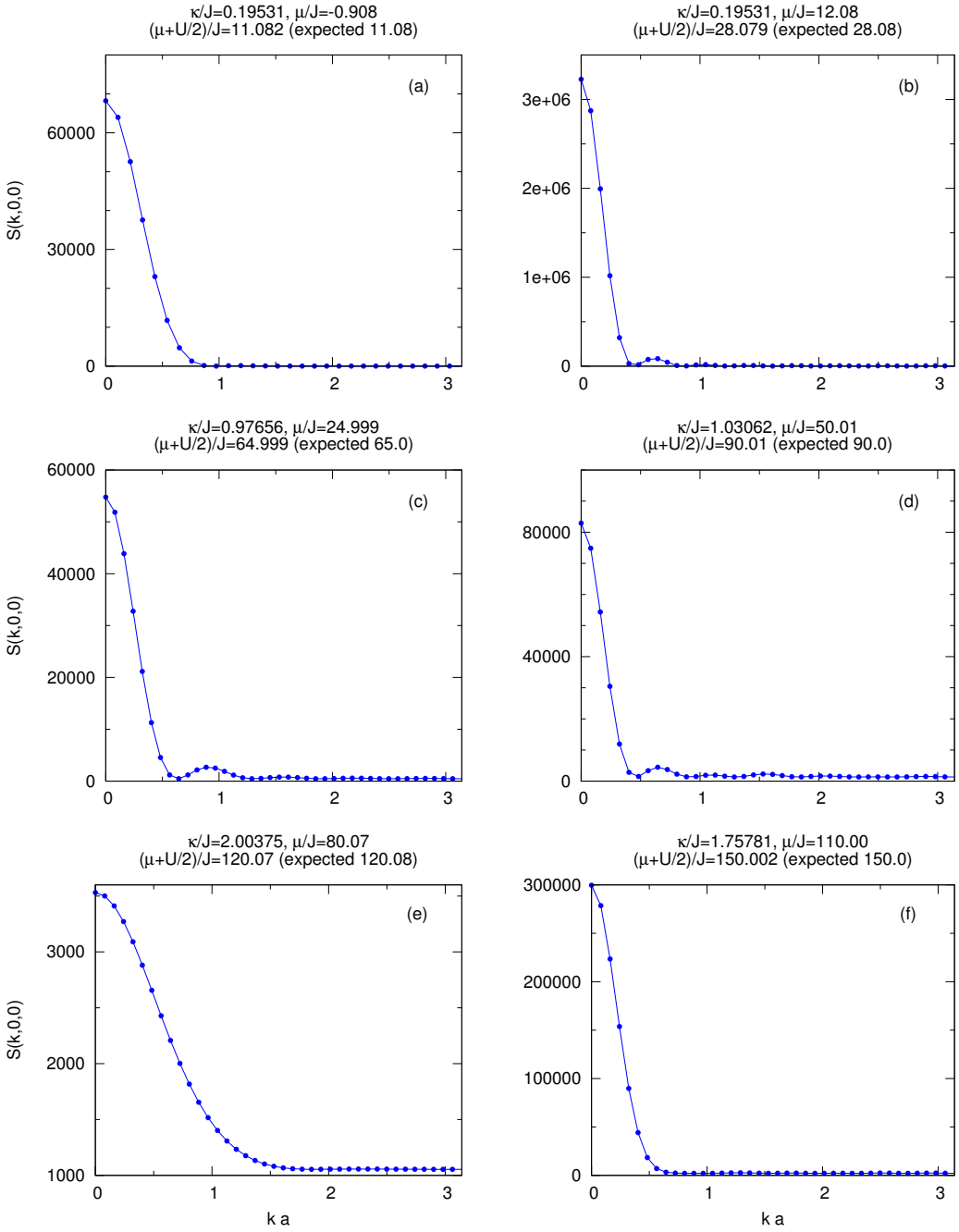

Figure 3.6: $S(\mathbf{k})$ along a cut $\mathbf{k} = (k, 0, 0)$ for a 3D trapped system. The parameters correspond to the ones in Fig. 3.5.

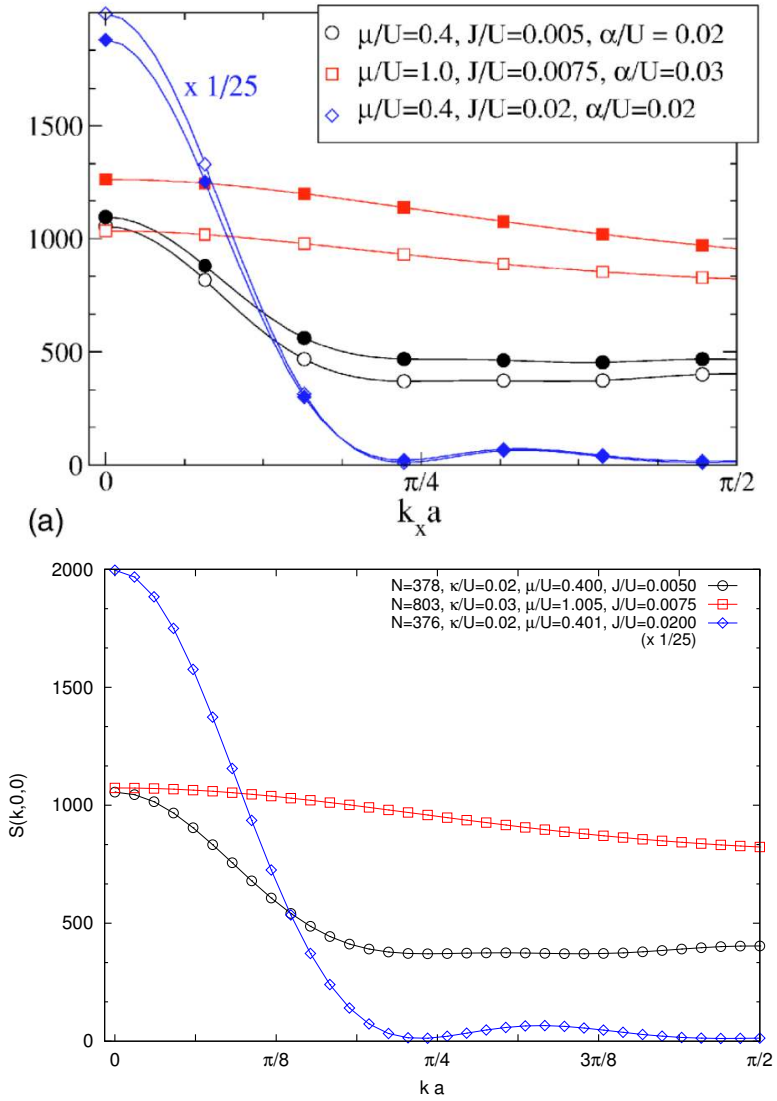

Figure 3.7: $S(\mathbf{k})$ along a cut $\mathbf{k} = (k, 0, 0)$ for a 3D trapped system. Top: figure from [58] (empty symbols are results from mean-field, full ones include perturbative corrections). Bottom: results from the present work ($\alpha \equiv \kappa$ is the curvature of the harmonic trap).

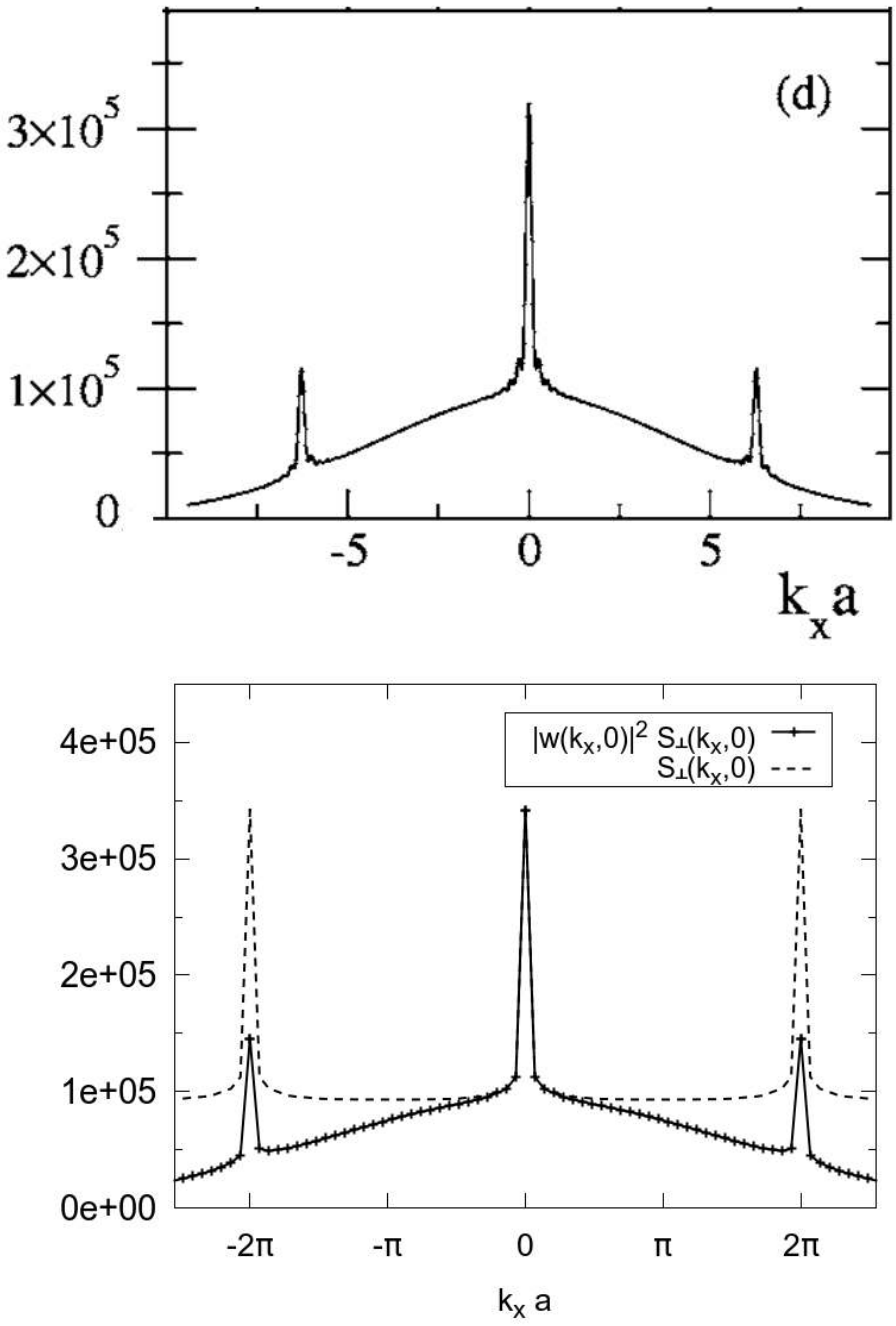

Figure 3.8: Top: integrated momentum distribution $n_\perp(k_x, k_y)$ along a cut $\mathbf{k}_\perp = (k, 0)$; figure adapted from Ref. [60]. Bottom: results from the present work ($59 \times 59 \times 59$ lattice, lattice depth $V_0/E_R = 22$, trap curvature $\kappa = 0.00131$ and number of particles $N = 94172$), with or without the Gaussian Wannier envelope.

3.4 Quantum Monte Carlo

As we mentioned in section 3.1, the exponential growth of the Hilbert space dimension D with the system size makes the computation of the exact ground state wave function impossible for a large system; but even knowing this wave function (and being able to store it on a computer) would not be enough, because computing any physical observable would require a summation of D terms. We will describe here two Monte Carlo schemes that provide a way of dealing with this task.

The VMC approach is based on a certain choice of a trial wave function, including a set of variational coefficients that have to be optimized to minimize the expectation value of the Hamiltonian. This method depends heavily on the choice of the trial wave function, but despite giving only approximate results it can provide some physical information about the system. Moreover it is often needed as a starting point for more accurate methods. The GFMC scheme is a stochastic implementation of the power method, in which a projector operator is applied repeatedly to an initial wave function to filter out the high energy components and find the ground state. This method is in principle exact, up to the statistical error.

3.4.1 Variational Monte Carlo

The VMC method is based on a certain choice of a trial wave function $|\psi_\alpha\rangle$, depending on a set of parameters $\{\alpha\}$ and expressed in terms of a certain basis $\{|x\rangle\}$. A VMC scheme includes the following operations

- computing the expectation value of the energy for a certain choice of the coefficients α;
- optimizing the coefficients in order to minimize this expectation value, thus obtaining the best estimate of the ground state energy and wave function;
- computing the relevant observables on this state.

Considering the wave function $|\psi\rangle$ (for a fixed set of parameters), the expectation value of the Hamiltonian can be written as

$$E[\psi] = \frac{\langle\psi|\hat{H}|\psi\rangle}{\langle\psi|\psi\rangle} = \frac{\sum_x e_L(x)\psi^2(x)}{\sum_x \psi^2(x)} = \sum_x e_L(x)p_x, \tag{3.42}$$

by introducing the local energy

$$e_L(x) = \frac{\langle x|\hat{H}|\psi\rangle}{\langle x|\psi\rangle} \tag{3.43}$$

and the (normalized, non-negative) probability distribution

$$p_x = \frac{\psi^2(x)}{\sum_y \psi^2(y)}. \tag{3.44}$$

Therefore, computing the energy in a state corresponds to taking the average of the local energy $e_L(x)$, weighted with the probability distribution p_x. If we can construct a sequence of configurations $\{|x_n\rangle\}$ distributed according to the probability p_x, then the expectation value of the local energy can be computed as

$$E[\psi] = \lim_{N\to\infty} \left(\frac{1}{N} \sum_{n=1}^{N} e_L(x_n) \right). \tag{3.45}$$

One way of sampling the sequence of states $\{|x_n\rangle\}$ in such a way that the states are distributed according to the probability $p(x)$ is the one based on the Metropolis algorithm (Ref. [81]), in which a move from an initial state $|x_i\rangle$ to a final state $|x_f\rangle$ is proposed with a rate

$$T(x_i \to x_f) = T(x_f \to x_i), \tag{3.46}$$

and accepted with probability

$$A(x_i \to x_f) = \min\left(1, \frac{p(x_f)}{p(x_i)}\right) = \min\left(1, \left|\frac{\langle x_f|\psi\rangle}{\langle x_i|\psi\rangle}\right|^2\right). \tag{3.47}$$

This scheme satisfies the "detailed balance" condition

$$p(x_i)T(x_i \to x_f)A(x_i \to x_f) = p(x_f)T(x_f \to x_i)A(x_f \to x_i). \tag{3.48}$$

With this procedure, it is possible to use Eq. (3.45) to compute $E[\psi_\alpha]$ for any choice of the coefficients $\{\alpha\}$ of the trial wave function $|\psi_\alpha\rangle$.

The next step consists in finding the optimal set of α's, for which $E[\psi_\alpha]$ is minimum. We will now describe an example of the simplest case, in which the wave function depends only on one coefficient (g) and the optimal state can be estimated by directly comparing the energies for different values of g. More efficient optimization schemes have to be used for variational wave functions depending on a larger number of parameters.

Example

Here we give an example of the explicit calculation of the terms in the local energy in a simple case. We consider the homogeneous Bose-Hubbard for a fixed number N of bosons

$$\hat{H} = -\frac{J}{2} \sum_{i=1}^{L} \left(\hat{b}_i^\dagger \hat{b}_{i+1} + \hat{b}_{i+1}^\dagger \hat{b}_i \right) + \frac{U}{2} \sum_{i=1}^{L} \hat{n}_i(\hat{n}_i - 1), \tag{3.49}$$

and we consider a trial wave function that depends on a single variational parameter g:

$$|\psi_g\rangle = e^{-g\sum_i \hat{n}_i^2}|\phi_0\rangle, \tag{3.50}$$

where

$$|\phi_0\rangle \propto \left(\sum_i \hat{b}_i^\dagger\right)^N |0\rangle. \tag{3.51}$$

With $g = 0$, this wave function is the exact solution for the model with $U = 0$ (as discussed in section 1.4); we expect that the optimal value of g (i.e. the one minimizing the energy for a certain choice of J and U) will increase with U, since configurations with many bosons on the same site have a larger cost in interaction energy.[1]

Given a configuration $|x\rangle$, the local energy is written as

$$e_L(x) = \sum_{x'}\langle x|\hat{H}|x'\rangle\frac{\langle x'|\psi\rangle}{\langle x|\psi\rangle} = \langle x|\hat{H}|x\rangle + \sum_{x'\neq x}\langle x|\hat{H}|x'\rangle\frac{\langle x'|\psi\rangle}{\langle x|\psi\rangle}, \tag{3.52}$$

in which the only non-zero terms in the summation over $|x'\rangle$ are the ones such that

$$|x'\rangle = |n_1'...n_L'\rangle, \tag{3.53}$$
$$\langle x'|x'\rangle = 1, \tag{3.54}$$
$$n_j' = n_j + \delta_{jq} - \delta_{jp} \tag{3.55}$$
$$\langle x|\hat{H}|x'\rangle = -\frac{J}{2}\sqrt{n_q+1}\sqrt{n_p}, \tag{3.56}$$

while for all the other choices of $|x'\rangle$ the matrix element $\langle x|H|x'\rangle$ is zero. Through some algebra, we find that the local energy reads

$$\begin{aligned} e_L(x) =& \frac{U}{2}\sum_{i=1}^{L} n_i(n_i-1) + \\ &- \frac{J}{2}e^{-2g}\sum_{p=1}^{L} n_p e^{2gn_p}\left(e^{-2gn_{p+1}} + e^{-2gn_{p-1}}\right), \end{aligned} \tag{3.57}$$

and the ratio $p(x')/p(x)$ (to be used in the Metropolis acceptance probability) reads

$$\begin{aligned} \left|\frac{\langle x'|\psi_g\rangle}{\langle x|\psi_g\rangle}\right|^2 &= \left|e^{-2g(n_q+1-n_p)}\frac{\langle x'|\phi_0\rangle}{\langle x|\phi_0\rangle}\right|^2 = \\ &= \left|e^{-2g(n_q+1-n_p)}\sqrt{\frac{n_p}{n_q+1}}\right|^2 = \\ &= e^{-4g(n_q+1-n_p)}\frac{n_p}{n_q+1}. \end{aligned} \tag{3.58}$$

[1] This ansatz is analogous to the Gutzwiller wave function typically used to study the fermionic Hubbard model, in which for large U the double occupancies $N_D = \sum_i n_{i,\uparrow}n_{i,\downarrow}$ are suppressed by a term λ^{N_D} (with $\lambda \in [0,1]$).

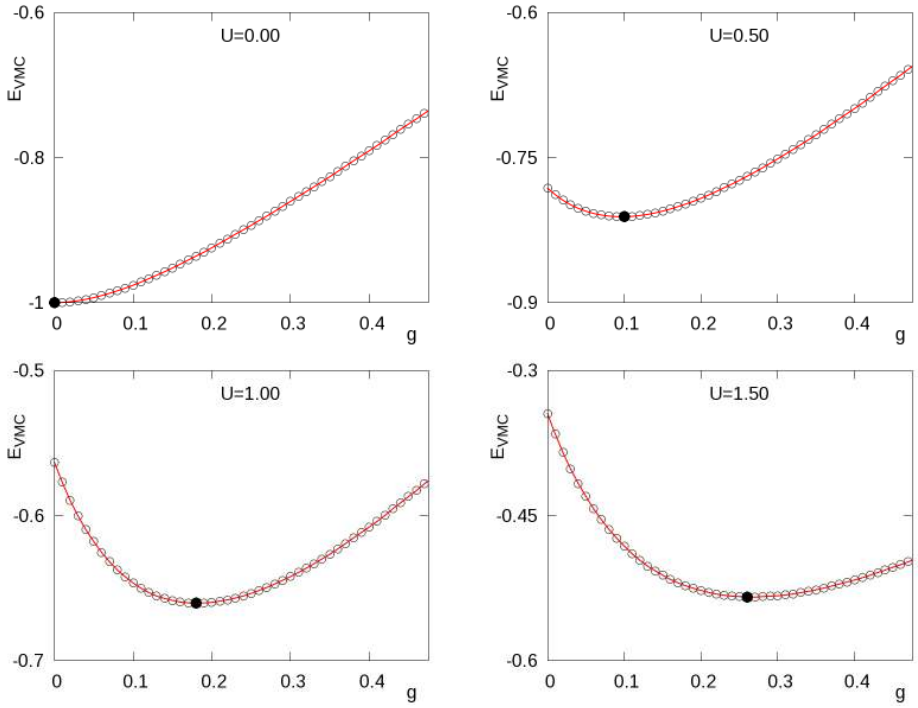

Figure 3.9: Variational energy for a system of 8 bosons on 8 sites, as a function of the coefficient g. J is set equal to 1, U is different in the four plots. The optimal energy is marked with a full circle. The statistical errors are smaller than the symbols.

Eqs. (3.57) and (3.58) are the basis for a VMC approach. In this case we use a trivial optimization scheme, i.e. we compute the energy for different choices of the variational parameter g in a mesh. Results for different values of U are shown in Fig. 3.9, from which it can be noticed that the optimal value of g is larger when the on-site repulsive interaction is stronger. This is an example of a situation in which a physical information (i.e. the fact that for larger U the multiple occupancies are suppressed) is already clear from a variational approach, while in a more sophisticated (and accurate) approach this might not be directly available.

Remarks

In the previous example we have used a trivial optimization scheme to find the optimal g; more efficient schemes have to be used for variational wave functions depending on a larger number of parameters. In particular the VMC calculation on which the results in chapter 5 are based makes use of the stochastic optimization algorithm introduced in Ref. [82].

We stress that the applicability of a VMC approach of this kind to the

model of interest is based on the fact that (a) for each state $|x\rangle$ there is a limited number (of the order of the number of sites) of non-zero matrix elements $\langle x|H|x'\rangle$ and (b) there is an efficient way of computing these matrix elements.

A general feature of VMC is the so called *zero variance* property, i.e. in case the chosen trial wave function is an eigenstate of the Hamiltonian then the fluctuations of the local energy are identically zero ($e_L(x)$ does not depend on $|x\rangle$). This is specially useful when some analytical results are known, in order to validate the QMC approach.

3.4.2 Green's Function Monte Carlo

The GFMC technique is a stochastic implementation of the power method, in which a projector operator is applied repeatedly to an initial wave function to filter out the high energy components and find the ground state. In this section we first introduce the power method and then describe the simpler version of GFMC (the single walker formulation). A more detailed explanation can be found in Ref. [83].

Power method

Given an initial state $|\psi_0\rangle$ that is not orthogonal to the ground state (i.e. such that $\langle\psi_0|\psi_{GS}\rangle \neq 0$), we show how to construct a sequence of states converging to $|\psi_{GS}\rangle$. We define this sequence as

$$\langle x|\psi_{n+1}\rangle = \sum_{x'} \left(\Lambda\delta_{x,x'} - \langle x|\hat{H}|x'\rangle\right) \langle x'|\psi_n\rangle, \tag{3.59}$$

where Λ is a positive number. Considering a basis of eigenstates $|\phi_i\rangle$ of the Hamiltonian

$$\hat{H}|\phi_i\rangle = E_i|\phi_i\rangle, \tag{3.60}$$

we rewrite the initial state of the sequence as

$$|\psi_0\rangle = \sum_i |\phi_i\rangle\langle\phi_i|\psi_0\rangle. \tag{3.61}$$

For the first iteration in the sequence we have

$$\begin{aligned}
\langle x|\psi_1\rangle &= \sum_i \sum_{x'} \left(\Lambda\delta_{x,x'} - \langle x|\hat{H}|x'\rangle\right) \langle x'|\phi_i\rangle\langle\phi_i|\psi_0\rangle = \\
&= \sum_i \left(\Lambda\langle x|\phi_i\rangle - \langle x|\hat{H}|\phi_i\rangle\right) \langle\phi_i|\psi_0\rangle = \\
&= \sum_i \langle\phi_i|\psi_0\rangle(\Lambda - E_i)\langle x|\phi_i\rangle,
\end{aligned} \tag{3.62}$$

and the n-th state reads

$$|\psi_n\rangle = \sum_i \langle\phi_i|\psi_0\rangle(\Lambda - E_i)^n|\phi_i\rangle. \tag{3.63}$$

If Λ is large enough, we have that

$$|\Lambda - E_{GS}| = \max_i |\Lambda - E_i|\,, \tag{3.64}$$

and all the components of ψ_n not corresponding to the ground state are exponentially suppressed for large n. Thus we have proved that the sequence converges to the ground state: $|\psi_n\rangle \to |\psi_{GS}\rangle$.

We stress that this method does not include any approximation, but it cannot be applied in practice because the number of basis states $|x\rangle$ of which one has to keep track grows exponentially when new states are generated by using Eq. (3.63).

Single walker GFMC

The goal of this technique is to reproduce the power method in a stochastic way, in which we do not need to keep track of an exponentially increasing number of states; this is achieved by performing the n-th step of a power method

$$\langle x|\psi_n\rangle = \langle x|(\Lambda - \hat{H})^n|\psi_0\rangle \tag{3.65}$$

in a stochastic way. The basic element of this approach is the so called *walker*, that is determined by a state $|x\rangle$ and a weight $w \geq 0$. Given an initial walker configuration (x_0, w_0), we introduce a rule to generate (x_{n+1}, w_{n+1}) in terms of (x_n, w_n); this defines a Markov chain with elements distributed with a probability $P_n(x_n, w_n)$. In order to use this chain to evaluate $\psi_n(x)$, we require that

$$\int dw\, w\, P_n(x, w) = \langle x|\psi_n\rangle, \tag{3.66}$$

so that for $n \to \infty$ we have a way of getting to the ground state, even though we are only interested in computing expectation values and not in $\langle x|\psi_{GS}\rangle$ itself.

In order to construct the correct Markov chain, we introduce the Green's function

$$G_{x',x} = \Lambda\delta_{x',x} - \langle x'|\hat{H}|x\rangle \tag{3.67}$$

and we have to assume that $G_{x',x} \geq 0$ so that it can be interpreted as a probability. For the diagonal terms $G_{x,x}$, we can choose Λ large enough to satisfy this requirement, but the off-diagonal terms $G_{x',x}$ only depend on the Hamiltonian. If the requirement of $G_{x',x} \geq 0$ is not satisfied, the Hamiltonian has the so called *sign problem* (typically present for fermionic

Hamiltonians or in frustrated lattices) and the approach described here cannot be directly used. Once we assume that there is no sign-problem, we can split G in the following way

$$\begin{aligned} b_x &= \sum_{x'} G_{x',x}, \\ p_{x',x} &= \frac{G_{x',x}}{b_x}, \\ G_{x',x} &= p_{x',x} b_x, \end{aligned} \tag{3.68}$$

so that $p_{x',x}$ is a stochastic matrix (i.e. $p_{x',x} \geq 0$ and $\sum_{x'} p_{x',x} = 1$). This decomposition of $G_{x',x}$ allows us to construct the Markov chain by defining the following rules for generating (x_{n+1}, w_{n+1}) from (x_n, w_n)

- generate x_{n+1} with probability p_{x_{n+1},x_n},
- multiply the old weight by b_{x_n} to obtain the new one: $w_{n+1} = w_n b_{x_n}$.

It can be proven that the resulting Markov chain satisfies Eq. (3.66).

Importance sampling

The present GFMC scheme does not satisfy the *zero variance* property, that in turn is satisfied by the VMC scheme described in section 3.4.1. This property corresponds to the fact that if the variational wave function is an exact eigenstate of the Hamiltonian then the local energy $e_L(x)$ is a constant (not depending on $|x\rangle$) and it has no statistical fluctuations. In order to recover this property in the GFMC scheme, we consider the *importance sampling* Green's function

$$\bar{G}_{x',x} = G_{x',x} \frac{\psi_g(x')}{\psi_g(x)}, \tag{3.69}$$

where the so called *guiding function* ψ_g is a guess of the ground state wave function, obtained before using the GFMC (for instance this can be the outcome of a VMC calculation). The same decomposition of Eq. (3.68) can be applied to $\bar{G}$

$$\begin{aligned} \bar{G}_{x',x} &= p_{x',x} b_x, \\ p_{x',x} &= \frac{\bar{G}_{x',x}}{b_x}, \\ b_x &= \sum_{x'} \bar{G}_{x',x} = \Lambda - \frac{\sum_{x'} \psi_g(x') H_{x',x}}{\psi_g(x)} = \Lambda - e_L(x), \end{aligned} \tag{3.70}$$

and the Markov chain can be defined in the same way. With these definitions, if the guiding function is the correct ground state wave function ($\psi_g(x) = \psi_{GS}(x)$) we have that the local energy $e_L(x)$ is a constant and statistical fluctuations vanish. Thus we have recovered the zero variance property.

Observables

The ground state energy is obtained as the large n limit of the weighted average of the local energies, i.e.

$$E_{GS} = \lim_{n\to\infty} \frac{\langle w_n e_L(x_n)\rangle}{\langle w_n\rangle} = \lim_{n\to\infty} \frac{\langle\psi_g|\hat{H}(\Lambda-\hat{H})^n|\bar{\phi}\rangle}{\langle\psi_g|(\Lambda-\hat{H})^n|\bar{\phi}\rangle}, \tag{3.71}$$

where $|\bar{\phi}\rangle$ is defined as the state such that $\langle x|\bar{\phi}\rangle \equiv b_x\psi_g(x)$.

In practice, it is enough to stop the iteration at a finite number of iterations $n = \tilde{n}$. In order to have a statistically relevant expectation value, one could generate many Markov chains of $\tilde{n}$ steps and consider their average. However, it is more convenient to generate a single Markov chain of M steps (with $M \gg \tilde{n}$) and use the expression

$$E_{GS} = \lim_{n\to\infty} \frac{\langle\psi_g|\hat{H}(\Lambda-\hat{H})^n|\bar{\phi}\rangle}{\langle\psi_g|(\Lambda-\hat{H})^n|\bar{\phi}\rangle} = \frac{\sum_{n=n_0}^{M} G_{n,\tilde{n}} e_L(x_n)}{\sum_{n=n_0}^{M} G_{n,\tilde{n}}}, \tag{3.72}$$

where n_0 is the number of steps required to get to the equilibrium and the coefficients $G_{n,\tilde{n}}$ are defined as

$$G_{n,\tilde{n}} = \prod_{i=1}^{\tilde{n}} b_{x_{n-i}}. \tag{3.73}$$

In Fig. 3.10 the result of such a calculation for the Hamiltonian in Eq. (1.42) is compared with the exact value, to show the convergence in terms of $\tilde{n}$.

We now consider other observables; if they are diagonal in the occupation number basis, the analogue of the local energy is just the corresponding eigenvalue

$$\frac{\langle\psi_g|\hat{A}|x\rangle}{\langle\psi_g|x\rangle} = A_x. \tag{3.74}$$

It can be verified that the analogue of Eq. (3.71) is

$$\frac{\langle w_n A_{x_{n-m}}\rangle}{\langle w_n\rangle} = \frac{\langle\psi_g|(\Lambda-H)^m\hat{A}(\Lambda-H)^{n-m}|\bar{\phi}\rangle}{\langle\psi_g|(\Lambda-H)^n|\bar{\phi}\rangle}, \tag{3.75}$$

where $n-m$ is the iteration at which the operator is applied. Thus Eq. (3.72) becomes

$$\langle\psi_{GS}|\hat{A}|\psi_{GS}\rangle \simeq \frac{\sum_{n=n_0}^{M} G_{n,\tilde{n}} A_{x_{n-m}}}{\sum_{n=n_0}^{M} G_{n,\tilde{n}}}, \tag{3.76}$$

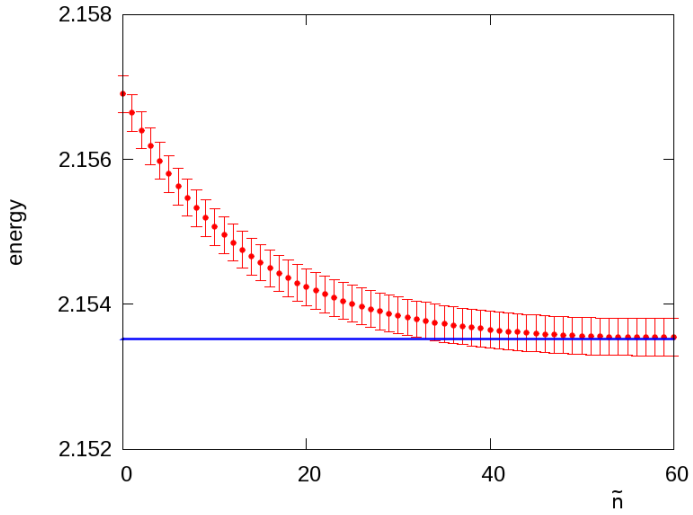

Figure 3.10: Points: GFMC energy (Eq. 3.72) of the Hamiltonian in Eq. (1.42), as a function of $\tilde{n}$. The solid horizontal line corresponds to the exact energy, computed by the ED scheme described in section 3.1. System of 8 bosons on 8 sites, with $(J, U, V) = (1, 5, 4)$.

that is valid for $\tilde{n} \gg 1$ and $m \gg 1$.

The scheme described here can be generalized to use many walkers simultaneously. If one wants to keep the number of walkers fixed, a reconfiguration scheme has to be used to avoid that a few walkers gain a very large weight compared to the others. The results shown in chapter 5 are obtained through a many-walkers GFMC scheme that makes use of the stochastic reconfiguration technique (see Ref. [84]).

Chapter 4

Trapped model: mean-field results

In this chapter, we show the results of the mean-field approach described in section 3.2.2 for the trapped Bose-Hubbard model. In particular, we measure the visibility of the quasimomentum distribution (introduced in section 2.1) and we describe which features are found in the mean-field results.

In section 4.1, we consider a 1D system and we show how the choice of different trapping potentials leads to different visibility curves. The results for 2D systems are shown in section 4.2, where we describe both a pure 2D system and a 2D system that constitutes the central layer of a 3D one.

4.1 1D system

In this section we show the results of our calculations in a one-dimensional system. In particular we have studied (for different values of U/J) the following two systems

- system of $N = 80$ bosons in $N_s = 79$ lattice sites, trapping potential $V_T(i) = (0.06\ J)\ i^2$;
- system of $N = 80$ bosons in $N_s = 79$ lattice sites, trapping potential $V_T(i) = (0.003\ U)\ i^2$.

Throughout this section we set the lattice constant a to one.

In the weakly interacting regime (small U/J) the entire system is in the superfluid phase; for larger values of U/J, we observe the formation of the Mott domains with $n = 1$; for even stronger interactions, the two Mott regions with $n = 2$ appear around the central superfluid domain, and they get connected when the interactions increase further. The first way of observing this phase structure comes by looking at the local density profile n_i, that is pinned to integer values in the Mott domains (examples are shown

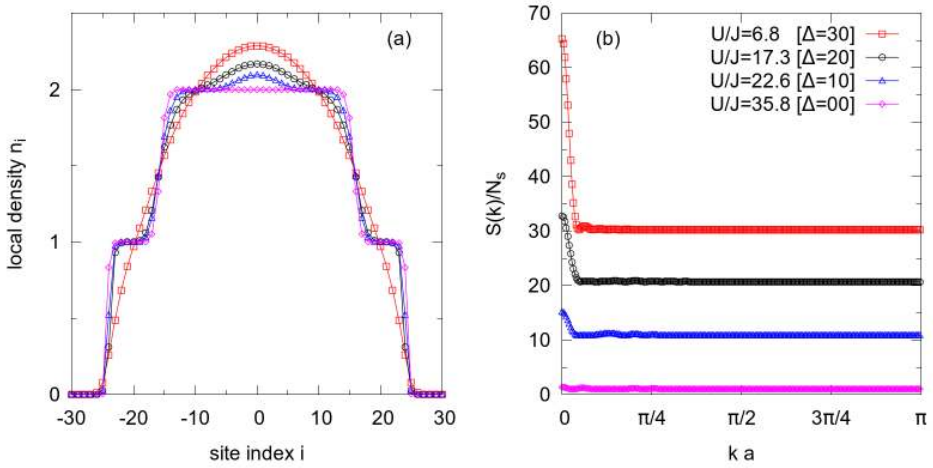

Figure 4.1: System of 80 bosons in 79 lattice sites, trap $V_T(i) = (0.003\ U)i^2$. (a) Profiles of the local density n_i, for different values of U/J (see legend in (b)). (b) Quasimomentum distribution $S(k)$ divided by the number of sites, for different values of U/J; data are vertically shifted by Δ for clarity, see legend.

in Figures 4.2(a) and 4.1(a)). Moreover, we have measured the local order parameter ($\psi_i = \langle \hat{b}_i \rangle$) and the local density fluctuations ($\sigma_i^2 = \langle \hat{n}_i \rangle^2 - \langle \hat{n}_i^2 \rangle$); a finite value of these two quantities is a signature of the superfluid phase (an example is shown in Fig. 4.5).

The presence of coherent superfluid domains determines sharp interference peaks in the quasimomentum distribution $S(k)$, as discussed in section 1.6; as expected, we observe that for larger values of U/J the interference peaks become smaller and $S(k)$ consists only in a uniform incoherent background. This is shown in Figures 4.2(b) and 4.1(b).

From the data for $S(k)$, it is possible to measure the visibility $\mathcal{V}$; in Note 1 (page 26) we have described how this is to be done in 1D. The results for the two choices of the trapping potential are shown in Figures 4.3(b) and 4.4(b), together with the corresponding canonical trajectories in the homogeneous phase diagram (Figures 4.3(a) and 4.4(a)). The first appearance of $n = 1$ Mott regions does not lead to clear features in the visibility, and the same is true for the appearance of the $n = 2$ Mott shoulder around the central superfluid domains. On the contrary, the closure of the $n = 2$ Mott domain in the center is clearly signaled in the visibility by a change of slope.

This main kink is clear in both the cases we are describing, but the case shown in Fig. 4.3 (where the trap curvature is proportional to J and thus decreasing for larger U/J) has also some additional features in the regime of strong interactions (i.e. large U/J). As shown in Fig. 4.5, the local order parameter and the density fluctuations show oscillations as functions of U/J

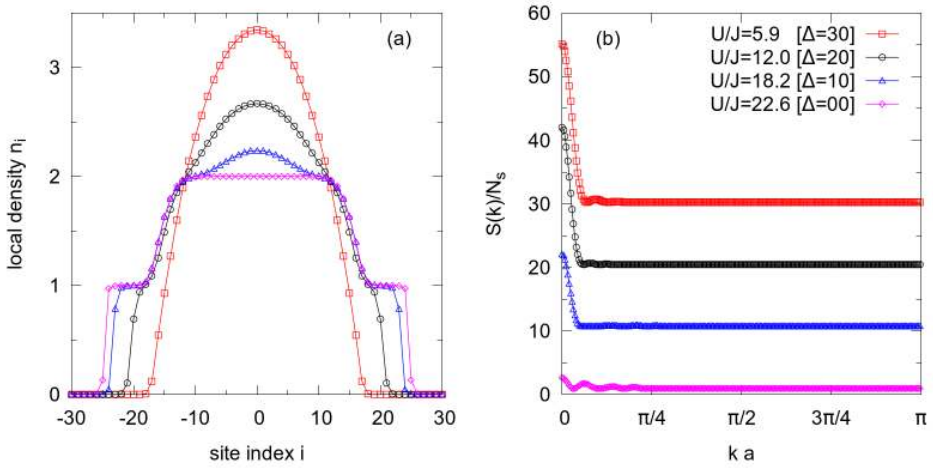

Figure 4.2: System of 80 bosons in 79 lattice sites, trap $V_T(i) = (0.06\ J)i^2$. (a)-(b): same as in caption of Fig. 4.1.

in the region where the local density is between 0 and 1. This effect is due to the competition between the trapping energy (that pushes bosons towards the center) and the on-site repulsion, and it has strong consequences on the visibility (that is larger when more bosons are in the superfluid regions). In the other case (i.e. when the trap frequency is proportional to U, thus getting larger for increasing U/J), the visibility decay is smooth, after the kink; no oscillations are observed in the local order parameter and in the density fluctuations, and in fact no oscillations are present in the visibility.

As reviewed in section 2.3, an effect similar to these oscillations is observed in the QMC study in Ref. [50] (in which a trap curvature proportional to J is used). Note that the oscillations observed here originate from the oscillations in the superfluid regions with $0 < n < 1$, whereas the ones in Ref. [50] are explained by the change of size of the superfluid regions with $1 < n < 2$; however the mechanism is the same and it is based on the interplay between the trapping potential and the on-site repulsion that leads to a certain density structure. It has to be stressed that in 1D the QMC and mean-field phase diagrams are qualitatively different, thus a quantitative agreement between the two methods is not expected.

Our observations lead to the conclusion that the influence of different trapping potentials on the density structure (given by the competition with the repulsive interaction) has an effect also on the visibility of the system. This is clear by looking at the regime of large U/J in our results, while in the weakly interacting regime the visibility features are similar for the two choices of the trap.

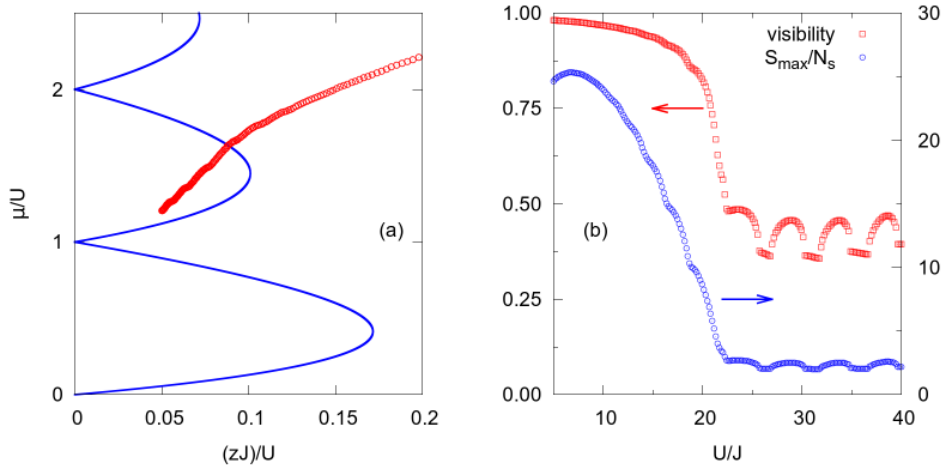

Figure 4.3: System of 80 bosons in 79 lattice sites, trap $V_T(i) = (0.06\ J)i^2$. (a) Open circles represent $(zJ/U, \mu/U)$ points in the homogeneous mean-field phase diagram; μ is the external chemical potential, $z = 2$ is the number of nearest neighbours of each site. (b) Visibility of the quasimomentum distribution, computed as described in Note 1 (page 26).

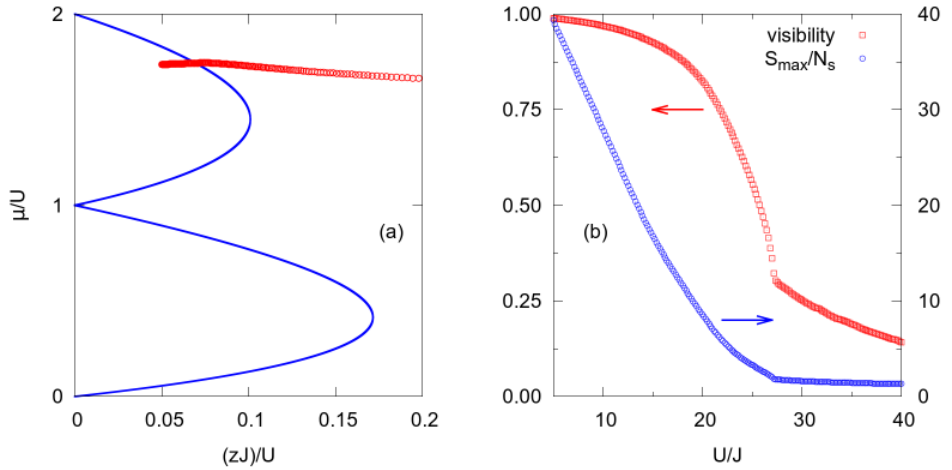

Figure 4.4: System of 80 bosons in 79 lattice sites, trap $V_T(i) = (0.06\ J)i^2$. (a)-(b): same as in caption of Fig. 4.3.

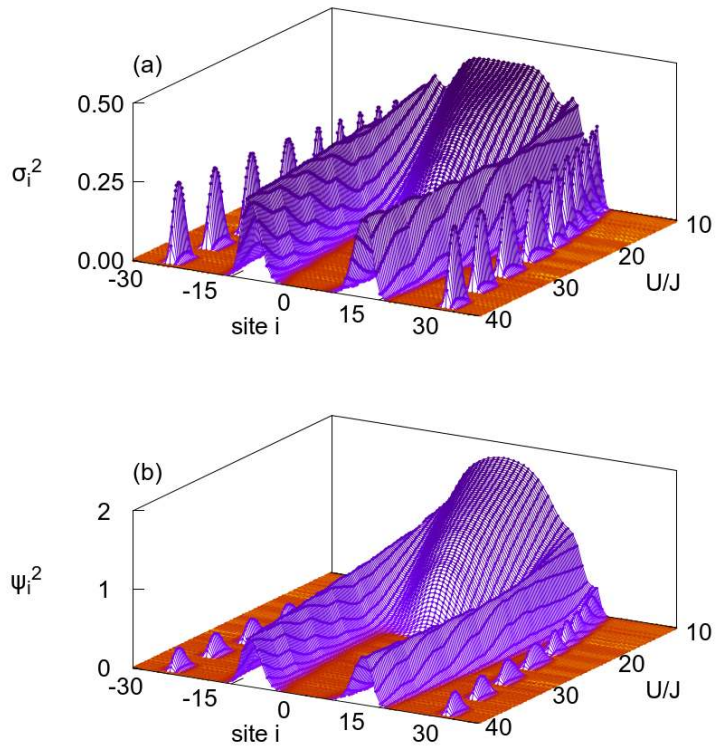

Figure 4.5: System of 80 bosons in 79 lattice sites, trap $V_T(i) = (0.06\ J)i^2$. Plots of the local density fluctuations σ_i^2 (a) and the local order parameter squared: ψ_i^2 (b) , both as functions of U/J.

4.2 2D system

When considering a 2D system, we choose the parameters of the model to be relevant for a comparison with experiments. In particular we consider a system in an isotropic trapping potential with frequency as in Eq. (1.34), where the external magnetic trap has $\omega_m = 30$ Hz$\times 2\pi$, $m = 86.9$ a.u. is the mass of the ^{87}Rb atoms and $w = 100$ μm is the waist of the laser beams generating the lattice. The way of obtaining 2D independent system in a 3D experimental set-up is that of setting the lattice depth in the third direction to a large value ($V_{0,z} = 28.8E_R$), so that the hopping along z is strongly suppressed and all the layers are effectively independent. The wave length of the laser beams forming the lattice is the same in the three directions ($\lambda = 1064$ nm) and the lattice depth along x and y is the same ($V_0 \equiv V_{0,x} = V_{0,y}$). [1]

For each choice of V_0, the parameters of the Bose-Hubbard model (the on-site interaction U and the hopping coefficient J in the x-y plane) are computed as explained in sections 1.2 and 1.3.

First case

As a first case, we study a trapped 2D system and we do not consider it as a part of a 3D set-up. Thus we choose a fixed number of particles ($N = 2600$), that remains constant for different lattice depths V_0. When we let V_0 vary, we observe the formation of the shell structure described in section 1.5; this is shown in Fig. 4.6. Note that we can study the density profile as a function of the distance r from the center, because of the symmetry of the trapping potential under rotations in the x-y plane.

This shell structure can be studied globally by measuring the number of bosons in the Mott and superfluid phases. In order to recognize the phase on a certain site, we check whether the local order parameter ψ_i is finite or vanishing. This is done by setting a finite tolerance ε and by checking the condition $\psi_i^2 < \varepsilon$; if the condition is true, we consider the site as hosting particles in the Mott phase. Note that in this procedure (required by the fact that the numerical value of ψ_i remains small but finite even in the Mott phase) the choice of ε is arbitrary, thus the results have to be considered only qualitatively. As shown in Fig. 4.7, in the regime of weak interactions all the particles are in the superfluid phase, while for increasing lattice depth more particles become part of the Mott shells. It is clear from the data that the increase in the number of "Mott particles" is steeper for certain values of V_0/E_R, corresponding to the formation of the different Mott domains; with the help of the density profiles shown in Fig. 4.6, it is possible to explain

[1] The parameters that we have listed here are comparable to the ones used in current experiments with optical lattices; in particular, they are relevant for a set-up used in Andreas Hemmerich's group at the Institut für Laserphysik (Hamburg, Germany).

some of these features. For $V_0 \simeq 14.75E_R$ the Mott shell with $n = 3$ starts to form around the central superfluid domain, and this corresponds to a sudden increase in the number of particles in the Mott state. The other steep increase in this quantity is for $V_0 \simeq 15.5E_R$, corresponding to the closure of the Mott domain in the center.

In Fig. 4.8, we show the visibility $\mathcal{V}$ (computed as in Eq. (2.5)) and its numerical derivative. By looking at the derivative, it is possible to recognize some features in $\mathcal{V}$. In particular for $V_0/E_R \simeq 14.75$ and $V_0/E_R \simeq 15.5$ the visibility has some kinks, in which its decay is steeper; these correspond to the features previously recognized in the density profiles and in Fig. 4.7. A different feature takes place at $V_0/E_R \simeq 16.85$; this is a point at which the decay of $\mathcal{V}$ is less steep (whereas the previous features have the opposite behaviour). The explanation is that at this value of V_0 the number of particles in the Mott state decreases (as seen in Fig. 4.7), before increasing again. For this reason, the decay of $\mathcal{V}$ "slows down" around that point. Note that the fact that the number of particles in the Mott state is not always monotonously increasing with V_0 is not contradictory, since also the trapping potential depends on V_0 and it competes with the repulsive interaction in redistributing the particles in the system.

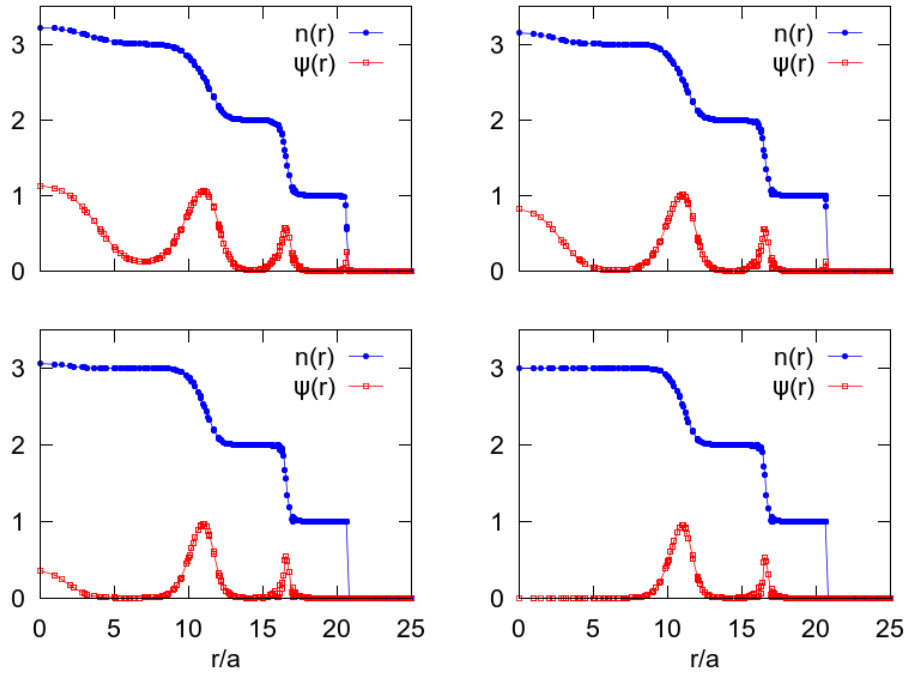

Figure 4.6: Radial dependence of the local density $n(r)$ (blue full circles) and local order parameter $\psi(r)$ (red empty squares). The four plots are for $V_0/E_R = 14.25$, 14.75, 15.25, 15.5 (ordered row by row).

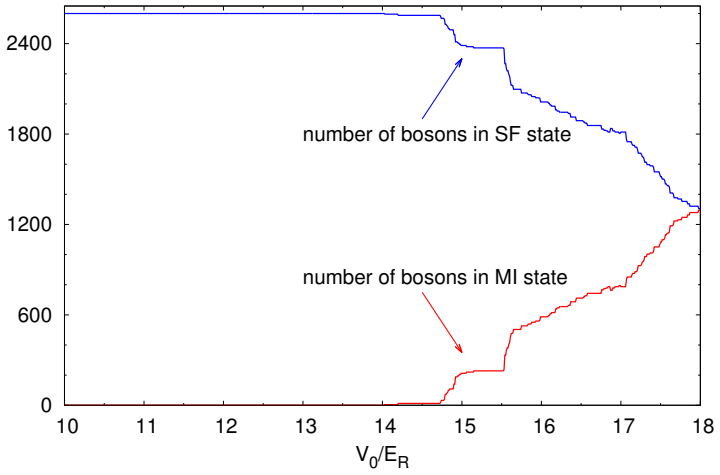

Figure 4.7: Number of particles in the two phases (Mott insulator and superfluid) for a 2D system with $N = 2600$ bosons, as a function of the lattice depth in the x-y plane.

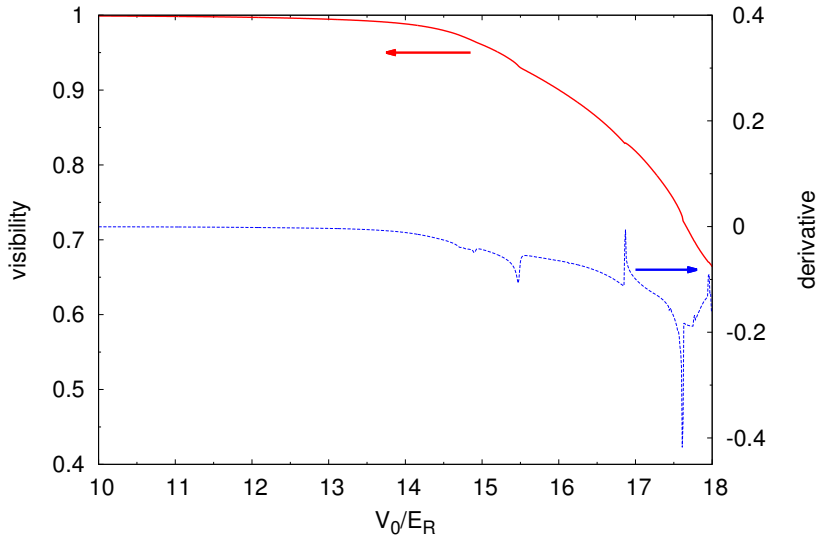

Figure 4.8: Visibility (upper curve) and its numerical derivative (lower curve) for a 2D system with $N = 2600$ bosons, as functions of the lattice depth in the x-y plane.

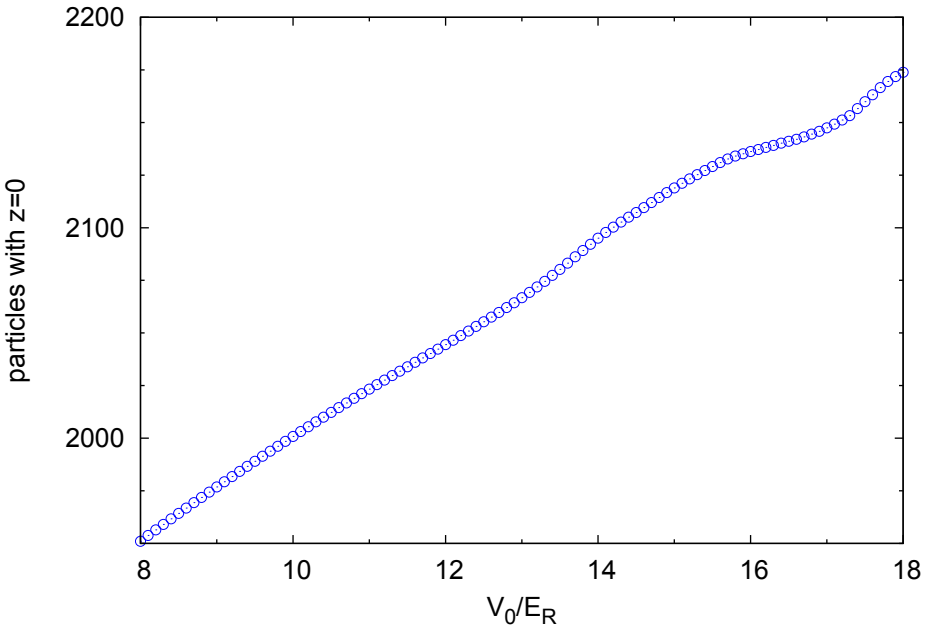

Figure 4.9: Number of particles in the $z = 0$ layer of a 3D system with a deep lattice along z ($V_{0,z} = 28.8E_R$) and 5.5×10^4 particles, as a function of the lattice depth V_0 in the x-y plane. The parameters of the trapping potential are given in the text.

Second case

As a second example, we choose a simulation more relevant for comparison with experiments. We assume that the 2D system that we study is a part of the 3D experimental set-up, in which the strong lattice depth along z makes the 2D layers with fixed z effectively independent, since no particle hopping takes place between them. The difference with the first example is that here we consider a specific layer of the 3D system (the one with $z = 0$); the number of particles in this layer depends both on $V_{0,z}$ and on V_0, thus it is not constant for different V_0. The scheme we follow is that of simulating the full 3D system to extract the number of particles in the $z = 0$ layer $N_{z=0}(V_0)$ and using this as an input for the simulation of the 2D system. In Fig. 4.9 we show $N_{z=0}(V_0)$ for a total of 5.5×10^4 bosons in the 3D system. Apart from this detail, the mean-field calculations are the same as in the previous example.

In Fig. 4.10 we show some radial density profiles for different values of U/J, that is for different values of V_0/E_R; at $U/J \simeq 55$ the Mott shell with $n = 2$ appears, while at $U/J \simeq 63$ the Mott domain with $n = 3$ starts to form (from the center of the trap).

As in the previous section, some kinks in the visibility (Fig. 4.11) correspond to these specific points. Note that the first kink is slightly shifted to larger U/J w.r.t. to the point $U/J \simeq 63$ at which the Mott domain appears in the center; this means that the kink in the visibility corresponds to the situation in which the size of this domain becomes relevant.
The trajectory corresponding to the chosen parameters enters the $n = 3$ Mott lobe close to its tip, in the homogeneous phase diagram (not shown); for this reason, the kink in the visibility corresponding to the closure of the Mott in the center of the trap is close to the expected mean-field value for the tip of the lobe (see vertical line in Fig. 4.11).
For large values of U/J, the sizes of the superfluid shells with density $n \in [1, 2]$ and $n \in [0, 1]$ have an oscillating behaviour as functions of U/J; as explained in section 4.1, this is an effect of the interplay between the trap and the repulsion, and it is linked to the features in the visibility for $U/J \gtrsim 90$.

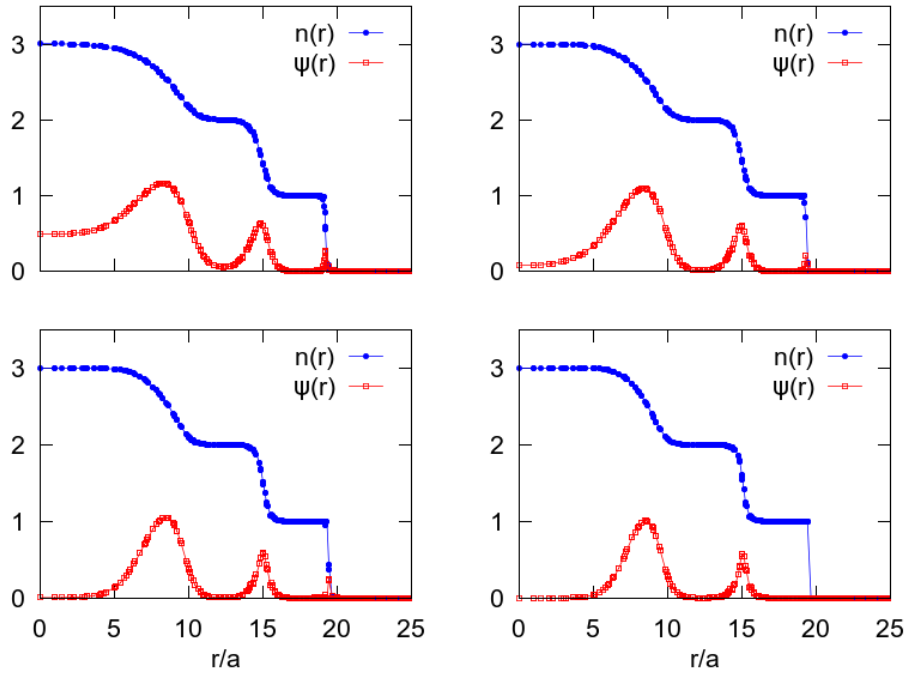

Figure 4.10: Radial dependence of the local density $n(r)$ (blue full circles) and local order parameter $\psi(r)$ (red empty squares). The four plots are for $U/J = 46.2, 55.6, 64.3, 74.9$ (ordered row by row), corresponding to $V_0/E_R = 13.25, 14, 14.6, 15.25$.

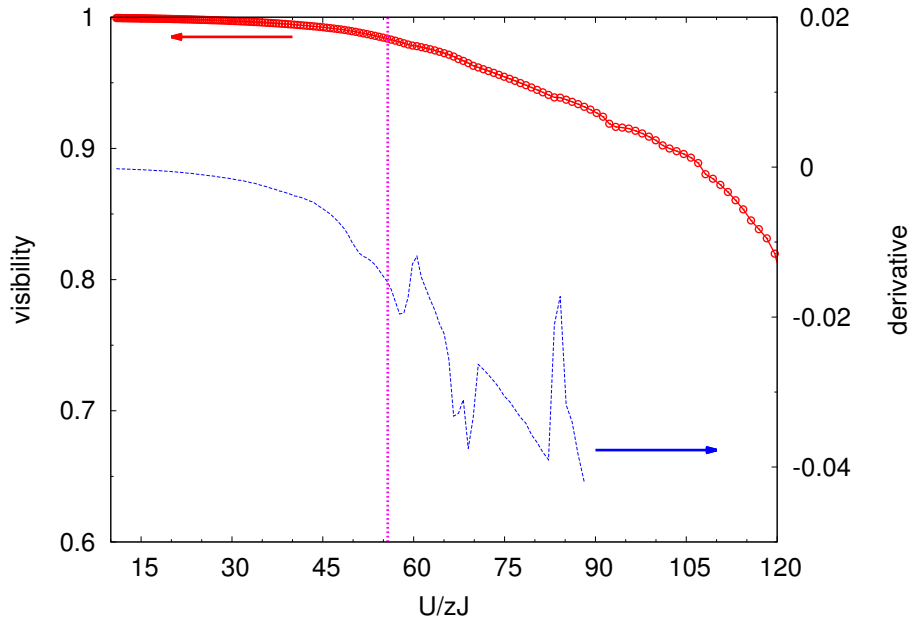

Figure 4.11: Visibility (upper curve) and its numerical derivative (lower curve) for a 2D system with varying number of bosons, as functions of the dimensionless ratio U/J. The vertical dashed line corresponds to $U/J = 55.71$, the tip of the lobe for the homogeneous system in the mean-field approach (see Ref. [57]). The x-axis range corresponds approximately to $V_0/E_R \in [8, 17.3]$; for large U/J the derivative of $\mathcal{V}$ has strong oscillations and it is not shown here.

Chapter 5

Extended model: QMC results

In this chapter we show the results of our QMC simulations of the one-dimensional extended Bose-Hubbard model (Eq. 1.42). First we have verified that the GFMC code used here is able to reproduce exact results, obtained through exact diagonalization; this is described in section 5.1. In section 5.2 we show our results in the characterization of the different phases of the 1D extended Bose-Hubbard model. In particular, we describe the difference between the two insulating phases (Mott and Haldane insulators) and we verify numerically an analytic estimate (from Ref. [85]) of the way in which the parity order parameter decays in the superfluid phase.

The numerical approach that we use is the GFMC scheme described in section 3.4.2. As a guiding wave function for the importance sampling, we chose the following wave function $|\psi\rangle$ for a system of N bosons

$$|\psi\rangle = \exp\left(\frac{1}{2}\sum_{i,j} v_{ij}\hat{n}_i\hat{n}_j\right)|\phi_0\rangle, \tag{5.1}$$

where $|\phi_0\rangle$ is the condensate wave function

$$|\phi_0\rangle \propto \left(\sum_i \hat{b}_i^\dagger\right)^N |0\rangle. \tag{5.2}$$

This choice of $|\psi\rangle$ is also used – for instance – in Ref. [68]. The operator that is applied on $|\phi_0\rangle$ is a Jastrow factor that introduces a correlation between the sites i and j, depending on the coefficient v_{ij}. We assume that the coefficients v_{ij} depend only on the distance $|i-j|$, because of the translational invariance of the Hamiltonian Eq. (1.42). Note that Periodic Boundary Conditions are required to have the full translational invariance; this means that the sites 1 and N_s are seen as nearest neighbours.

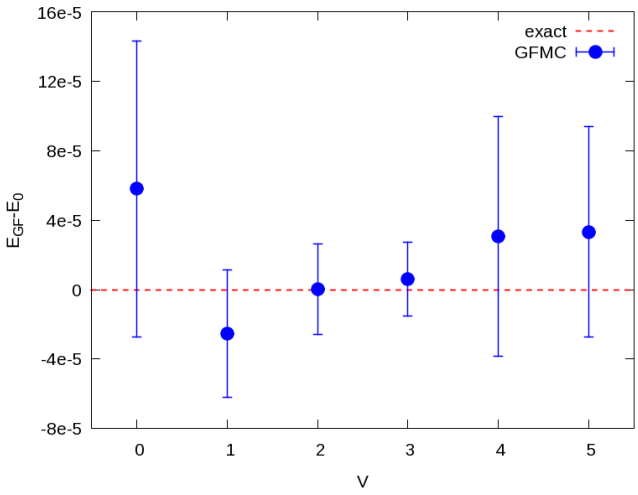

Figure 5.1: Difference of the ground state energy computed by GFMC and its exact value; system of 8 bosons on 8 sites, with $J = 1$ and $U = 5$. V is the next-nearest-neighbour repulsion, as in Eq. (1.42).

VMC and stochastic minimization have been used to find the optimal coefficients v_{ij}, before using $|\psi\rangle$ as a guiding function in the GFMC scheme. Note that the presence of a trapping potential would require some modifications of this approach, since the homogeneity of the system would be explicitly broken by $V_T(x)$. A first solution would be that of considering the coefficients v_{ij} explicitly dependent on the sites i and j. Note that this would increase the number of variables in the VMC optimization, from $N_s/2$ (the number of inequivalent distances for N_s even) to N_s^2 (the total number of pairs of sites).

5.1 Validation of the GFMC scheme

In order to validate our GFMC approach, we have compared the results with the exact ones, obtained through ED on small lattices. In Fig. 5.1 we show a comparison of the ground state energy computed through GFMC with the exact one. The results are in good agreement; the error bars could be reduced further by using a larger number of walkers or of MC steps.

The same comparison is shown in Fig. 5.2 for the three order parameters defined in Eqs (1.46) (string order parameter), (1.45) (parity order parameter) and (1.44) (density wave order parameter). Also in this case, the difference between GFMC results and exact ones is of the order of the statistical error bars.

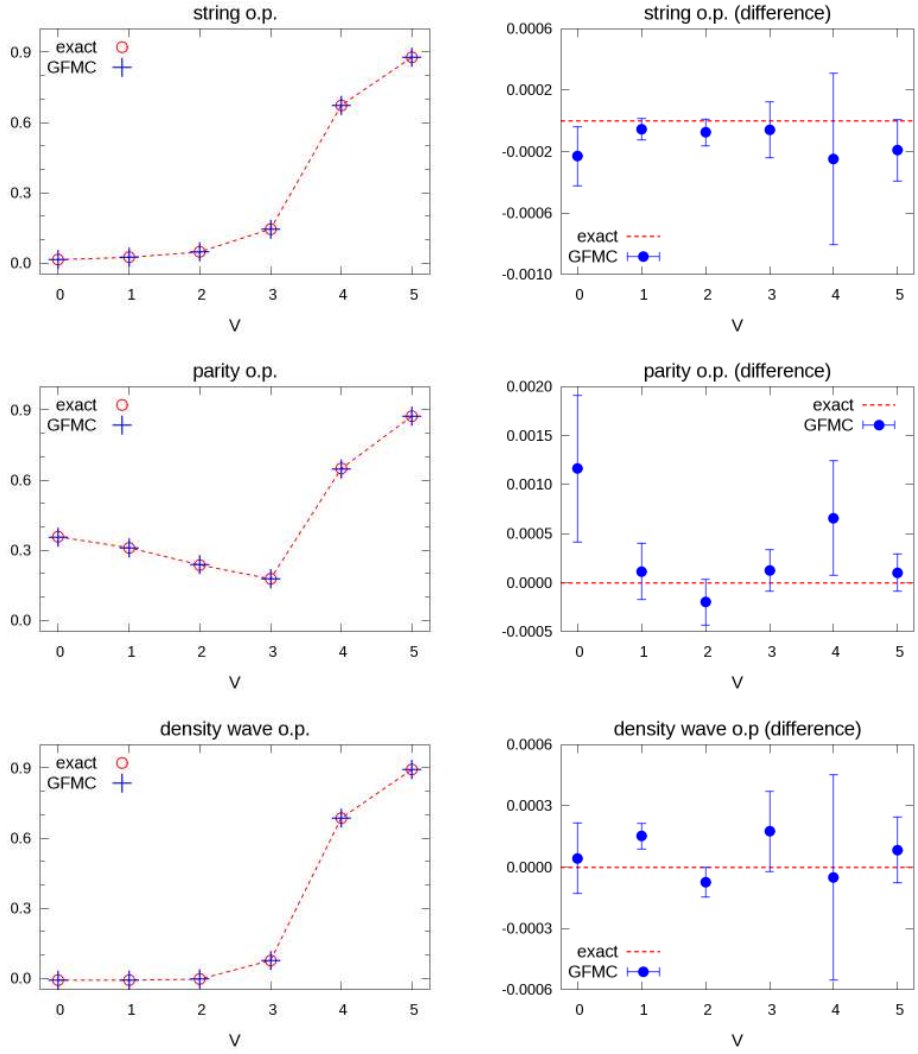

Figure 5.2: Comparison of GMFC and exact results for the string, parity and density wave order parameter in a system of 8 bosons on 8 sites; results for $J = 1$, $U = 5$ and varying next-nearest-neighbour repulsion V. Left: results of ED (empty circles) and GFMC (crosses); right: difference between exact results and GFMC ones, including the statistical errors of GFMC. Dashed lines are guides to the eye.

5.2 Results

We consider systems at unitary filling ($N = N_s$), for different sizes and for different parameters J, U, V. In particular we consider three points in the phase diagram, with J and U fixed ($J = 1$ and $U = 5$). We let V vary, so that (according to the phase diagram shown in Fig. 1.9) the system is in three different phases: Mott insulator (for $V = 2.8$), Haldane insulator (for $V = 3.2$) and density wave phase (for $V = 3.65$).

Compared to the ED approach, GFMC allows the study of larger systems. For each choice of the parameters, we have repeated the simulation for systems of different sizes, in order to extrapolate the results to the thermodynamic limit. In Fig. 5.3, the size scaling is shown for the parity and string order parameters; in Fig. 5.4 the same is shown for the density wave order parameter.

The results clearly indicate the following characterization of the ground state of the system for different choices of V:

- for $V = 2.8$ the parity order parameter is non-zero while the other ones (string and density wave) vanish, therefore the system is in a Mott insulating phase;
- for $V = 3.2$ the string order parameter is non-zero while the other ones (parity and density wave) vanish, therefore the system is in a Haldane insulating phase;
- for $V = 3.65$, the three order parameters (string, parity and density wave) are non-zero, therefore the system is in a density wave phase.

5.2.1 Insulating phases

It is of particular interest to consider the difference between the two insulating phases. In both cases, there is no density wave order; however, the Haldane phase has a non-vanishing string order parameter, that corresponds to a hidden antiferromagnetic ordering. As represented in Fig. 5.5, the hidden order $+, -, +, -, ..$ is the one that would be found after removing all the sites with $n = \bar{n}$ (i.e. with $\delta n = 0$). The link between a non-vanishing string order parameter and the hidden antiferromagnetic order in the Haldane phase is the following: if one cancels all the sites with $n = \bar{n}$ (represented as zeros in the figure), all the sites left are occupied by $n = 0$ or $n = 2$ bosons. Thus the exponential that appears in the definition of the string order parameter (Eq. 1.46) only contributes a global sign, and

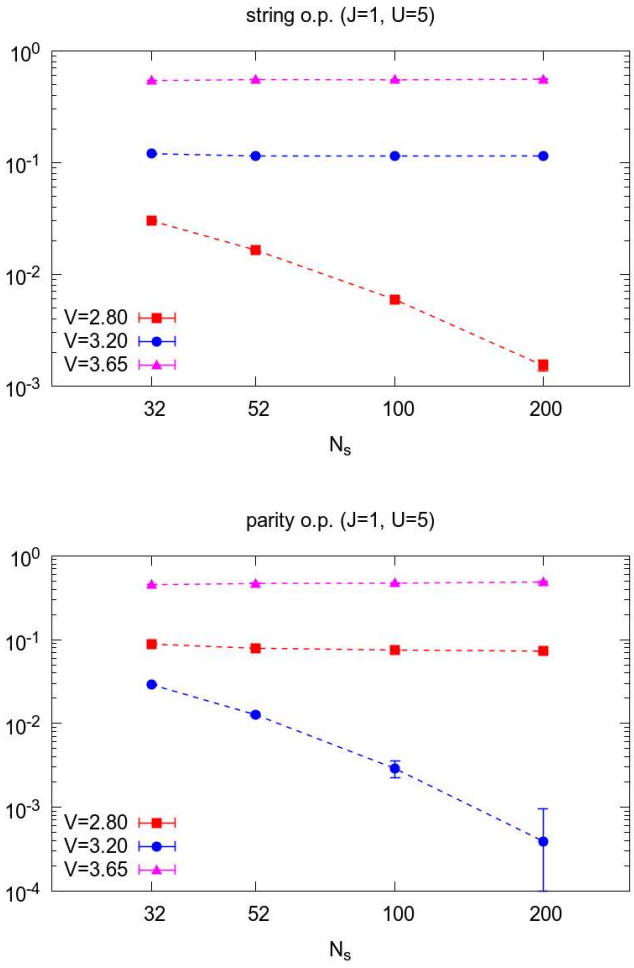

Figure 5.3: Size-scaling of the string (top) and parity (bottom) order parameters in three different phases: Mott insulator (squares), Haldane insulator (circles), density wave (triangles). The scale is logarithmic for both axis; the error bars are smaller than symbol sizes, when not explicitly shown; the dashed lines are guides to the eye.

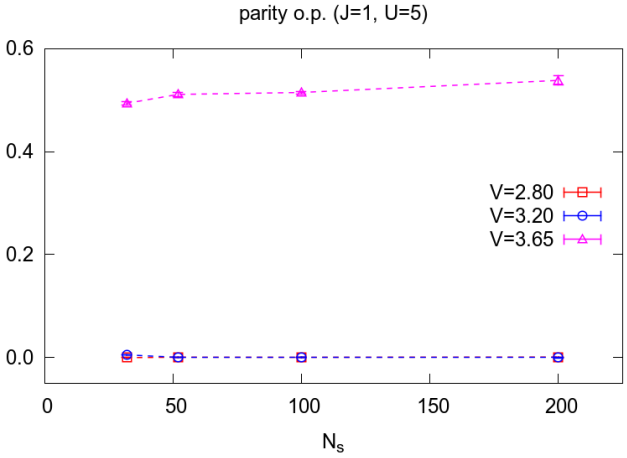

Figure 5.4: Size-scaling of the density wave order parameter in three different phases: Mott insulator (squares), Haldane insulator (circles), density wave (triangles).The error bars are smaller than symbol sizes, when not explicitly shown; the dashed lines are guides to the eye.

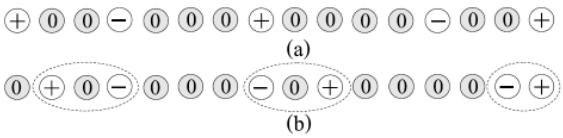

Figure 5.5: Typical configuration in the Haldane phase (a) and Mott phase (b). Average filling is one, the symbol + (−) corresponds to $n = 2$ ($n = 0$). Figure extracted from Ref. [9].

one is left with

$$\begin{aligned} C_{\mathrm{str}}(r) &\equiv \left\langle \delta\hat{n}_j \exp\left[i\pi \sum_{p=j}^{j+r-1} \delta\hat{n}_p \right] \delta\hat{n}_{j+r} \right\rangle = \\ &= \left\langle \delta\hat{n}_j \left(\prod_{p=j}^{j+r-1} (-1)^{\delta\hat{n}_p} \right) \delta\hat{n}_{j+r} \right\rangle = \\ &= (-1)^{r-1} \left\langle \delta\hat{n}_j \delta\hat{n}_{j+r} \right\rangle = \\ &= C_{\mathrm{DW}}(r). \end{aligned} \tag{5.3}$$

Thus when there are no sites with $n = \bar{n}$ the string and density wave order parameters are equivalent. On the contrary, the Mott phase shows not hidden order; the reason for the non-vanishing parity order parameter is that the Mott state corresponds to an admixture of particle-hole pairs on

top of the fixed-density background (see Refs [31, 12]).

5.2.2 Superfluid phase

In the superfluid phase, the large fluctuations in the occupation number (see section 1.4) prevent the system from developing any string or parity order. In particular, the parity order parameter is expected to decay according to the following power law (from Ref. [85])

$$C_{\mathrm{par}}(r) \sim r^{-\pi\alpha\bar{n}}, \tag{5.4}$$

where $\bar{n}$ is the average filling. The coefficient α is related to the density-density correlation function in Fourier space

$$N(q) \equiv \langle n_{-q} n_q \rangle = \frac{1}{N_s} \left\langle \sum_{i,j} e^{-iq(x_i - x_j)} n_i n_j \right\rangle ; \tag{5.5}$$

in the superfluid phase, this correlation function is linear for small values of q and α is the coefficient in $N(q) \simeq |\alpha| q$.

For $J = 1$ and $V = 0$, the Mott transition is expected around $U = 3.61 \pm 0.01$ (see Ref. [34]). In Figures 5.6 and 5.7 we show the results for $N(q)$ and $C_{\mathrm{par}}(r)$ at $U = 2.5$ and $U = 3$, that is in the superfluid phase. The values of α from the different fits are shown in Table 5.1.

	$U = 2.5$	$U = 3$
α from fit of $N(q)$	0.434 ± 0.003	0.3833 ± 0.0016
α from fit of $C_{\mathrm{par}}(r)$	0.436 ± 0.013	0.391 ± 0.008

Table 5.1: Results for α.

As shown in Fig. 5.7, the parity correlator at large distance has strong fluctuations; this is also due to finite size effects. Moreover, different ranges for the fit can be chosen, thus including some arbitrariness in the results. The study of larger systems and a better statistics (i.e. a larger number of GFMC walkers and Monte Carlo steps) would reduce the statistical errors and make this arbitrariness less relevant. Despite these remarks, the results for α are in agreement, thus proving the statement in Ref. [85].

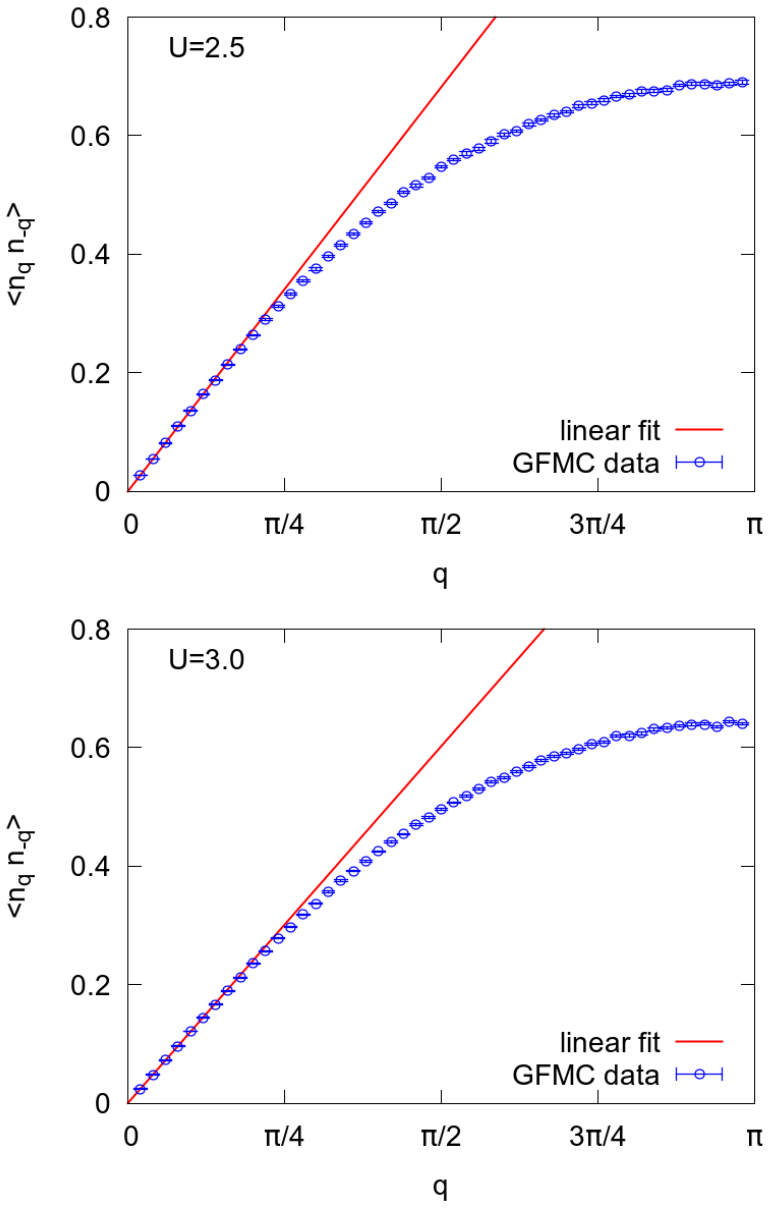

Figure 5.6: Density-density correlation function in Fourier space (Eq. 5.5) for a system of 100 bosons on 100 sites with $J = 1$. Results for $U = 2.5$ (top) and $U = 3$ (bottom). Fit range: $q \in [0, 0.4]$. Statistical errors (generally smaller than the symbol sizes) are shown.

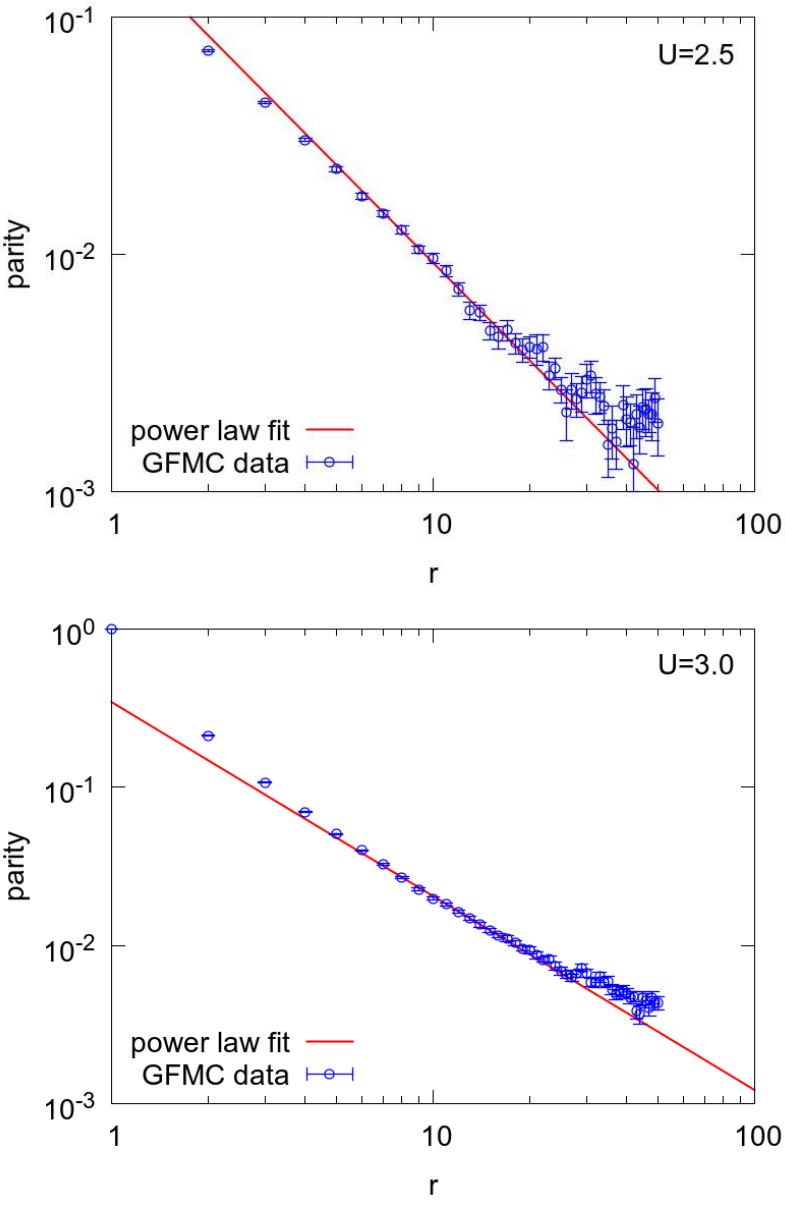

Figure 5.7: Parity correlation function for a system of 100 bosons on 100 sites with $J = 1$. Results for $U = 2.5$ (top) and $U = 3$ (bottom). Fit range: $r \in [7, 20]$.

Conclusions and outlook

In this thesis we have studied two different versions of the Bose-Hubbard model: the inhomogeneous model in presence of a confining potential (in one and two dimensions) and the homogeneous model with nearest-neighbour repulsive interactions. Here we present our conclusions and we mention the open questions and the possible developments of this work.

Trapped system

In chapter 4 we have shown the results for the study of the trapped Bose-Hubbard model, obtained through the mean-field approach described in section 3.2.2. First, we have considered the 1D system and we have computed its properties (including the density profile, the quasimomentum distribution and the visibility) for different values of the ratio U/J between the on-site repulsion and the hopping parameter. We have considered different choices for the dependence of the trapping potential on the energy scales of the system, leading to qualitative differences in the visibility. This is explained by the fact that the coherence properties (including the visibility) depend on the density structure, that is determined by the competition between the different terms in the Hamiltonian (including the trapping potential). A peculiar feature (the presence of oscillations in the visibility) is observed in the case in which the curvature of the trap scales proportionally to the hopping parameter; a similar effect (although with possible different explanation) is described in Ref. [50]. We stress that the choice of the scaling of the trapping potential has to be carefully taken into account, when the goal is the comparison with experimental results.

In the pure 2D case, we have studied the system by looking at how its observables (the shell structure, the number of particles in the two phases and the visibility) depend on the lattice depth V_0. We have recognized some features (kinks) in the visibility, that we are able to link to the opening or closure of Mott shells. Analogous features can be found in the number of particles that are in each one of the two phases. When we consider a single layer that is part of a 3D system, we observe the same features. However, these are less clear and that can be due to the fact that the number of particles in a single layer is not constant as a function of the lattice depth.

Both in the 1D and 2D cases, we observe features (kinks or oscillations) in the visibility, that we are able to interpret as signatures of some "event" as the formation of Mott domains. It has to be stressed that not all these events correspond to a clear signature in the visibility; this can also be the effect of the small number of particles in some Mott domains of the system.

Different questions remain open about the experimental measurements of the visibility and of the kinks. A first issue is the one of adiabaticity: if the ramping of the lattice takes place too fast, it is possible that the system does not reach its true ground state. This scenario is explained for instance in Refs [86, 87], while from the conclusions of Refs [53, 45] it seems that with the parameters of current experiments the lattice ramping is slow enough. One way of answering this question using the mean-field approach would be the use of a time-dependent Gutzwiller scheme to simulate the full experimental procedure, including the ramping of the lattice.

A possible improvement of the numerical solution technique would be the *cluster* Gutzwiller scheme, that has been recently used in Ref. [64] for a precise study of the homogeneous Bose-Hubbard phase diagram. In this approach, the system is covered with small patches (inside which exact diagonalization is performed) and the mean-field scheme is used to connect different patches.

Another relevant open question is related to the comparison with experimental results for the 2D systems. As described in section 4.2, the way to realize 2D systems in a 3D set-up is through the suppression of the hopping along one direction; this leads to an array of effectively independent 2D layers. The time-of-flight measurement includes contributions from different layers (that can host different density structures), thus it is not clear whether the simulation of a single layer (namely the one with $z = 0$) can be used to describe the experimental results. Note that in the set-up described in Ref. [48] it is possible to select a few of these layers for the adsorption imaging, but this is a specific technique not used in all the experiments.

Hidden order in the extended model

In chapter 5 we have shown the results of our study of the one-dimensional extended Bose-Hubbard model, obtained through the GFMC scheme described in section 3.4.2. We have studied the system at unitary filling and we have computed the relevant order parameters in some points of the $T = 0$ phase diagram, in order to recognize different phases. In particular we have characterized the transitions between Mott and Haldane insulating phases and between Mott and superfluid phases by studying the string and parity order parameters.

The calculations have been done with a many-walkers GFMC scheme with importance sampling, in which the guiding function has been chosen

by optimizing the parameters in a variational ansatz. The scheme correctly reproduces the exact results obtained through diagonalization of the Hamiltonian on small lattices.

For three sets of parameters corresponding to the three different phases of the system at large on-site repulsion U, we have performed a size-scaling of the relevant order parameters and found agreement with the phase diagram proposed in the literature [10, 11]. In particular, we have shown the difference between the Mott and the Haldane insulating phases, characterized trough the parity and string order parameters.

For the model without nearest-neighbour interactions, we have studied the parity correlation function and verified that it has the expected behaviour at large distance, i.e. it does not vanish in the Mott phase while it decays exponentially in the superfluid phase. In Ref. [85] it is suggested that the exponent for the decay in the superfluid phase is related to the small-momentum behaviour of the density-density correlation function, as we have verified numerically.

The study of non-local order can be relevant to characterize the Mott insulator phase also for systems in dimensions higher than one. In particular the parity order can be used to distinguish the Mott phase from the superfluid one, also in the usual Bose-Hubbard model (including only nearest-neighbour hopping and on-site repulsion). In dimensions higher than one, the generalization of the definition of non-local correlators is not unique. In 2D – for instance – the correlators can be evaluated both on two-dimensional domains or along one-dimensional loops. One possibility for this generalization has been recently proposed in Ref. [85], but this is not yet supported by numerical simulations.

The interest in this characterization of different phases is also linked to the fact that recent *in-situ* measurements in experiments with cold atoms in optical lattices access the parity of the local density, rather than the local density itself. In Ref. [12] the authors perform this kind of experiment for a trapped system and measure the (non-local) parity order parameter, showing that its non-vanishing value is characteristic of the Mott phase.

Moreover, we mention that similar considerations apply to the case of fermions. In Ref. [13], the 1D fermionic Hubbard model is studied by means of bosonization and DMRG, using spin and charge non-local order parameters to characterize the Mott-insulator and Luther-Emery phases.

Acknowledgements

First of all, I thank my supervisor, Cristiane de Morais Smith. Her knowledge and ideas have been necessary for this thesis, and her enthusiasm contributed a lot in pushing me forward, for this thesis and for my future work. Special thanks are due to Marco di Liberto, who has spent a large fraction of his time in this project, providing invaluable help.
Part of the work for this thesis has been done in Trieste, at the International School for Advanced Studies. Federico Becca is thanked for his expert guide while I was there, and financial support from the institute is acknowledged.
Last but not least, I thank my friends (in Utrecht and abroad) for the necessary distractions and my family for the constant support.

Bibliography

[1] R. P. Feynman. Simulating Physics with Computers. *International Journal of Theoretical Physics*, 21(6-7):467–488, 1982.

[2] M. P. A. Fisher, P. B. Weichman, G. Grinstein, and D. S. Fisher. Boson localization and the superfluid-insulator transition. *Phys. Rev. B*, 40:546–570, Jul 1989.

[3] D. Jaksch, C. Bruder, J. I. Cirac, C. W. Gardiner, and P. Zoller. Cold Bosonic Atoms in Optical Lattices. *Phys. Rev. Lett.*, 81:3108–3111, Oct 1998.

[4] M. Greiner, O. Mandel, T. Esslinger, T. W. Hansch, and I. Bloch. Quantum phase transition from a superfluid to a Mott insulator in a gas of ultracold atoms. *NATURE*, 415(6867):39–44, Jan 2002.

[5] N. Gemelke, X. Zhang, C.-L. Hung, and C. Chin. In situ observation of incompressible Mott-insulating domains in ultracold atomic gases. *NATURE*, 460(7258):995–U75, Aug 2009.

[6] J. F. Sherson, C. Weitenberg, M. Endres, M. Cheneau, I. Bloch, and S. Kuhr. Single-atom-resolved fluorescence imaging of an atomic Mott insulator. *NATURE*, 467(7311):68–U97, Sep 2010.

[7] W. S. Bakr, A. Peng, M. E. Tai, R. Ma, J. S., J. I. Gillen, S. Fölling, L. Pollet, and M. Greiner. Probing the Superfluid–to–Mott Insulator Transition at the Single-Atom Level. *Science*, 329(5991):547–550, 2010.

[8] E. G. Dalla Torre, E. Berg, and E. Altman. Hidden Order in 1D Bose Insulators. *Phys. Rev. Lett.*, 97:260401, Dec 2006.

[9] E. Berg, E. G. Dalla Torre, T. Giamarchi, and E. Altman. Rise and fall of hidden string order of lattice bosons. *Phys. Rev. B*, 77:245119, Jun 2008.

[10] D. Rossini and R. Fazio. Phase diagram of the extended Bose–Hubbard model. *New Journal of Physics*, 14(6):065012, 2012.

[11] G. G. Batrouni, R. T. Scalettar, V. G. Rousseau, and B. Grémaud. Competing Supersolid and Haldane Insulator Phases in the Extended One-Dimensional Bosonic Hubbard Model. *Phys. Rev. Lett.*, 110:265303, Jun 2013.

[12] M. Endres, M. Cheneau, T. Fukuhara, C. Weitenberg, P. Schauß, C. Gross, L. Mazza, M. C. Bañuls, L. Pollet, I. Bloch, and S. Kuhr. Observation of Correlated Particle-Hole Pairs and String Order in Low-Dimensional Mott Insulators. *Science*, 334(6053):200–203, 2011.

[13] A. Montorsi and M. Roncaglia. Nonlocal Order Parameters for the 1D Hubbard Model. *Phys. Rev. Lett.*, 109:236404, Dec 2012.

[14] L. Pollet. Recent developments in quantum Monte Carlo simulations with applications for cold gases. *Reports on Progress in Physics*, 75(9):094501, 2012.

[15] D. M. Ceperley. Path integrals in the theory of condensed helium. *Rev. Mod. Phys.*, 67:279–355, Apr 1995.

[16] S. R. White. Density matrix formulation for quantum renormalization groups. *Phys. Rev. Lett.*, 69:2863–2866, Nov 1992.

[17] U. Schollwöck. The density-matrix renormalization group in the age of matrix product states. *ANNALS OF PHYSICS*, 326(1, SI):96–192, 2011.

[18] F. Verstraete, V. Murg, and J. I. Cirac. Matrix product states, projected entangled pair states, and variational renormalization group methods for quantum spin systems. *ADVANCES IN PHYSICS*, 57(2):143–224, 2008.

[19] L. Fallani, J. E. Lye, V. Guarrera, C. Fort, and M. Inguscio. Ultracold Atoms in a Disordered Crystal of Light: Towards a Bose Glass. *Phys. Rev. Lett.*, 98:130404, Mar 2007.

[20] A. Eckardt, C. Weiss, and M. Holthaus. Superfluid-Insulator Transition in a Periodically Driven Optical Lattice. *Phys. Rev. Lett.*, 95:260404, Dec 2005.

[21] L.-K. Lim, A. Hemmerich, and C. Morais Smith. Artificial staggered magnetic field for ultracold atoms in optical lattices. *Phys. Rev. A*, 81:023404, Feb 2010.

[22] J. Dalibard, F. Gerbier, G. Juzeliūnas, and P. Öhberg. *Colloquium* : Artificial gauge potentials for neutral atoms. *Rev. Mod. Phys.*, 83:1523–1543, Nov 2011.

[23] I. Bloch. Ultracold quantum gases in optical lattices. *NATURE PHYSICS*, 1(1):23–30, Oct 2005.

[24] M. Lewenstein, A. Sanpera, V. Ahufinger, B. Damski, A. Sen(De), and U. Sen. Ultracold atomic gases in optical lattices: mimicking condensed matter physics and beyond. *Advances in Physics*, 56(2):243–379, 2007.

[25] I. Bloch, J. Dalibard, and W. Zwerger. Many-body physics with ultracold gases. *Rev. Mod. Phys.*, 80:885–964, Jul 2008.

[26] I. Bloch, J. Dalibard, and S. Nascimbène. Quantum simulations with ultracold quantum gases. *NATURE PHYSICS*, 8(4):267–276, Apr 2012.

[27] T. Lahaye, C. Menotti, L. Santos, M. Lewenstein, and T. Pfau. The physics of dipolar bosonic quantum gases. *Reports on Progress in Physics*, 72(12):126401, 2009.

[28] C. Becker, P. Soltan-Panahi, J. Kronjäger, S. Dörscher, K. Bongs, and K. Sengstock. Ultracold quantum gases in triangular optical lattices. *New Journal of Physics*, 12(6):065025, 2010.

[29] A. Eckardt, M. Holthaus, H. Lignier, A. Zenesini, D. Ciampini, O. Morsch, and E. Arimondo. Exploring dynamic localization with a Bose-Einstein condensate. *Phys. Rev. A*, 79:013611, Jan 2009.

[30] W. Zwerger. Mott–Hubbard transition of cold atoms in optical lattices. *Journal of Optics B: Quantum and Semiclassical Optics*, 5(2):S9, 2003.

[31] F. Gerbier, A. Widera, S. Fölling, O. Mandel, T. Gericke, and I. Bloch. Phase Coherence of an Atomic Mott Insulator. *Phys. Rev. Lett.*, 95:050404, Jul 2005.

[32] B. Capogrosso-Sansone, Evgeny Kozik, N. Prokof'ev, and B. Svistunov. On-site number statistics of ultracold lattice bosons. *Phys. Rev. A*, 75:013619, Jan 2007.

[33] G. G. Batrouni and R. T. Scalettar. World-line quantum Monte Carlo algorithm for a one-dimensional Bose model. *Phys. Rev. B*, 46:9051–9062, Oct 1992.

[34] T. D. Kühner and H. Monien. Phases of the one-dimensional Bose-Hubbard model. *Phys. Rev. B*, 58:R14741–R14744, Dec 1998.

[35] N. Elstner and H. Monien. Dynamics and thermodynamics of the Bose-Hubbard model. *Phys. Rev. B*, 59:12184–12187, May 1999.

[36] B. Capogrosso-Sansone, Ş. G. Söyler, N. Prokof'ev, and B. Svistunov. Monte Carlo study of the two-dimensional Bose-Hubbard model. *Phys. Rev. A*, 77:015602, Jan 2008.

[37] B. Capogrosso-Sansone, N. V. Prokof'ev, and B. V. Svistunov. Phase diagram and thermodynamics of the three-dimensional Bose-Hubbard model. *Phys. Rev. B*, 75:134302, Apr 2007.

[38] I. V. Stasyuk and T. S. Mysakovych. Phase diagrams of the Bose-Hubbard model at finite temperature. *Condensed Matter Physics*, 12:539, 2009.

[39] M. Ohliger and A. Pelster. Green's Function Approach to the Bose-Hubbard Model. *World Journal of Condensed Matter Physics*, 3:125, 2013.

[40] F. Gerbier, A. Widera, S. Fölling, O. Mandel, T. Gericke, and I. Bloch. Interference pattern and visibility of a Mott insulator. *Phys. Rev. A*, 72:053606, Nov 2005.

[41] F. Gerbier, S. Foelling, A. Widera, and I. Bloch. Visibility of a Bose-condensed gas released from an optical lattice at finite temperatures. *eprint arXiv:cond-mat/0701420*, January 2007.

[42] G. G. Batrouni, V. Rousseau, R. T. Scalettar, M. Rigol, A. Muramatsu, P. J. H. Denteneer, and M. Troyer. Mott Domains of Bosons Confined on Optical Lattices. *Phys. Rev. Lett.*, 89:117203, Aug 2002.

[43] L. Pollet, S. Rombouts, K. Heyde, and J. Dukelsky. Bosons confined in optical lattices: The numerical renormalization group revisited. *Phys. Rev. A*, 69:043601, Apr 2004.

[44] S. Fölling, A. Widera, T. Müller, F. Gerbier, and I. Bloch. Formation of Spatial Shell Structure in the Superfluid to Mott Insulator Transition. *Phys. Rev. Lett.*, 97:060403, Aug 2006.

[45] F. Gerbier, S. Trotzky, S. Fölling, U. Schnorrberger, J. D. Thompson, A. Widera, I. Bloch, L. Pollet, M. Troyer, B. Capogrosso-Sansone, N. V. Prokof'ev, and B. V. Svistunov. Expansion of a Quantum Gas Released from an Optical Lattice. *Phys. Rev. Lett.*, 101:155303, Oct 2008.

[46] T. Stöferle, H. Moritz, C. Schori, M. Köhl, and T. Esslinger. Transition from a Strongly Interacting 1D Superfluid to a Mott Insulator. *Phys. Rev. Lett.*, 92:130403, Mar 2004.

[47] I. B. Spielman, W. D. Phillips, and J. V. Porto. Condensate Fraction in a 2D Bose Gas Measured across the Mott-Insulator Transition. *Phys. Rev. Lett.*, 100:120402, Mar 2008.

[48] K. Jiménez-García, R. L. Compton, Y.-J. Lin, W. D. Phillips, J. V. Porto, and I. B. Spielman. Phases of a Two-Dimensional Bose Gas in an Optical Lattice. *Phys. Rev. Lett.*, 105:110401, Sep 2010.

[49] S. Trotzky, L. Pollet, F. Gerbier, U. Schnorrberger, I. Bloch, N. V. Prokof'ev, B. Svistunov, and M. Troyer. Suppression of the critical temperature for superfluidity near the Mott transition. *NATURE PHYSICS*, 6(12):998–1004, Dec 2010.

[50] P. Sengupta, M. Rigol, G. G. Batrouni, P. J. H. Denteneer, and R. T. Scalettar. Phase Coherence, Visibility, and the Superfluid˘Mott-Insulator Transition on One-Dimensional Optical Lattices. *Phys. Rev. Lett.*, 95:220402, Nov 2005.

[51] A. Hoffmann and A. Pelster. Visibility of cold atomic gases in optical lattices for finite temperatures. *Phys. Rev. A*, 79:053623, May 2009.

[52] G. G. Batrouni, H. R. Krishnamurthy, K. W. Mahmud, V. G. Rousseau, and R. T. Scalettar. Canonical trajectories and critical coupling of the Bose-Hubbard Hamiltonian in a harmonic trap. *Phys. Rev. A*, 78:023627, Aug 2008.

[53] L. Pollet, C. Kollath, K. Van Houcke, and M. Troyer. Temperature changes when adiabatically ramping up an optical lattice. *New Journal of Physics*, 10(6):065001, 2008.

[54] K. Sheshadri, H. R. Krishnamurthy, R. Pandit, and T. V. Ramakrishnan. Superfluid and Insulating Phases in an Interacting-Boson Model: Mean-Field Theory and the RPA. *Europhysics Letters*, 22(4):257, 1993.

[55] R. V. Pai, J. M. Kurdestany, K. Sheshadri, and R. Pandit. Bose-Hubbard models in confining potentials: Inhomogeneous mean-field theory. *Phys. Rev. B*, 85:214524, Jun 2012.

[56] W. Krauth, M. Caffarel, and J.-P. Bouchaud. Gutzwiller wave function for a model of strongly interacting bosons. *Phys. Rev. B*, 45:3137–3140, Feb 1992.

[57] D. van Oosten, P. van der Straten, and H. T. C. Stoof. Quantum phases in an optical lattice. *Phys. Rev. A*, 63:053601, Apr 2001.

[58] C. Schroll, Florian Marquardt, and C. Bruder. Perturbative corrections to the Gutzwiller mean-field solution of the Mott-Hubbard model. *Phys. Rev. A*, 70:053609, Nov 2004.

[59] J. Zakrzewski. Mean-field dynamics of the superfluid-insulator phase transition in a gas of ultracold atoms. *Phys. Rev. A*, 71:043601, Apr 2005.

[60] J. Zakrzewski. Erratum: Mean field dynamics of superfluid-insulator phase transition in a gas of ultra cold atoms [Phys. Rev. A 71, 043601 (2005)]. *Phys. Rev. A*, 72:039904, Sep 2005.

[61] A. Dhar, M. Singh, R. V. Pai, and B. P. Das. Mean-field analysis of quantum phase transitions in a periodic optical superlattice. *Phys. Rev. A*, 84:033631, Sep 2011.

[62] P. Pisarski, R. M. Jones, and R. J. Gooding. Application of a multisite mean-field theory to the disordered Bose-Hubbard model. *Phys. Rev. A*, 83:053608, May 2011.

[63] T. McIntosh, P. Pisarski, R. J. Gooding, and E. Zaremba. Multisite mean-field theory for cold bosonic atoms in optical lattices. *Phys. Rev. A*, 86:013623, Jul 2012.

[64] D.-S. Lühmann. Cluster Gutzwiller method for bosonic lattice systems. *Phys. Rev. A*, 87:043619, Apr 2013.

[65] V. A. Kashurnikov, N. V. Prokof'ev, and B. V. Svistunov. Revealing the superfluid Mott-insulator transition in an optical lattice. *Phys. Rev. A*, 66:031601, Sep 2002.

[66] S. Wessel, F. Alet, M. Troyer, and G. G. Batrouni. Quantum Monte Carlo simulations of confined bosonic atoms in optical lattices. *Phys. Rev. A*, 70:053615, Nov 2004.

[67] M. Capello, F. Becca, M. Fabrizio, and S. Sorella. Superfluid to Mott-Insulator Transition in Bose-Hubbard Models. *Phys. Rev. Lett.*, 99:056402, Aug 2007.

[68] M. Capello, F. Becca, M. Fabrizio, and S. Sorella. Mott transition in bosonic systems: Insights from the variational approach. *Phys. Rev. B*, 77:144517, Apr 2008.

[69] J. F. Carrasquilla. *The Bose-Hubbard model with disorder in low-dimensional lattices*. PhD thesis, International School for Advanced Studies (Trieste, Italy), 2010.

[70] C. Kollath, U. Schollwöck, J. von Delft, and W. Zwerger. Spatial correlations of trapped one-dimensional bosons in an optical lattice. *Phys. Rev. A*, 69:031601, Mar 2004.

[71] C. Kollath, A. Iucci, T. Giamarchi, W. Hofstetter, and U. Schollwöck. Spectroscopy of Ultracold Atoms by Periodic Lattice Modulations. *Phys. Rev. Lett.*, 97:050402, Jul 2006.

[72] S. Ramanan, T. Mishra, M. S. Luthra, R. V. Pai, and B. P. Das. Signatures of the superfluid to Mott-insulator transition in cold bosonic atoms in a one-dimensional optical lattice. *Phys. Rev. A*, 79:013625, Jan 2009.

[73] K. Byczuk and D. Vollhardt. Correlated bosons on a lattice: Dynamical mean-field theory for Bose-Einstein condensed and normal phases. *Phys. Rev. B*, 77:235106, Jun 2008.

[74] W.-J. Hu and N.-H. Tong. Dynamical mean-field theory for the Bose-Hubbard model. *Phys. Rev. B*, 80:245110, Dec 2009.

[75] P. Anders, E. Gull, L. Pollet, M. Troyer, and P. Werner. Dynamical mean-field theory for bosons. *New Journal of Physics*, 13(7):075013, 2011.

[76] H. Q. Lin. Exact diagonalization of quantum-spin models. *Phys. Rev. B*, 42:6561–6567, Oct 1990.

[77] J. M. Zhang and R. X. Dong. Exact diagonalization: the Bose–Hubbard model as an example. *European Journal of Physics*, 31(3):591, 2010.

[78] D. S. Rokhsar and B. G. Kotliar. Gutzwiller projection for bosons. *Phys. Rev. B*, 44:10328–10332, Nov 1991.

[79] R. B. Diener, Q. Zhou, H. Zhai, and T.-L. Ho. Criterion for Bosonic Superfluidity in an Optical Lattice. *Phys. Rev. Lett.*, 98:180404, May 2007.

[80] J. K. Freericks and H. Monien. Strong-coupling expansions for the pure and disordered Bose-Hubbard model. *Phys. Rev. B*, 53:2691–2700, Feb 1996.

[81] N. Metropolis, A. W. Rosenbluth, M. N. Rosenbluth, A. H. Teller, and E. Teller. Equation of state calculations by fast computing machines. *JOURNAL OF CHEMICAL PHYSICS*, 21(6):1087–1092, 1953.

[82] S. Sorella. Wave function optimization in the variational Monte Carlo method. *Phys. Rev. B*, 71:241103, Jun 2005.

[83] S. Sorella and F. Becca. SISSA Lecture notes on Numerical methods for strongly correlated electrons. Available online at `http://people.sissa.it/~sorella/Simulazioni.pdf`, 2013.

[84] M. Calandra Buonaura and S. Sorella. Numerical study of the two-dimensional Heisenberg model using a Green function Monte Carlo technique with a fixed number of walkers. *Phys. Rev. B*, 57:11446–11456, May 1998.

[85] S. P. Rath, W. Simeth, M. Endres, and W. Zwerger. Non-local order in Mott insulators, duality and Wilson loops. *Annals of Physics*, 334:256–271, Jul 2013.

[86] J. Wernsdorfer, M. Snoek, and W. Hofstetter. Lattice-ramp-induced dynamics in an interacting Bose-Bose mixture. *Phys. Rev. A*, 81:043620, Apr 2010.

[87] S. S. Natu, K. R. A. Hazzard, and E. J. Mueller. Local Versus Global Equilibration near the Bosonic Mott-Insulator Superfluid Transition. *Phys. Rev. Lett.*, 106:125301, Mar 2011.